REDUCED BORON DIFFUSION UNDER POINT DEFECT INJECTION IN FLUORINE IMPLANTED SILICON

Man Niang Kham

PhD Thesis, September 2007

UNIVERSITY OF SOUTHAMPTON

FACULTY OF ENGINEERING, SCIENCE & MATHEMATICS
SCHOOL OF ELECTRONICS AND COMPUTER SCIENCE

REDUCED BORON DIFFUSION UNDER POINT DEFECT INJECTION IN FLUORINE IMPLANTED SILICON

by
Man Niang Kham

A thesis submitted for the degree of
Doctor of Philosophy

September 2007

UNIVERSITY OF SOUTHAMPTON

ABSTRACT

FACULTY OF ENGINEERING, SCIENCE & MATHEMATICS
SCHOOL OF ELECTRONICS AND COMPUTER SCIENCE

Doctor of Philosophy

REDUCED BORON DIFFUSION UNDER POINT DEFECT INJECTION IN FLUORINE IMPLANTED SILICON

by Man Niang Kham

Fluorine implantation into silicon has recently been recognised as an effective way to reduce boron diffusion, which severely limits the scaling of both metal-oxide-semiconductor transistors and bipolar junction transistors. This thesis reports the results of experiments aimed at understanding the behaviour of fluorine under various device processing conditions and hence aims to identify the mechanisms responsible for the reduced boron diffusion.

Point defect injection studies are performed to study how the injection of interstitials and vacancies from the surface influences the fluorine SIMS peaks and the diffusion of boron marker layers which are placed to coincide with major fluorine peaks of the fluorine profile. SIMS analysis of a sample implanted with 185keV, 2.3 x10^{15} cm^{-2} F^+ and annealed at 1000 °C shows fluorine peaks at depths of $0.3R_p$ and R_p and a shoulder between $0.5\text{-}0.7R_p$. The shallow fluorine peak at a depth of $0.3R_p$ is smaller under interstitial injection than inert anneal and it decreases in size with anneal time. The presence of this shallow peak correlates with the suppression of boron diffusion in a boron marker located at the same depth. These results provide strong evidence that the shallow peak is due to vacancy-fluorine (V-F) clusters and that these clusters are responsible for the suppression of boron diffusion. The elimination of the shallow fluorine peak is explained by the annihilation of vacancies in the clusters by recombination with injected interstitials.

In fluorine implanted samples, less boron diffusion is surprisingly observed under interstitial injection than inert anneal for boron marker layers located in the interstitial-rich region (at R_p) of the fluorine damage profile. TEM images show a band of dislocation loops around the range of the fluorine implant and the density of dislocation loops is lower under interstitial injection than inert anneal. It is proposed that interstitial injection accelerates the Ostwald ripening process- the evolution of interstitial defects into dislocation loops. The accelerated Ostwald ripening process gives a shorter period of time for boron transient enhanced diffusion, thereby resulting in reduced boron diffusion.

A systematic study is made of the effect of device processing on the V-F clusters. SIMS analysis shows that the V-F clusters are stable for anneals of 1.5 hours at 820 °C or 45s at 1050 °C. The clusters are stable in the presence of a low dose dopant co-implant (1x10^{13} cm^{-2}), but are eliminated by a high dose dopant co-implant (2x10^{15} cm^{-2}). Monte carlo simulations show that the damage arising from the dopant co-implant is responsible for the elimination of the V-F clusters. Investigation of the effect of decreasing fluorine implant energy on the V-F clusters shows that a low thermal budget anneal gives a better retention of the V-F clusters and allows a reduction of the fluorine implant energy for application in junction depths down to ~20 nm.

Finally, this thesis reports the implementation of a fluorine implant in a production silicon bipolar technology at STMicroelectronics, Sicily, Italy. A novel approach was used by positioning the fluorine implant deeper than the germanium pre-amorphisation implant. This allows the V-F clusters to suppress the formation of the germanium end-of-range defects through vacancy-interstitial annihilation. It is thus demonstrated that fluorine dramatically suppresses boron diffusion in the base and leads to a world record f_T of 110GHz in an appropriately optimised device.

Contents

List of figures

List of tables

Acknowledgements

First of all, I would like to express my sincere gratitude to my supervisor, Professor Peter Ashburn for his exceptional guidance, patience and advice throughout this project. Every discussion I had with him was challenging and an invaluable experience for me. His optimism and encouragement especially after the clean room fire has helped me to focus and stay on course.

I would like to thank Dr. Janet Bonar for giving me a good start on the Epitaxial equipment and her invaluable suggestions on my work. Many papers and works by Dr. Huda El Mubarek was an inspiration to me. I am grateful to the entire clean room staff of Innos' Ltd for their technical advice and help. My thanks are extended to Dr. A. Smith and Dr. J. Hamilton at the University of Surrey for helping me with the RTA. I like to thank my fellows here in the research group for their friendship and support.

I am indebted to my parents for their love, advice and support. Thankyou to my brothers and sisters for their encouragement and phone calls. My gratitude to my sister, Dr. L. Ciin for encouraging me to get back to study in the UK and supporting me financially during my undergraduate years. Thanks to all my friends from church, and those far and near. Above all, I would like to thank the Lord for always guiding my path in life.

Chapter 1

Introduction

The world's first metal-oxide-semiconductor field-effect transistor (MOSFET) was fabricated on a silicon substrate in 1960 [1]. In the past three decades, the growth of integrated circuit industry has been sustained by the scaling of the physical dimensions of the devices. In MOSFETs, the fabrication of ultra-shallow source-drain extension (SDE) junctions is one of the challenges for device scaling. SDE junction formation requires the fabrication of ultrashallow junctions with a small junction depth (x_j), low sheet resistance (R_s) and high junction abruptness. According to the International Technology Roadmap for Semiconductors (ITRS), a device of 45nm-channel length will require a SDE junction depth of 12nm, sheet resistance of 830 Ω/sq and junction abruptness better than 2.8 nm/decade [2].

The task of achieving ultra-shallow source drain junctions is more challenging for p-channel MOSFETs than n-channel MOSFETs. This is because boron, which is the most favoured dopant for p-channel devices, has a higher diffusivity and a lower solubility in silicon than arsenic, which is used in n-channel devices. Moreover, boron suffers from anomalous diffusion, known as transient enhanced diffusion (TED), where boron diffusion is many times higher than normal thermal diffusion. TED is caused by the damage introduced by ion-implantation, the most common technique used to dope a semiconductor [3,4]. Boron TED hinders the scaling of devices and is the main cause of short channel effects in MOSFETs [5]. It also has detrimental effects in bipolar transistors in degrading the current gain and limiting the value of cut-off frequency [6].

Fluorine has been commonly used in the manufacture of both bipolar and MOS transistors as a BF_2^+ implant for shallow pn junction formation [7]. Over the past few years the interest in fluorine has been increased due to its effect on boron diffusion; research has shown that fluorine implants reduce boron TED [8-13] and also increase boron activation [8]. There were also reports showing that fluorine had little or no effect on boron diffusion [14] and that fluorine enhanced boron diffusion in crystalline [15] and pre-amorphised silicon [16,17]. These contradictory reports have been later reconciled by careful analysis of the experimental

conditions used for the fluorine and boron implants. It has recently been shown that an optimised F implant completely eliminates boron TED and significantly reduces boron thermal diffusion in both crystalline silicon [18] and preamorphised silicon [19]. Several mechanisms have been proposed to explain the effect of fluorine on boron diffusion, including vacancy-fluorine clusters [12,18], boron-fluorine reaction [13,14] and fluorine-Si interstitial interactions [8,10,11,19,20].

Most fluorine experiments reported in the literature are performed in pre-amorphised silicon [12-14, 16-17, 19-23] because a pre-amorphisation implant (PAI) combined with solid-phase epitaxy (SPE) is considered a promising method for the fabrication of ultrashallow junctions for future MOSFETs in both bulk silicon [21] and SOI wafers [31]. However, fluorine experiments performed in conjunction with PAI have also identified many process variables. For example, Jacques et al [17] have shown that F enhances boron motion prior to activation annealing and that the enhancement is higher in Ge^+ pre-amorphised material than in Si^+ pre-amorphised material. The SPE regrowth rate is also dramatically affected by the presence of fluorine [23]. Cowern et al [22] have reported the importance of F implant position with respect to the B implant and the amorphous-crystalline (a/c) interface, while Groui et al [21] have shown that the depth of the a/c interface is less critical than the F dose for obtaining an optimised junction depth and sheet resistance. These variables have resulted in controversy over the F mechanism on B diffusion during SPE regrowth [16,20] and on B diffusion and deactivation during post-SPE annealing [13,19,22]. Impellizzeri et al [19] who performed F implants in silicon pre-amorphised using a silicon implant has shown suppression of boron diffusion in MBE grown boron marker layers. The authors proposed the formation of vacancy-fluorine clusters during the SPE regrowth. Upon post-SPE annealing, the self-interstitials released from end-of-range defects are annihilated by the vacancy-fluorine clusters, thereby reducing the flux of back diffusing interstitials to the surface. Thus, the authors have ruled out the B-F interaction mechanism [19,23]. However, when ultra low energy, high dose boron implants are used (ultrashallow p^+/n junctions), such B-F interactions at the peak of boron profile cannot be discounted [13,22], based on the results of sheet resistance measurements [22]. Finally, review of this PAI+F literature shows that extensive analysis of fluorine SIMS profiles has not been performed largely because fluorine implants into pre-amorphised silicon do not tend to give distinct fluorine SIMS peaks.

For fluorine implants into crystalline silicon, clearly defined fluorine peaks are observed by SIMS analysis [18,24,25]. Moreover, there are less process variables compared to experiments in pre-amorphised silicon, and therefore, interpretation of the F SIMS profiles is easier. For example, El Mubarek et al [18] who used a 185keV, $2.3\times10^{15}cm^{-2}$ F^+ implant into

crystalline silicon, showed that the fluorine profile after anneal exhibited two distinctive peaks: a shallow peak around $R_p/2$ and a deep peak at R_p. This fluorine implant completely eliminated boron TED and also suppressed boron thermal diffusion in crystalline silicon. It was demonstrated that the shallow fluorine peak was responsible for the reduction of boron thermal diffusion in silicon [18,25]. It was proposed that the reduced boron thermal diffusion was due to the formation of vacancy-fluorine clusters which created an undersaturation of the interstitial concentration in the vicinity of the boron marker layer located around $R_p/2$ of the fluorine implant. The authors also showed that the suppression of boron TED correlated with the presence of a band of dislocation loops at approximately the range, R_p, of the fluorine implant [24]. It was proposed that the suppression of boron TED was due to the retention of self interstitials in the dislocation loops, which suppressed their backflow to the surface. In this work, little research was done on V-F cluster behaviour under different processing conditions or their thermal stability for different thermal budget anneals. Moreover, only one F implant energy (185 keV) was used and no information is available on the fluorine behaviour at lower implant energies, where the influence of the surface may be more important.

Recently fluorine implantation has been applied to MOS transistors to reduce boron diffusion in critical areas of the source and drain [26, 27]. Liu et al [26] used a 1×10^{15} cm^{-2} fluorine implant to create a super halo for both 50nm n- and p-channel transistors. The fluorine-assisted halo process resulted in reduced junction capacitance and an improved I_{on} - I_{off} trade-off. Fukutome et al [27] used a 5×10^{14} - 2×10^{15} cm^{-2} fluorine implant prior to the p-channel extension implant to minimise the diffusion of boron in the extension. The fluorine implant led to dramatically improved threshold voltage roll-off characteristics without any degradation of drive current in sub-50nm p-channel MOSFETs. Scanning tunnelling microscopy was used to show that the improvement was due to a reduction of the overlap length, for example from 13 to 7nm in 40-nm gate length p-channel MOSFETs. While fluorine implantation is increasingly being applied to MOS transistors, to date no work has been reported on the application of fluorine to silicon bipolar transistors.

The primary goal of this work is to further investigate the behaviour of the V-F clusters that are proposed to play a vital role in suppressing boron diffusion. Point defect injection studies are performed to gain a better understanding of the physical nature of the V-F clusters and to gain further insights on the mechanism of boron diffusion suppression. We also investigate the behaviour of the dislocation loops and their effect on boron diffusion (Chapters 5 and 6). We also perform a detailed, systematic study of V-F clusters under a wide range of

processing conditions which are of interest for device fabrication. We show how V-F clusters are influenced by the presence of damage from co-implants, and investigate the feasibility of reducing the F implant energy for application in scaled transistors. Finally, we apply fluorine implantation to a production silicon bipolar technology at STMicroelectronics, Sicily, Italy. We demonstrate that the fluorine implant dramatically suppresses boron diffusion in the base and leads to a value of f_T as high as 110GHz in an appropriately optimised device (Chapter 7).

Chapter 2

Literature Review

2.1 Boron TED

Since 1960, the anomalous boron diffusion behaviour has been reported in bipolar devices where abnormally rapid diffusion of base dopant impurity was observed near the emitter region of a doubly diffused n-p-n semiconductor. The effect is known as the emitter push effect which is caused by the enhanced diffusion of base dopant atoms due to interstitials injected by the diffusing phosphorus ions [28]. In boron implanted Si, the anomalous enhanced diffusion during low temperature anneal was reported by Hofker et al in 1973 [29]. It was reported that during the initial stage of the annealing process a fast broadening of the profile occurs, which could not be predicted by the normal diffusion model.

The anomalous diffusion was attributed to either a fast diffusing interstitial component of the boron [29,30] or to damage clusters at the peak of the implantation range [3]. Cho et al [4] implanted a dose of ^{11}B in a silicon layer and stabilized the layer by a 10 s rapid thermal anneal at 1050 °C. The layer was again implanted with a low dose of ^{10}B and then annealed. The results showed that both the newly implanted ^{10}B atoms and the already stabilised ^{11}B atoms experience TED. Thus, it was proved conclusively that boron TED is due to the point defects created by implantation.

TED has a complex dependence on the implantation dose, anneal temperature and time [32-35]. As the name suggests, TED is a transient effect with a decay time that decreases rapidly with increasing anneal temperature. Fig. 2.1 shows experimental results from Michel et al [32] who implanted 60 keV, $2x10^{14}$ cm^{-2} boron in silicon and annealed at temperatures between 800-1000 °C. Fig. 2.1(a) clearly shows that at 800°C, TED is significant for the first 35 min anneal and is negligible for the further 145 min anneal. A similar TED behaviour is observed at a higher anneal temperature of 900 °C, as shown in Fig. 2.1(b) for a shorter time scale. The amount of TED is also significantly reduced at the higher anneal temperature (~150nm at 800°C vs. ~70nm at 900 °C).

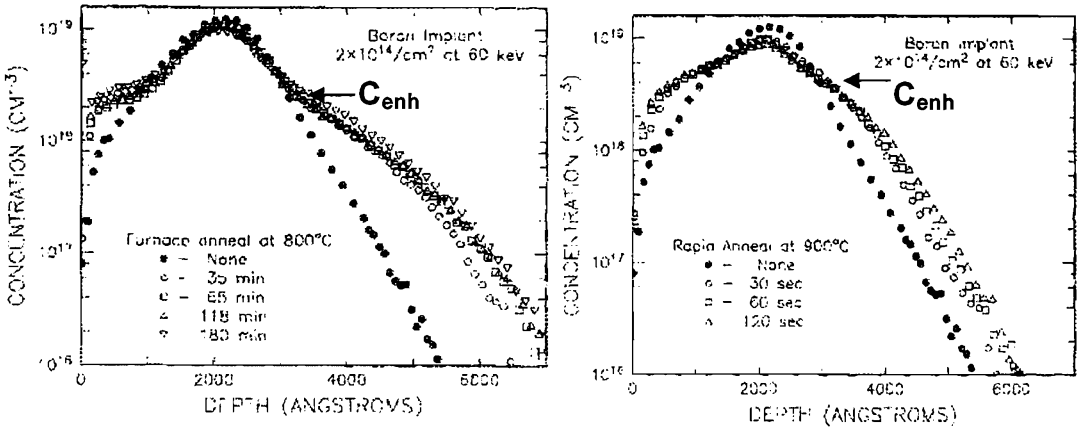

(a) (b)

Fig. 2.1. Boron SIMS profiles for a 60keV, 2x10^{14} cm^{-2} boron implant into silicon after different anneal times at 800 °C (a) and 900 °C (b), after Michel et al [32].

A kink is observed at a concentration from where the enhanced diffusion is seen, as indicated by C_{enh} in Fig.2.1. The value of C_{enh} is related to the intrinsic carrier concentration within a factor of 2 over the temperature range 550-900 °C [33]. Above C_{enh}, a static peak is observed which consists of trapped, non-substitutional B atoms which are electrically inactive. This static peak is nowadays known to be due to boron-interstitial clusters (BICs) which dissolve only at a high temperature [34]. It should be noted that the time scale of BIC dissolution is much longer than that of TED [33].

TED displacement increases linearly with the implant dose. But, a threshold value exists above which, TED saturates (for example, 8x10^{14} cm^{-2} at 900 °C). This TED behaviour was attributed to the formation of different types of defects formed by the higher implant dose [33].

The mechanism of boron TED has been explained by a 'kick-out' reaction [35,36]. A silicon interstitial kicks out a boron atom out of its lattice site to an interstitial position where it can diffuse easily. Alternatively it can form a dopant-interstitial pair which is highly mobile. It is the presence of excess interstitials, the implant damage, which enhances boron diffusion. It has been reported that the enhanced boron diffusivity is proportional to the supersaturation, S, of the excess silicon interstitials [37]. Therefore, during TED, the boron diffusivity can be written in the form

$$D_{B,TED} = D_B^{eq} S = D_B^{eq} . I / I^{eq} \qquad (2.1)$$

where I is the concentration of silicon interstitials, D_B is the diffusion coefficient and the superscript, eq, is the equilibrium value.

2.2 Defects generated by ion implantation

Ion implantation in silicon creates large concentrations of vacancies and interstitials (Si recoils). Each pair of a vacancy and an interstitial is known as a Frenkel pair [38]. Damage annealing is required after implantation to remove the implant damage and electrically activate the dopants by placing them on active substitutional sites. The damage removal can be divided into two distinct regimes: one below and the other above the amorphous threshold.

In non-amorphising implants, usually done by light ions with low implant doses, most of the Frenkel pairs recombine during the initial stages of the annealing. It leaves only extra interstitials whose origin stems from the extra dopant introduced into the lattice. This is commonly known as '+1' model for residual damage due to implants, and the damage level is approximately equal to the implant dose [35]. This primary damage annealing occurs at temperature as low as 400 °C in a time scale as short as milliseconds [39]. Upon further annealing at temperatures above 400 °C, the extra interstitials quickly condense into rod-like {113} defects and sometimes evolve into dislocation loops depending on the implant dose. The defect band is usually formed at the projected range of the ions as shown in Fig. 2.2 (a).

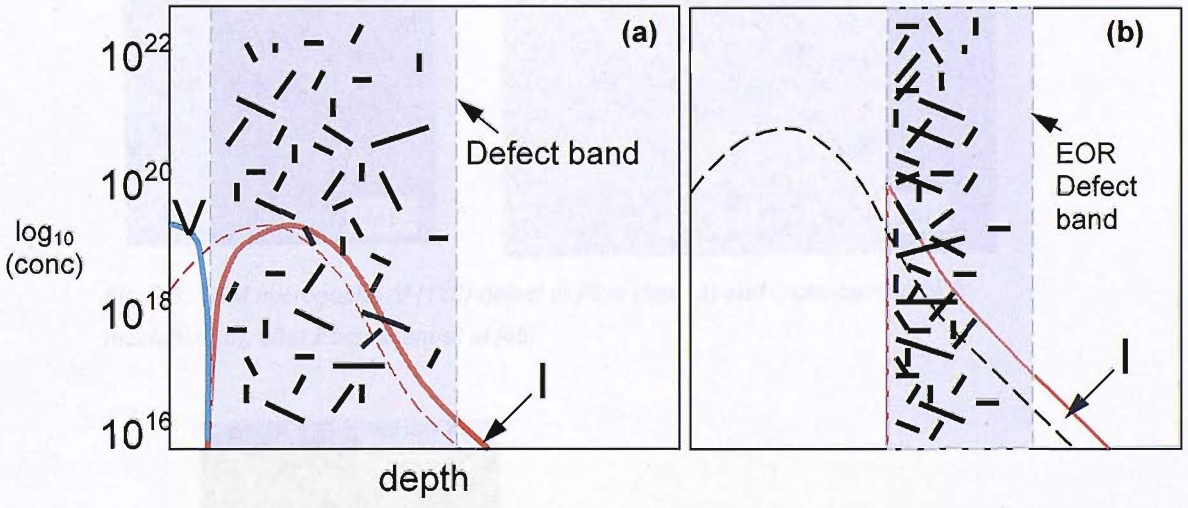

Fig. 2.2. Schematics showing the positions of defect band in the non-amorphising (a) and in the amorphising implants (b) where V and I represents vacancy and Si interstitials, after [40].

Implantations with heavy ions and doses above the amorphisation threshold can transform silicon into an amorphous layer from the surface to a depth beyond the implant range. The amorphous layer can be re-grown into crystalline silicon by a process called solid-phase-epitaxy (SPE) when heated at a temperature as low as 450°C. A large amount of interstitial damage is left below the original amorphous-crystalline (a/c) interface and it is known as end of range (EOR) defects, as shown in Fig. 2.2 (b). Therefore, the EOR defect band formed by

the amorphising implant is narrower and located deeper than the defect band formed by a sub-amorphising implant. This EOR damage consists mainly of dislocation loops and sometimes {113} defects, depending on the anneal conditions.

Fig. 2.3 shows high resolution plan view (a) and cross-section (b) transmission electron microscopy (TEM) images of a {113} defect. It consists of interstitials precipitating on {113} planes running along <110> directions, and is often described as rod-like defects. The smallest {113} defects detected by TEM are about 2nm long, containing at least 40 atoms [44]. {113} defects can grow in size before they either dissolve or grow into dislocation loops, depending on the implant dose and thermal budget. Fig. 2.4 shows a typical plan-view image of dislocation loops formed in 150 keV, $2x10^{15}$ cm^{-2} Ge^{+} amorphised silicon which was annealed at 900 °C [43]. The dislocation loops are precipitates of excess silicon interstitials atoms and they lie on {111} planes. Depending on their crystallographic structure, two types of dislocation loop with different stability are commonly observed: perfect dislocation loop and faulted dislocation loops [43,44].

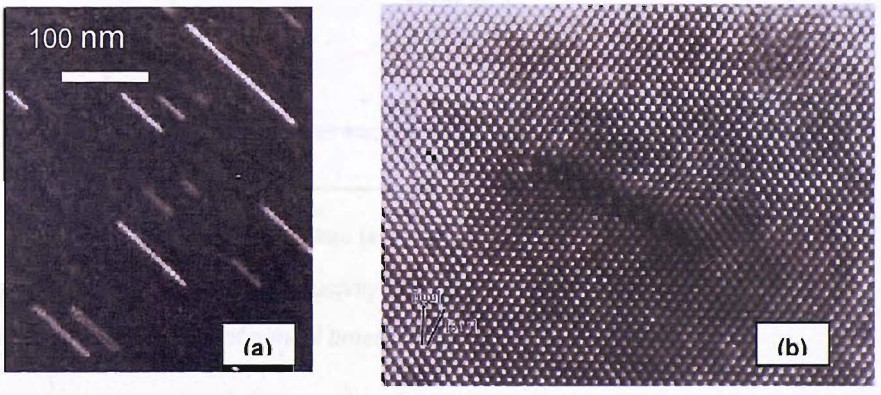

Fig. 2.3. TEM micrographs of {113} defect in Plan view (a) and cross-section high resolution (b), after Eaglesham et al [45].

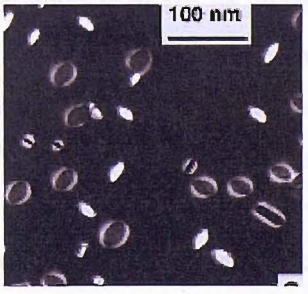

Fig. 2.4. TEM images of EOR dislocation loops in Ge^{+} implanted samples after a 100s anneal at 900 °C, after Cleverie et al [43].

Earlier, Eaglesham et al [45] performed quantitative study of the {113} defects and their thermal behaviour. They demonstrated a link between the number of interstitials emitted by

the {113} defects and the flux of interstitials driving TED and thus concluded that the {113} defects are responsible for boron TED. However, their finding was subsequently proven to be an incomplete picture as Zhang et al [46] showed that strong TED was observed without the formation of {113} defects. Huizing et al [47] studied the time variation of the boron diffusivity enhancement in B marker layers after a 40keV, 2-5x10^{13} cm^{-2} silicon implant and an anneal at 700 °C for times between 15s-40min. As shown in Fig. 2.5, the maximum diffusivity enhancement occurs at a very short time (15s), much earlier than the dissolution of the {113} defects which is in the order of 10^3 s at 700 °C [45]. It has been concluded that a very fast injection of silicon interstitials causes the very high boron diffusivity. The silicon interstitial clusters are very small and difficult to resolve by TEM, but they play a critical role in causing boron TED. These small clusters are known as 'precursors' of the {113} defects [48] and their formation energies and evolution are studied by computer simulation and theoretical calculations [48, 49].

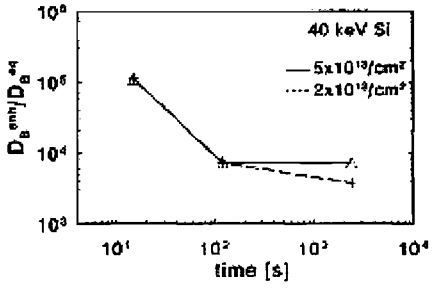

Fig. 2.5. Average enhanced diffusivity of boron spikes in a 40keV Si implanted samples as a function of anneal times, after Huizing et al [47].

The nucleation of the excess interstitials into different types of defects depends on the implant dose and thermal annealing budget. {113} defects and dislocation loops are known as 'extended defects' since they can be imaged by TEM. As shown in the schematic diagram in Fig. 2.6 [41], for implantation doses below 5x10^{12} cm^{-2}, no {113} defects are observed. In this case, only interstitial clusters are formed which are too small to be resolved by TEM. For doses between 5x10^{12} cm^{-2} and 1x10^{14} cm^{-2}, {113} defects are observed and they evaporate at a sufficiently high thermal budget. Above a threshold dose of ~10^{14} cm^{-2}, some of {113} defects undergo unfaulting, forming dislocation loops. At a high thermal budget anneal, only dislocation loops survive since they are more stable defects than {113} defects. Dislocation loops grow in size with the anneal time but they can still be dissolved at a very high anneal temperatures, ~1100 °C [42]. The driving force for transformation of one defect type to another is the reduction of the formation energy [43].

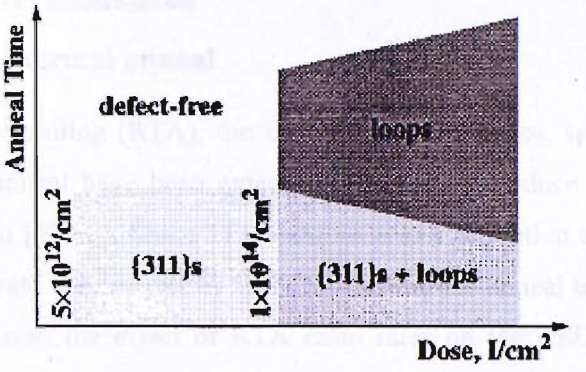

Fig. 2.6. Schematic diagram of the annealing behaviour of defects in relation to the implanted dose and thermal annealing budget, after Stolk et al [41].

The growth of defect size with anneal time mentioned above is explained by the Ostwald ripening mechanism [50]. During annealing, each of these defects is in dynamical equilibrium with a supersaturation of silicon interstitials Si (int), which surround it and is proportional to exp (E_f/kT) where E_f is the defect formation energy. E_f depends on the type and the size of the defects. Hence, a concentration gradient exists between defects and allows the exchange of silicon atoms between defects. Large defects (precipitates) with a small formation energy thus act as sinks for atoms released by small precipitates with a large formation energy. This process maintains a supersaturation of free interstitials in the defect region and can act as a source of interstitials for the rest of the wafer [50]. Ostwald ripening has been accepted by many researchers as the key mechanism in the evolution of the small clusters [48], {113} defects [41] and dislocation loops [42].

Stolk et al [41] performed a quantitative analysis of the thermal evolution of {113} defects at anneal temperature between 670- 815 °C. It was shown that, while there is competitive growth between defects, the total number of interstitials bound to the defects decreases with time and at a rate that increases for increasing temperatures. Thus, the whole defect region can be seen as a source of interstitials which can be released from the defects and diffuse away both towards the bulk and the surface. The whole process can be described as competitive growth within a 'leaky' box and is termed 'non-conservative' Ostwald ripening [43]. The thermal evolution of loops has been studied by Bonafos et al [51] in silicon samples amorphised with a 150keV, $2x10^{15}$ cm^{-2} Ge implant and RTA annealed in the range 900-1100°C. The EOR defect grow in size and reduce their density upon annealing, in a behaviour similar to the {113} defects. However, in contrast to the {113} defects, the total number of silicon atoms stored in the loops remains constant upon annealing. Such a coarsening process can be described as competitive growth within a 'closed' box and is thus called 'conservative' Ostwald Ripening [43].

2.3 TED countermeasures

2.3.1. Advanced thermal anneal

In rapid thermal annealing (RTA), the use of high ramp-rates, spike anneal, flash-assisted anneal and laser anneal have been extensively studied to reduce boron TED and increase electrical activation [52-62]. Since TED exhibits a low activation energy, it is advantageous to electrically activate the dopants by quickly reaching the anneal temperature [54]. Mannino et al [53] investigated the effect of RTA ramp rates on the TED of boron markers in Si implanted samples. The ramp rates were varied between 0.1 and 300 °C/s and the peak anneal temperature between 950 and 1100 °C. TED was reduced when higher ramp rates were used and this effect was credited to the minimization of a strong TED phase which occurs at lower temperatures (600-800 °C). However, high ramp-up rates can degrade uniformity across the wafer and process repeatability [54].

In spike anneal, the dwelling time at the peak temperature is as short as a few milliseconds. It was reported to yield significant improvements in the junction depth and was successfully implemented in the development of the sub-90nm CMOS technology node [55]. For the 65nm and 45nm nodes, flash-assisted annealing [56] and non-melting laser annealing [57,58] are considered as promising methods for achieving the required junction depth and sheet resistance. It should be noted that research on these advanced anneal techniques, for example in refs. 56-58, were performed together with pre-amorphisation. Lerch et al [56] performed optimisation of flash-assisted annealing by using a temperature ramp-up to an intermediate temperature around 700 °C and then an intense flash on the front side of wafer to induce a temperature jump up to 1325 °C with a peak width of 1.6ms. It has been shown to meet sheet resistance requirement for the 65nm technology node without any degradation of the active junction during post-annealing processes.

More recently, laser anneal has been explored as it offers better control over the junction depth and a higher dopant activation than RTA [59-62]. By using an optimised laser energy, together with a Ge^+ preamorphisation and subsequent implants of B^+ and F^+, a p^+-n junction depth of 14 nm with a remarkable super-activation level peaking at $1x10^{21}$ cm^{-3} is achieved [60]. However, challenges faced by the laser annealing technique are the deactivation of dopant during post-annealing and the surface roughness induced by the laser which can deteriorate the device performance significantly [61]. Recently, Sharp et al [62] have shown that multiple scanning (up to 10 scans) of non-melt laser annealing at 1150 °C can significantly reduce the electrical deactivation occurred during post-annealing. The effect has been explained by the removal of end-of-range defects by the multiple scans.

2.3.2. Point defect engineering

Point defect engineering (PDE) is a technique which exploits the spatial distribution of point defects following a high energy ion implantation, in the MeV range, for the formation of ultra-shallow junctions with high dopant activation [63-68]. It has been shown that a Si^+ implant at MeV energy prior to the dopant implant reduces boron TED [63-65]. Other experiments have also shown that boron enhanced diffusion (BED), which is usually associated with a high B concentration layer, is also suppressed by the PDE technique [66]. Recently, Smith [68] showed, by careful optimization, that the Si^+ implant energy could be reduced to 160 keV while still achieving a highly activated ultra-shallow p^+/n junction. It should be noted that the dose of the Si^+ implant are chosen carefully such that the implant does not amorphised the silicon substrate.

2.3.3. Carbon co-implantation

Co-implantation of impurities such as carbon and fluorine has also been researched as countermeasure for TED. Suppression of TED by carbon has been attributed to the formation of carbon-related complexes which trap the silicon interstitials [69]. Carbon is incorporated into silicon by chemical vapour deposition (CVD), molecular-beam-epitaxy (MBE) [69-71] or ion-implantation [72-74]. In order to have an effect on B TED, a threshold concentration of substitutional carbon [72] has to be reached. Once an interstitial has formed a complex with a substitutional carbon atom, the effectiveness of carbon in suppressing TED ceases [70]. For application in devices, SiGeC HBTs have been reported to have improved f_T and f_{max} by a factor of 2 compared to SiGe HBTs [75]. However, it has also been reported that the C-rich region in carbon implanted silicon shows a low electron mobility and the presence of deep donor levels resulting in the degradation of p^+-n diode characteristics [74,76].

2.3.4. Fluorine co-implantation

Wilson [7] performed an extensive study of the depth distributions and carrier profiles of B^+, F^+, BF^+ and BF_2^+ ions in crystalline and amorphous silicon. Comparison of SIMS profiles of a 10keV B^+ and an equivalent 45keV BF_2^+ implant showed that the diffusion of B during annealing was ~25% smaller for the BF_2^+ implant than the B^+ implants. The authors suggested that this effect could either be due to the additional damage caused by the more-massive F atoms or to a chemical effect caused by the F atoms. In later work, F was implanted separately to the boron to characterise the effect of the fluorine on B diffusion. It had been shown repeatedly that fluorine implantation reduces boron diffusion in both crystalline [7-10,18,79] and pre-amorphised silicon [12-14,19-21,80,81]. However, due to the

various experimental conditions used, several mechanisms have been proposed to explain the effect of fluorine on boron diffusion, including vacancy-fluorine clusters [12,18], boron-fluorine reaction [13,14] and fluorine-Si interstitial interactions [8,10,11,19,20,79].

Recently, El Mubarek et al [18] separately studied the effect of F on boron thermal diffusion and boron TED in crystalline silicon by characterizing the diffusion of a buried boron marker layer in wafers with and without a 185 keV, 2.3×10^{15} cm^{-2} F^+ implant and with and without a 288 keV, 6×10^{13} cm^{-2} P^+ implant. Here, P^+ implant was used to introduce implant damage which causes boron TED. As shown in Fig. 2.7 (left figure), the F^+ implanted boron profile (P^+ and F^+ implanted) shows the smallest diffusion indicating that F not only completely suppresses boron TED (P^+ implanted), but also reduces the boron thermal diffusion by 65% (unimplanted). This was the first report to show that fluorine reduces boron thermal diffusion.

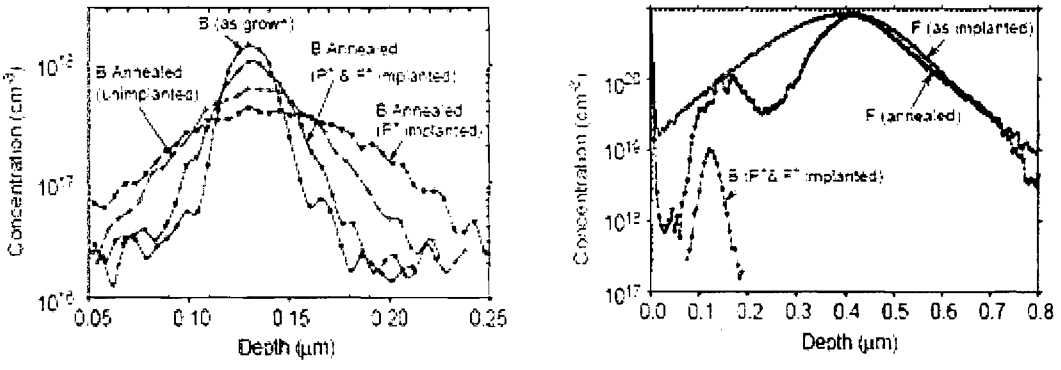

Fig. 2.7. Boron SIMS profiles in P^+ implanted, P^+ and F^+ implanted and unimplanted samples in silicon after an anneal of 30s at 1000 °C in dry nitrogen (left) and overlay of F and B SIMS profiles given the same anneal condition (right), after El Mubarek et al [83].

The fluorine SIMS profile after anneal (Fig. 2.7 right figure) exhibited two distinctive peaks: a shallow peak around $R_p/2$ where R_p is the projected range of the fluorine implant and a deep peak at R_p. A shoulder was also observed between the shallow and deep peak. The reduction of boron thermal diffusion correlated with the presence of the shallow fluorine peak. It was proposed that the $R_p/2$ peak was due to self vacancy-fluorine clusters, and that the clusters suppressed the self interstitial concentration in the vicinity of the boron profile and hence reduced boron thermal diffusion [18]. The authors also showed that a critical fluorine dose exists ($0.9\text{-}1.4 \times 10^{15}$ cm^{-2}), above which boron thermal diffusion is suppressed and below which the fluorine has no effect [25].

The suppression of boron TED correlates with the presence of a band of dislocation loops at approximately the range, R_p, of the fluorine implant [24]. It has been proposed that the

suppression of boron TED is then explained by the retention of self interstitials in the dislocation loops, which suppresses their backflow to the surface. Unlike thermal diffusion suppression, F doses down to 5x 10^{14} cm^{-2} all suppress boron TED [24]. This is presumably the reason why in almost all earlier experiments, boron TED reduction was observed to some degree for both BF_2^+ implants [7,77,78] and low dose F implants [79]. In ref. 79, the presence of F related traps for Si interstitials was proposed for the reduction of boron TED.

In the pre-amorphised (PAI) substrates, the effect of F on boron TED was seen during the post-regrowth annealing [12-14,19-21,80,81]. Impellizzeri et al [19,82] showed that a 100keV, 4x 10^{14} cm^{-2} F^+ implant into pre-amorphised silicon completely suppressed boron TED and also substantially reduced boron thermal diffusion. It was proposed that the presence of fluorine during the solid phase epitaxy (SPE) of silicon leads to a vacancy-rich silicon layer through the formation of vacancy-fluorine clusters. Upon post-SPE annealing, the self-interstitials released from end-of-range defects are annihilated by the vacancy-fluorine clusters, thereby reducing the flux of back diffusing interstitials to the surface [84].

2.4. Point defect injection

Perturbing the equilibrium concentration of interstitial and vacancy point defects in silicon is a method commonly used for determining which point defect mediates the diffusion of common dopants in silicon [38]. In an experiment under oxidation conditions, it was shown that interstitials enhanced phosphorous diffusion and created bigger stacking faults. Hu [85] first linked the growth of stacking faults and the oxidation enhanced diffusion of dopants by proposing they had a common origin. It was known that stacking faults grow in oxidizing ambient and thus he inferred that the enhanced phosphorous diffusion was assisted by interstitials.

A similar point defect injection technique can be used to selectively inject vacancies or interstitials into the silicon substrates during thermal anneal. This can be achieved by annealing silicon in different annealing ambients. On the other hand, point defect injection can also be achieved by annelaing silicon capped with different layers [86]. For example, oxidation of a bare silicon (without cap) results in injection of interstitials, and silicon capped with a nitride layer results in vacancy injection. Oxidation of both oxide and nitride layer capped layers will not inject any point defects and thus gives inert anneal conditions. Interstitial injection occurs due to the growing thermal oxide which injects excess silicon

self-interstitials from the Si/SiO_2 interface into the bulk [85]. Vacancy injection occurs due to compressive strain at the silicon interface caused by the deposited nitride layer. One possible mechanism proposed by Zaitsu et al [88] is that the silicon beneath the nitride layer releases silicon atoms into the nitride film to release the stress caused by the nitride layer, leaving vacancies at the surface of the substrate. Therefore, the vacancy injection effect is dependent on the thickness of the nitride layer [88]. There are a handful of reports in the literature reporting the use of selective point defect injection to study boron and arsenic diffusion in Si and SiGe alloys [86-89].

Chapter 3

Diffusion Theory

Diffusion is a phenomenon where atoms move in the lattice from a high concentration region to a low concentration region. From a macroscopic viewpoint, diffusion process is described by the overall motion of a dopant profile in order to predict the amount of motion, as will be described in Section 3.1. Due to the complex diffusion behaviour of dopants encountered in modern devices, for example boron TED, it has become necessary to understand the diffusion process beyond the macroscopic view point. In the microscopic viewpoint, diffusion is examined by considering the motion of the dopant on an atomic scale, based on interactions between dopant atoms and point defects in the silicon lattice. Point defects are described in Section 3.2 and their effect on dopant diffusion is described in Section 3.3.

3.1. Diffusion from a macroscopic viewpoint

Mathematical formulation of diffusion process was first given by Fick. **Fick's first law** states that diffusion flux of a dopant species J_x, is proportional to its concentration gradient measured normal to the area;

$$J_x = -D\frac{\partial C(x,t)}{\partial x} \quad , \tag{3.1}$$

where $C(x,t)$ is the concentration of diffusing dopant as a function of position and time, and D, the diffusion coefficient or diffusivity of the dopant. The direction of flow is from high to low concentration as indicated by the negative sign in the equation. Applying the law of conservation of matter, the change in concentration with time in the absence of a source or sink, is equal to the rate of change of flux. It can be expressed as,

$$\frac{\partial C(x,t)}{\partial t} = -\frac{\partial J_x}{\partial x} = \frac{\partial}{\partial x}\left(D\frac{\partial C(x,t)}{\partial x}\right). \tag{3.2}$$

When the dopant concentration is less than the intrinsic concentration, the diffusivity is independent of concentration and thus the equation 3.2 can be written as

$$\frac{\partial C(x,t)}{\partial t} = D\frac{\partial^2 C(x,t)}{\partial x^2} \tag{3.3}$$

which is known as **Fick's second law**. Equation 3.3 can be solved analytically subject to various initial and boundary conditions. In the case of a spike or delta function of dopant, the boundary conditions are

$$C \to 0 \text{ as } t \to 0 \text{ for } x > 0$$
$$C \to \infty \text{ as } t \to 0 \text{ for } x = 0 \tag{3.4}$$

and
$$\int_{-\infty}^{\infty} C(x,t)dx = Q \tag{3.5}$$

where Q is the dose of dopant which is contained in the spike. The solution of Fick's second law that satisfies these boundary conditions is

$$C(x,t) = \frac{Q}{2\sqrt{\pi Dt}}\exp\left(-\frac{x^2}{4Dt}\right) = C(0,t)\exp\left(-\frac{x^2}{4Dt}\right) \tag{3.6}$$

Equation 3.6 gives a Gaussian profile with a peak concentration, C(0,t) which decreases as $1/\sqrt{t}$. At a distance $x = 2\sqrt{Dt}$, the concentration $C(x,t)$ has fallen by $1/e$. Therefore, $x = 2\sqrt{Dt}$ gives an approximate measure of how far the dopant has diffused and is usually termed as the 'diffusion length'.

The diffusivity of a dopant, D, can be expressed by the Arrhenius expression

$$D = D_0 \exp\left(-\frac{E_a}{kT}\right), \tag{3.7}$$

where D_0 is the pre-exponential factor in cm^2/s and E_a the activation energy in eV, k the Boltzmann's constant and T the absolute temperature. For impurity diffusion in silicon, E_a is typically 3.5 ~ 4.5 eV. Figure 3.1 shows a plot of intrinsic diffusion coefficient of common dopants in silicon and Table 3.1 shows their corresponding pre-exponential factors and activation energies [39].

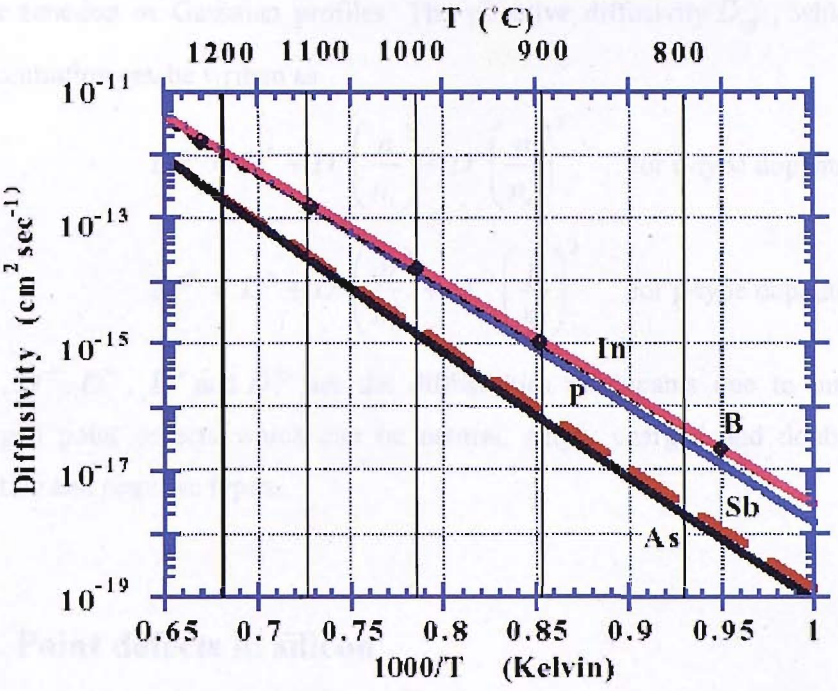

Fig. 3.1. Arrhenius plot of the intrinsic diffusivity of the common dopants in silicon, after ref.[39]

	Si	B	In	As	Sb	P	Units
D_0	560	1.0	1.2	9.17	4.58	4.70	cm^2sec^{-1}
E_A	4.76	3.5	3.5	3.99	3.88	3.68	eV

Table. 3.1. Intrinsic diffusivity for silicon self-diffusion and of common dopants in crystalline silicon, fitted to an Arrhenius expression, after ref. [39].

When the doping concentration exceeds the intrinsic carrier concentration at the diffusion temperature, electric fields set up by the doping atoms can affect the diffusion process. The origin of the electric field comes from the higher mobility of electrons and holes compared to dopant atoms. The additional flux is Cv where v is the velocity of particles due to the electric field and is directly related to the mobility of particles. Assuming v is independent of x, the diffusion equation under extrinsic condition is given by

$$\frac{\partial C(x,t)}{\partial t} = \frac{\partial}{\partial x}\left(D\frac{\partial C(x,t)}{\partial x}\right) - v\frac{\partial C(x,t)}{\partial x} \qquad (3.8)$$

Another effect is also seen at high doping concentration when C is higher than the intrinsic carrier concentration, which is known as concentration-dependent diffusion. Diffusion is faster in the higher concentration regions, resulting in a box-like profile rather than the simple

error function or Gaussian profiles. The effective diffusivity D_{eff}, which varies with the concentration can be written as

$$D^{eff} = D^0 + D^-\left(\frac{n}{n_i}\right) + D^=\left(\frac{n}{n_i}\right)^2 \qquad \text{for n-type dopants} \qquad (3.9)$$

$$D^{eff} = D^0 + D^+\left(\frac{p}{n_i}\right) + D^{++}\left(\frac{p}{n_i}\right)^2 \qquad \text{for p-type dopants} \qquad (3.10)$$

D^0, D^-, $D^=$, D^+ and D^{++} are the diffusivities of dopants due to interactions with the charged point defects which can be neutral, singly charged and doubly charged and of positive and negative types.

3.2. Point defects in silicon

Intrinsic or native point defects exist in the pure silicon lattice when the lattice atoms leave regular lattice sites during continuous vibrations around their equilibrium lattice positions. The absence of an atom from a regular lattice site is called a vacancy (V) and the presence of a self atom out of a regular lattice site is called a self-interstitial (I) as shown in Fig. 3.2 (a). A pair of a vacancy and an interstitial is termed a Frenkel pair and can easily be annihilated due to thermally activated movement.

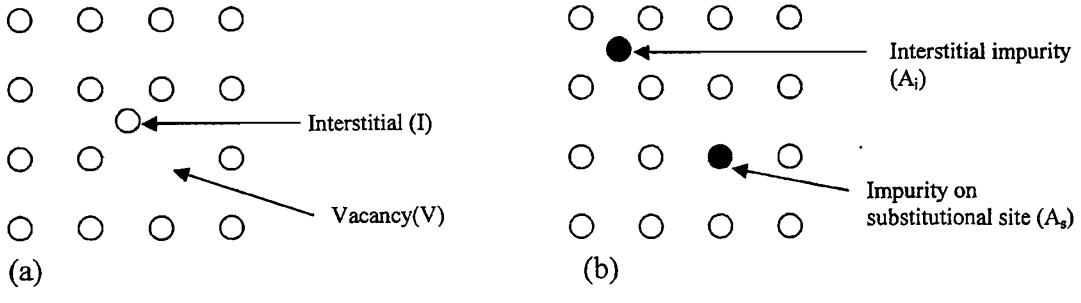

Fig. 3.2. Intrinsic (a) and extrinsic (b) point defects

Extrinsic point defects occur when impurities are introduced into the lattice, usually by ion-implantation, as shown in Fig. 3.2 (b). When an impurity atom, A, occupies a regular lattice site, it is called substitutional impurity (A_s). On the other hand, the impurity atom can occupy an interstitial site (A_i).

For any temperature other than 0 K, a finite concentration of point defects will exist in thermal equilibrium, due to the fact that this situation is the state of the crystal that minimizes its free energy. The equilibrium concentration of a point defect X, where X= I or V, can be expressed as,

$$C_X = \theta_X C_S \exp\left[\frac{G_X^f}{kT}\right] = \theta_X C_S \exp\left[\frac{S_X^f}{kT}\right]\exp\left[\frac{-H_X^f}{kT}\right] \qquad (3.11)$$

where C_S is the number of available lattice sites in the crystal, θ_X is the number of degrees of internal freedom of the defect on a lattice site, G_X^f is the Gibb's free energy, S_X^f and H_X^f are entropy (associated with lattice vibration) and the enthalpy (associated with lattice distortion) of the single point defect formation respectively, k is the Boltzmann's constant and T is the absolute zero temperature. In equilibrium, there is no requirement that the number of vacancy and interstitial defects be equal, because one of the species may recombine at the surface.

It is now well accepted that point defects (interstitials or vacancies) mediate dopant diffusion in silicon [38]. Therefore, much work has been done to study the thermodynamic and transport properties of interstitials and vacancies in silicon. The concentrations of interstitials and vacancies were usually determined by the diffusion of metal species at high temperatures. Bracht et al [90] performed experiments on Zn diffusion in silicon and presented the equilibrium concentration of vacancies and interstitials in the Arrhenius relations shown below,

$$C_V^* \approx 1.4\times10^{23}\exp\left(-\frac{2.0}{kT}\right) \qquad (3.12)$$

$$C_I^* \approx 2.9\times10^{24}\exp\left(-\frac{3.18}{kT}\right). \qquad (3.13)$$

The above equations yield C_V^* and C_I^* to about 2 x10^{15} and 7 x10^{11} cm^{-3} respectively at 1000°C. Figure 3.3 shows an Arrhenius plot of diffusion coefficients D_I and D_V from Bracht's experiment and other values from the literature, taken from Fig. 13 of Ref. [90]. We can deduce from Fig. 3.3 that the diffusion coefficients D_I and D_V are ~10^{-5} and 5 x10^{-9} cm^2/s respectively at 1000 °C.

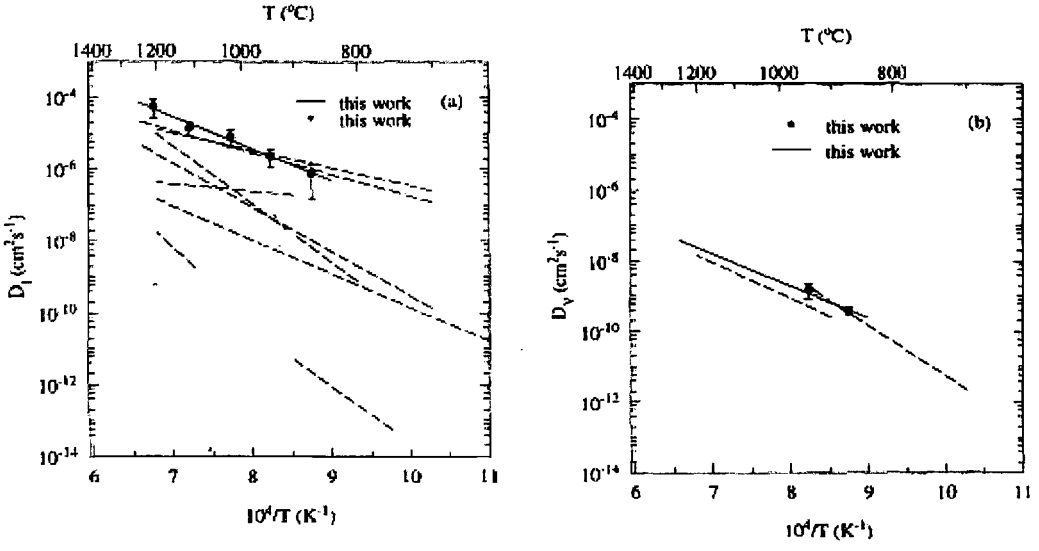

Fig. 3.3. Arrhenius plot of D_I (a) and D_V (b) from Bracht's and other experiments, after Bracht et al [90].

3.3. Diffusion from a microscopic viewpoint

An impurity atom can diffuse in silicon either by a direct or an indirect diffusion mechanism. Figure 3.4 shows direct diffusion mechanisms where point defects are not involved. In Fig. 3.4 (a), small impurity atoms, for example- hydrogen, diffuse via interstitial lattice sites. Therefore, it has a high diffusion coefficient which varies between 10^{-3} and 10^{-6} cm^2/s. Fig. 3.4 (b) shows a direct mechanism of diffusion of substitutional impurity atoms. This method of diffusion requires a large activation energy and thus does not play a significant role in the diffusion of dopants in silicon.

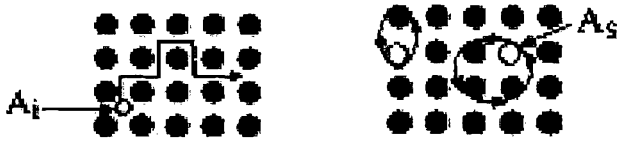

(a) (b)

Fig. 3.4. Schematic 2D representation of direct diffusion mechanisms of an impurity atom, A in a solid. Subscripts i and s indicate interstitial and substitutional positions of the impurity atom, after Bracht et al [91].

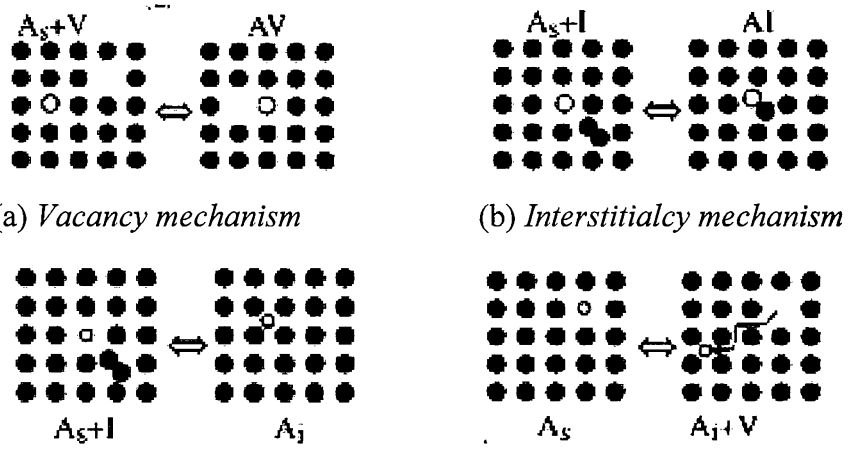

(a) *Vacancy mechanism* (b) *Interstitialcy mechanism*

(c) *Kick-out mechanism* (d) *Dissociative mechanism*

Fig. 3.5. Schematic 2D representation of indirect diffusion mechanisms of an impurity atom, A in a solid. Subscripts i and s indicate interstitial and substitutional positions of the impurity atom. AV is the impurity-vacancy defect pair and AI is the impurity-interstitial defect pair, after Bracht et al [91].

Fig. 3.5 shows indirect diffusion mechanisms which involve interactions between point defects and dopant atoms. V, I, A_i and A_s represent vacancies, silicon self-interstitials, interstitial dopant atoms and substitutional dopant atoms. AV and AI are the impurity-vacancy defect pair and impurity-interstitial defect pair respectively. In silicon, antimony diffuses mainly via vacancies, i.e., vacancy mechanism shown in Fig. 3.5 (a). On the other hand, dopants such as boron, phosphorous, carbon and indium diffuse mainly via interstitials, i.e., the kick-out mechanism as shown in Fig. 3.5 (c) [91].

3.4. Simulation models

There are three diffusion models in ATHENA- the Fermi, two dimensional and fully coupled diffusion models [92]. These models are natural extensions of each other in the sense that the most basic Fermi model is included in the two-dimensional model which is in turn included in the fully coupled model. All three models rely on the concept of pair diffusion, which says that a dopant atom diffuses only by the assistance of a point defect.

3.4.1. Fermi diffusion model

In this model, the point defect populations are assumed to be in thermodynamic equilibrium and thus need no direct representation. The continuity diffusion equation is

$$\frac{\partial C_{ch}}{\partial t} = -\sum_{X=I,V} \nabla J_A \qquad (3.14)$$

where C_{ch} is the chemical dopant concentration, J_A is the flux of mobile dopants, which can

be expressed as,

$$J_A = -D_{AX}\left[\nabla C_A - Z_A C_A \frac{qE}{kT}\right] \tag{3.15}$$

where Z_A is the dopant charge, C_A is the mobile impurity concentration, E is the electric field and D_{AX} is the dopant diffusivity from dopant-vacancy and dopant-interstitial pairs in different charge states.

3.4.2. Two dimensional diffusion model

This model is thus used when point defects are in non-equilibrium conditions, such as when the dopant concentration is very high or annealing is performed under oxidizing conditions. The point defect populations are directly represented and evolved in time. Therefore, the continuity equation for diffusion in equations (3.14) can be modified as

$$\frac{\partial C_{ch}}{\partial t} = \sum_{X=I,V} \nabla J_{AX} \tag{3.16}$$

and

$$J_{AX} = -f_X D_{AX}\left[\nabla C_A\left(\frac{C_X}{C_X^*}\right) - Z_A C_A\left(\frac{C_X}{C_X^*}\right)\frac{qE}{kT}\right] \tag{3.17}$$

where C_X is the point defect concentration and the asterisk refers to the equilibrium condition, f_X is fraction of dopant diffusivity due to either interstitial, f_I or vacancy f_V. There are two other governing equations: one for interstitials and one for vacancies:

$$\frac{\partial C_I}{\partial t} = -\nabla J_I - R_B + R_T - R_{<311>} \tag{3.18}$$

where J_I is the flux of interstitials, R_B is the bulk recombination rate of interstitials, R_T is the capture or emission of interstitials by traps, and $R_{<311>}$ is the recombination rate of {311} clusters.

Similarly, the diffusion equation for vacancies is

$$\frac{\partial C_V}{\partial t} = -\nabla J_V - R_B \tag{3.19}$$

where J_V is the flux of vacancies and R_B is the bulk recombination rate. Figure 3.6 shows an example from ATHENA which demonstrates the difference in the boron profiles between the fermi and two dimensional models when annealing is done under oxidizing ambient. The two dimensional model takes into account the silicon interstitials which are injected into silicon and produces enhanced boron diffusion.

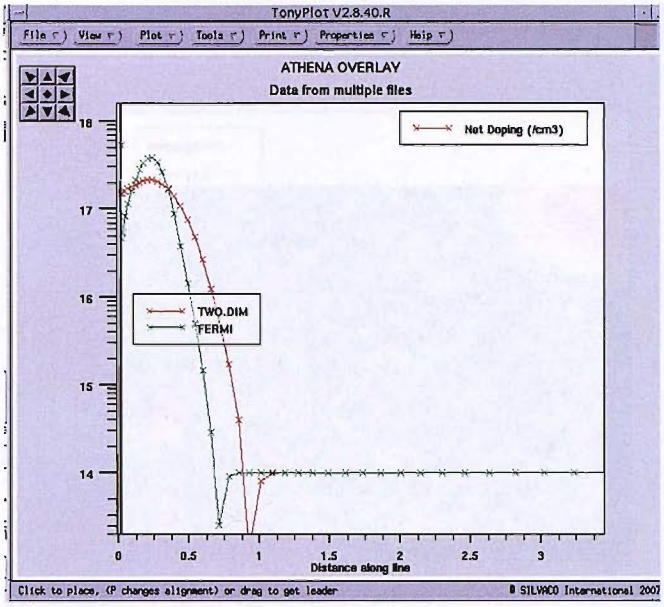

Fig. 3.6. Comparison of boron annealed profiles between Fermi and Two dimensional models in a 70keV, 1x10^{13} cm^{-2} B implants under oxidizing ambient, after [92].

3.4.3. Fully coupled diffusion model

This model is an extension of the two-dimensional model, and the diffusion of the point defects is now influenced by the diffusion of the dopants. There is a true two-way interaction between the diffusion of dopants and the diffusion of point defects. Thus the diffusion equations for the interstitials and vacancies in equations 3.18 and 3.19 are modified as follows:

$$\frac{\partial}{\partial t}\left[C_I + \sum_{A,c} C_{AI^c}\right] = -\nabla\left[J_I + \sum_{A,c} J_{AI^c}\right] - R_B + R_T - R_{<311>} \qquad (3.20)$$

$$\frac{\partial}{\partial t}\left[C_V + \sum_{A,c} C_{AV^c}\right] = -\nabla\left[J_V + \sum_{A,c} J_{AV^c}\right] - R_B \qquad (3.21)$$

where summations run over all dopants and pair charge states.

This model is capable of reproducing certain important aspects of semiconductor processing such as the emitter push effect in the case of phosphorous diffusion, as shown in Figure 3.7. The boron profile beneath the heavily doped emitter region diffuses more rapidly than the boron profile in the base region which is due to the point defects coupling with the diffusing phosphorus.

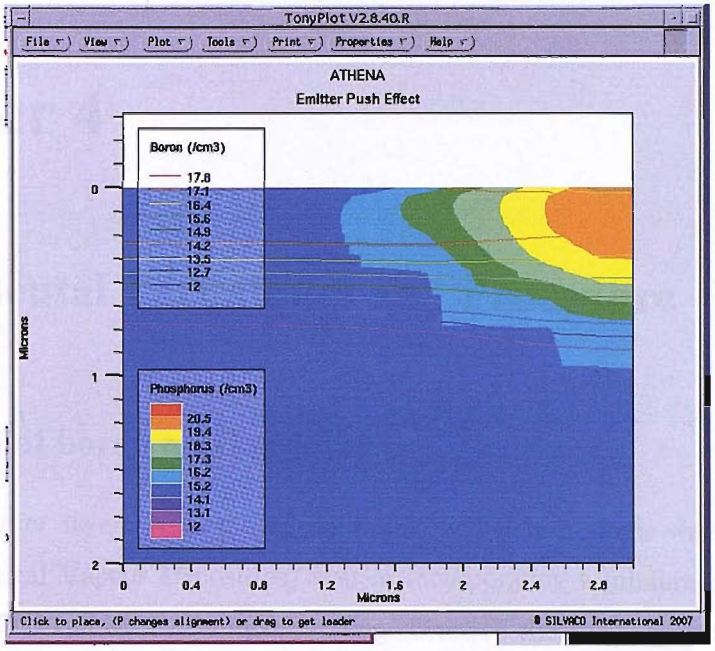

Fig. 3.7. 2-D simulation profile of boron and phosphorus demonstrating the emitter push effect using the fully coupled model. The boron profile beneath the heavily doped emitter region is diffused more rapidly than the boron profile in the base region, due to the point defects coupling with the diffusing phosphorus, after [92].

ATHENA is heavily used for simulation of boron diffusion in the defect injection experiment in chapter 6. In our experiments, the boron doping concentration (~$3x10^{18}$ cm^{-3}) is kept low enough for intrinsic diffusion at the anneal temperature to be used (1000 °C). The aim is not to model the effects of oxidation and fluorine implantation on the boron profiles, but rather to use ATHENA to fit measured boron profiles using simple diffusion theory (Equation 3.3). The Fermi model (FERMI) is therefore used with all the other models switched off (TWO.DIM and FULL.CPL). In this case, the effect of interstitials injected during oxidation is seen as a higher value of boron diffusion coefficients (Chapter 6).

Chapter 4

Experimental Techniques and Procedure

4.1 Growth of boron marker layer

The boron marker layers were grown on Epi-3, which is a single-wafer LPCVD (Low Pressure Chemical Vapour Deposition) system incorporating a mixture of the features of conventional CVD and MBE. By incorporating advanced chemical vapour deposition into a stainless steel chamber, high quality epitaxial layers can be grown similar to those grown by molecular beam epitaxy but without the slow throughput and high cost of MBE [93]. Moreover, reducing growth temperatures and pressures allows the production of materials with sharper dopant transitions, which will better meet the requirements for reduced device sizes. Therefore, in our point defect injection study (Chapters 5 and 6), this system was used to grow silicon and Si-Ge epitaxial layers with sharp boron markers which were accurately placed at particular depths with respect to a fluorine implant. Optimisation of growth conditions such as pressure, temperature and gas flow was based upon the process development performed by Dr. J. Bonar [93].

Before growth, the wafers were *ex-situ* cleaned using an RCA clean followed by a brief dip in a dilute HF solution (HF: H_2O 1:100) to thin the RCA oxide. Once in the process chamber, the wafer was *in-situ* cleaned by a hydrogen bake at 950 °C and 1 Torr pressure for 3 minutes to desorb the oxide remaining on the wafer surface. The wafer was then cooled in hydrogen to the layer growth temperature (either 750 or 800 °C) and the pressure was set to 0.5Torr. Diborane (B_2H_6) was used for doping and silane (SiH_4) and germane (GeH_4) were used as source gases for silicon and SiGe. Before growth on the work wafers, growth characterization was performed including epitaxial quality check and growth rate checks. Table 4.1 summarises the conditions of the growth runs done in the Epi-3 system. The growth interrupt will be discussed in detail in section 4.1.2.

Growth no.	Layer	Temp (°C)	Gas flow(sccm)	Growth interrupt	Note	Figures
5-461	Si	800	SiH_4:H_2 50:250	-	First trial	
5-462	Si	800	SiH_4 50	-	Epi quality+ growth rate check	
5-463	Si	750	SiH_4 50	-	Epi quality+ growth rate check	
5-464	Si	700	SiH_4 50	-	Epi quality+ growth rate check	
5-465	Si:B	750	SiH_4:B_2H_6 50:10	-		Fig. 4.3 (a)
5-473	Si:B	750	SiH_4:B_2H_6 50:10	-	**Batch 1**	Fig. 4.3 (b)
5-544	Si:B	800	SiH_4:B_2H_6 50:15	used	Growth interrupt test	Fig. 4.3 (c)
5-545	SiGe:B	800	SiH_4:B_2H_6:GeH_4 50:15:15	used	SiGe test run	Fig. 4.3 (d)
5-546	Si:B	800	SiH_4:B_2H_6 50:15	used		
5-548	Si:B	800	SiH_4:B_2H_6 50:15	used	**Batch 2**	Fig. 4.3 (e)
5-549	SiGe:B	800	SiH_4:B_2H_6:GeH_4 50:15:15	used		Fig. 4.3 (f)

Table 4.1. A summary of growth details of all the growth runs performed in Epi-3 LPCVD system.

4.1.1. Growth characterization

The quality of the epitaxial layer was observed by Nomarski contrast optical microscopy. Nomarski contrast is obtained by surface interference which highlights imperfections or non-smooth sections of the surface. Fig. 4.1 (a) shows a Nomarski micrograph of a layer grown on a half mask wafer (half of the wafer is covered by an oxide layer) at 800 °C (growth run 5-462). Under the optical microscope, the polysilicon grown on the oxide (L.H.S of Fig. 4.1 (a)) appears as a rough surface, known as the orange peel effect. The crystalline silicon layer grown on the Si-substrate (R.H.S of Fig. 4.1 (a)) is shiny and smooth indicating a high quality epitaxial layer.

To determine the growth rate, the layer thickness was measured by viewing cleaved wafer sections in the scanning electron microscope (SEM). A half-mask wafer was used for the growth rate check. In the SEM, the oxide mask material has a contrast different than the silicon areas. The bottom of the oxide mask will be on the same level as the initial substrate surface, thus the bottom of the oxide will act as a marker from which the epitaxial thickness can be measured. As shown in the cross-section SEM micrograph in Fig. 4.1 (b), by extending a line from the bottom of the oxide mask, the thickness of crystalline silicon is measured.

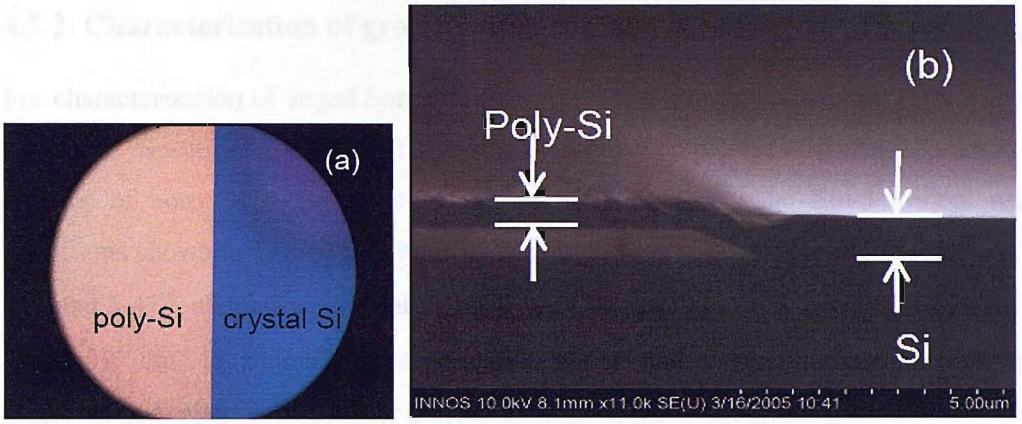

Fig. 4.1. Normarski contrast micrograph (a) and SEM micrograph (b) of a layer from growth chracterisation run, 5-462.

Table 4.2 shows the defect density and growth rate of the characterization layers. The growth defects appear as orange pits in the crystalline silicon under the optical microscope, as shown in Fig. 4.2 taken from ref. [93]. The number of defects was counted in an area seen under x10 magnification of the optical microscope. In layers grown at 800 °C, the defect count is less than 10 counts. The defect count increases when the growth temperature is reduced to 700-750 °C, which means poorer crystal quality. The growth rate is lower at 800°C than at 700 °C. To grow layers of thickness ~1μm for our work, the growth rate is not as critical as the crystal quality. Therefore, a growth temperature of 800 °C was chosen for the work wafers.

Growth no.	Layer	Temp (°C)	Defect density (cm^{-2})	Growth rate (nm/min)
5-461	Si	800	3×10^3	50-55
5-462	Si	800	3×10^3	50-55
5-463	Si	750	2×10^4	65
5-464	Si	700	3×10^4	68

Table 4.2 Summary of defect density and growth rate of the characterisation wafers

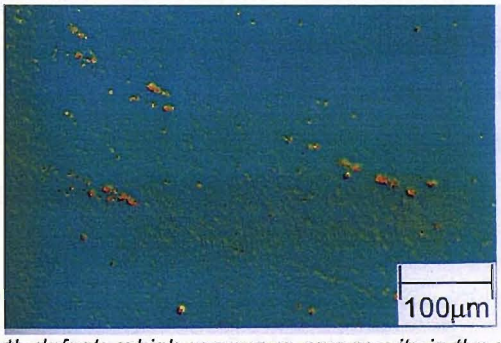

Fig. 4.2. The growth defects which appear as orange pits in the grown crystalline silicon under the optical microscope, after Bonar [93].

4.1.2. Characterisation of grown Boron marker layers

For characterization of doped boron marker layers and silicon-germanium layers, secondary Ion Mass Spectroscopy (SIMS) measurement was employed. Figure 4.3 shows SIMS profiles of boron marker layers in Si and SiGe grown in the Epi-3 system using the conditions shown in Table 4.1. The early growth runs in Figs. 4.3 (a) and (b) (growth nos. 5-465 and 5-473) show that the peak boron concentration fluctuates between 4×10^{18} cm^{-3} in (a) and 7×10^{17} cm^{-3} in (b) and the layer width also fluctuates. A separate investigation by Dr. J. Bonar found poor control over boron doping using a diborane gas flow of 10 sccm. Therefore, the diborane flow was increased to 15 sccm in the later growth runs. Moreover, a tail is observed on the falling edge of the boron profile which is clearly visible in Fig. 4.3 (a). To counter this problem, a growth interrupt was introduced [94] with a 3 minute hydrogen anneal between the growth of the doped layer and the undoped silicon. The interrupt effect can be explained by the purging of any remaining diborane gas from the chamber by the hydrogen. In the case where the growth is continued, the remaining diborane gas would decompose and boron will incorporate into the growing silicon, resulting in the boron tail.

In the next growth runs (growth nos. 5-544 and 5-545) which used a diborane gas flow of 15 sccm and a growth interrupt, the SIMS profiles show an improvement in the marker layers, as shown in Figs. 4.3 (c) and (d). Boron marker layers show similar widths and peak concentrations. However, the boron marker layers are quite thick, measuring ~70 nm at a concentration of 1×10^{18} cm^{-3}. Moreover, the background boron doping level is high (1×10^{17} cm^{-3}) which is suspected to be due to doping from the platen, a likelier source compared to the chamber wall or the heater [93]. Investigations revealed that the platen used in these growths had been used a number of times for high boron doping growths. The practice of flushing the diborane gas during the chamber conditioning run could also worsen the memory effect. Thus, the platen was changed and a conditioning run with silane only was performed for the next growth. Regarding the boron tail, Figs. 4.3 (c) and (d) show that it was improved but not completely eliminated which could be due to the above mentioned memory effect. Fig. 4.3 (d) shows similar, well behaved germanium layers with an atomic concentration of about 10% (i.e., $Si_{0.9}Ge_{0.1}$). The germanium layer thickness is ~70 nm, which is measured at a concentration of $1x10^{20}$ cm^{-3} (at 0.2% Ge).

All the countermeasures were included in the final growth set, and the SIMS profiles are shown in Figs. 4.3 (e) and (f) (growth nos. 5-548 and 5-549). Boron marker layers with peak concentrations of ~3×10^{18} cm^{-3} and widths of ~30nm at a concentration of 1×10^{17} cm^{-3} were achieved. Neither boron tails nor autodoping effect is observed. Further adjusting of the gas

flow time achieved more precise placing of the boron marker layers with respect to the fluorine profile, as shown in Fig. 4.4. This growth was used for the defect injection experiment as reported in Chapters 5 and 6. The position of boron peak 1 was chosen to coincide with the shallow peak, peak 2 with the shoulder and peaks 3 and 4 with the deep peak of the 185 keV F^+ annealed profile.

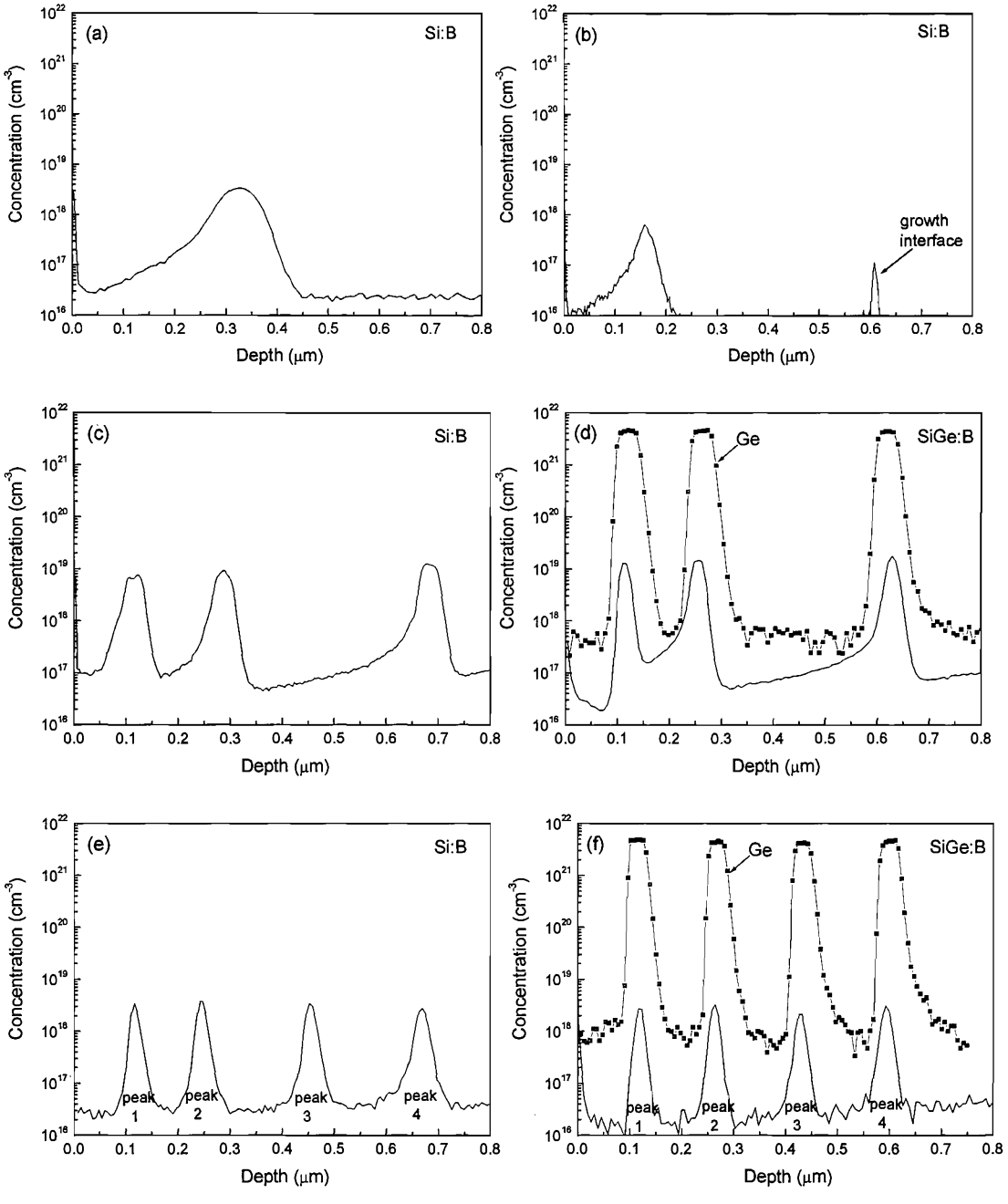

Fig. 4.3. SIMS profiles of boron marker layers in Si and SiGe for growth numbers 5-465 (a), 5-473 (b), 5-544 (c), 5-545 (d), 5-548 (e) and 5-549 (f). For growth details see table 4.1.

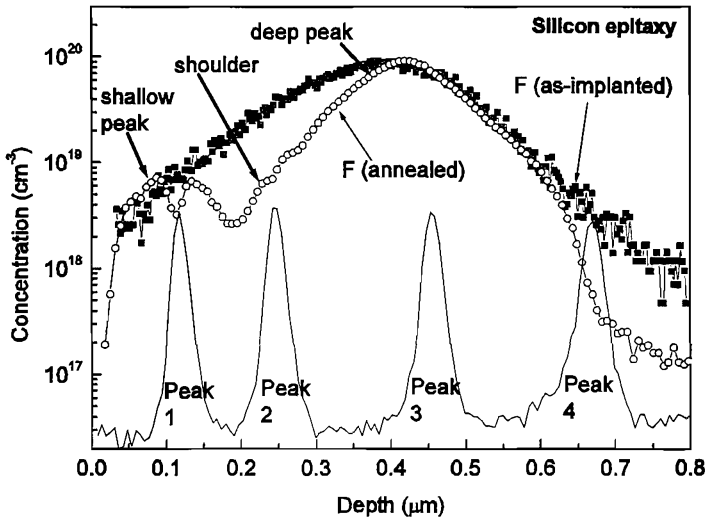

Fig. 4.4. SIMS profiles of boron marker layers after growth showing the location of the four boron peaks with respect to the fluorine profiles after implant and anneal.

4.2 Ion implantation

Ion implantation is a well developed impurity doping technique for silicon integrated circuits. It introduces energetic, charged particles into the target material, such as silicon, to change its electrical properties. The process consists of extracting impurity ions from a source, purification and accelerating them with a high velocity towards the target. Compared to conventional doping methods like diffusion, ion implantation offers more precise control over the dopant profile, better reproducibility and lower processing temperatures. The main disadvantage of ion implantation is the damage it creates in silicon. It thus requires a thermal treatment to repair the damaged lattice and electrically activate the impurities during which the implantation damage can result in anomalous diffusion such as transient enhanced diffusion. Implantation energies range from a few hundred eV to a few MeV, resulting in the average depths ranging from a few nm to 10 μm. Ion doses vary from 10^{12} to 10^{18} cm^{-2}.

The total distance that an ion travels before coming to rest is called the range (R) and the projection of this distance along the axis of incidence is called the projected range (R_p). The statistical fluctuations in the projected range are called the projected straggle, σ_p. The implanted impurity profile can be approximated by a Gaussian distribution:

$$C(x) = \frac{\Phi}{\sqrt{2\pi}\sigma_p} \exp\left[-\frac{(x-R_p)^2}{2\sigma_p^2}\right], \qquad (4.1)$$

where $C(x)$ is the impurity concentration at a depth x and Φ is the total dose implanted, which can be calculated by measuring the ion beam current and integrating it over the time of implantation.

On entering a target material, an energetic ion loses its energy through a series of collisions with the target atoms. During collision, the energetic ion transfers its energy to the target nuclei and it may dislodge the target nuclei from their original lattice sites. This is known as nuclear stopping which is significant for higher mass ions at low energies. On the other hand, the incident ion may interact with the cloud of electrons surrounding the target atoms, resulting in the excitation of the electrons. This is called electronic stopping which is significant at high implant energies.

Figure 4.5 shows a schematic of lattice disorder in the region around the ion track. At low doses, the highly disordered regions around the tracks of the ions are spatially separated form each other (top left figure). At high doses, the individual disordered regions begin to overlap and at some point an amorphous layer is formed (top right figure) [95].

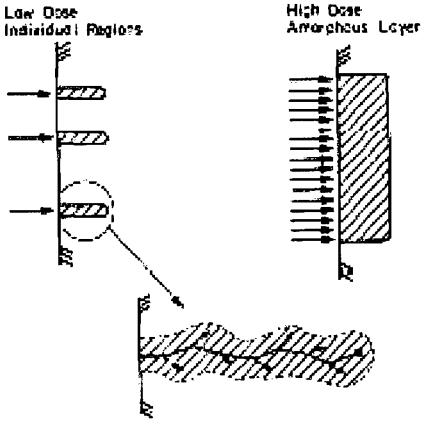

Fig. 4.5. Schematic representation of the disorder produced in samples implanted with low dose (top left) and high dose (top right), after Mayer et al [95].

4.2.1. A case of B cross contamination

Ion implantation in our work was performed in Innos Ltd's medium current Varian implanter. During the high energy fluorine implant (185keV) for batches 1 and 2, a boron cross contamination effect was observed. For the fluorine implanted sample shown in Fig. 4.6, the boron profile not only shows the boron marker layer, but also a boron implant with a range of 0.18 μm and a dose of 1.45×10^{13} cm^{-2}. Investigation into this problem together with D. Chivers, Ion Beam Services (UK) Ltd is briefly described here.

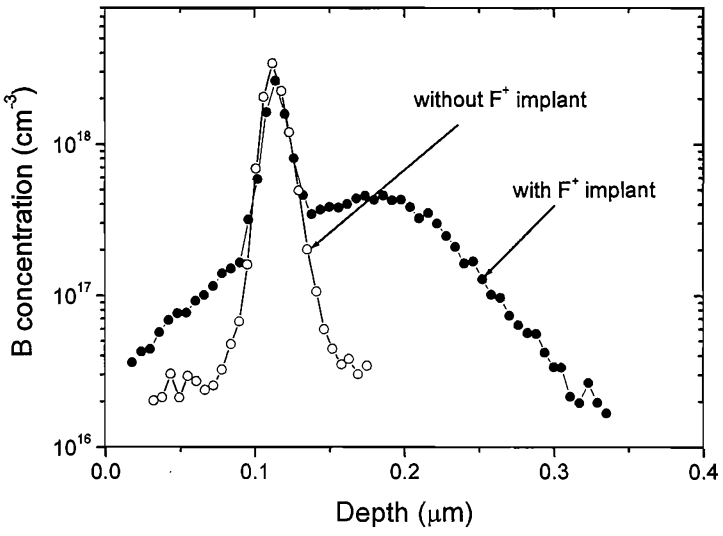

Fig. 4.6. SIMS profiles of overlayed boron marker layers with and without 185 keV, 2.3×10^{15} cm^{-2} F$^+$ implant.

The cross contamination occurs due to a charge exchange collision between BF_2^+ ions and residual gas molecules in the vacuum creating BF^+ ions. The analysing magnet of an implanter usually separates the "apparent mass" instead of the exact mass of the ions. The so called "apparent mass" is due to the changes in charge or molecular states during the charge exchange collision. It can be calculated by the following equation [96]:

$$M_{app} = \frac{q_{ex}}{q_{an}^2} \frac{m_{an}^2}{m_{ex}} \tag{4.2}$$

where M_{app} is the apparent mass, q is the charge state, m is the mass and the subscripts *ex* and *an* are the extracted and analysed ion. The apparent mass of BF^+ is thus calculated to be 18.37, which the analysing magnet is unable to resolve from the F^+ mass of 19.

For the 185 keV F^+ implant, the extraction and post acceleration voltages used are 70 and 115 keV respectively. Along with F^+ ions, unwanted BF^+ ions are also accelerated with 43 and 115 keV in the two stages and result in a total energy of 158 keV. Finally, the energy of the unwanted B^+ ions from this BF^+ implant is calculated to be 58 keV, producing an implant with a range of 0.18 μm as shown in Fig. 4.6. Correction of the boron SIMS data to account for this problem is described in section 4.5. It should be noted that this problem occurs only for the implants in Batches 1 and 2. For Batches 3 to 5, this problem was countered by fluorine implantations using zirconium tetrafluoride, ZrF_4 source. The implantation for Batches 3 to 5 was performed in Philips Microsystems Plaza R&D cleanroom in Eindhoven.

4.3. Rapid Thermal Anneal

Two rapid thermal annealers were used in our work: an AG Associates' RTA Heatpulse-610 and the Surrey Ion Beam Centre's Process Product Corporation (PPC) annealer. The Heatpulse-610 system uses an enclosed quartz chamber which is heated by tungsten halogen lamps situated above and beneath the quartz wafer holder. In the process chamber the wafer is placed on the quartz tray. The wafer temperature is measured by an optical pyrometer which measures emissivity of the wafer susceptor. A polysilicon susceptor is used to get round problems of different emissivities produced by the different coating layers on the wafer back surfaces. The emissivity was determined during temperature calibration by using a test wafer with a series of thermocouples embedded in it and the temperature was measured on the thermocouple as the RTA is heated up. In this system, the ramp up rate is ~25 °C/sec and the steady state temperature stability is ± 7 °C. Before RTA was performed, the system was usually purged with nitrogen for at least 3 minutes. This is important especially if oxygen anneal was used in the preceeding batch. To ensure the accuracy of the process temperature, three dummy runs were performed before annealing of the work wafer. The work wafer was usually placed on the polysilicon susceptor which has a recess the size of a 4 inch wafer. When 1cm x 1cm samples were used in our experiments, dummy pieces were used along with the work samples to complete a four-inch wafer area on the susceptor, as shown in Fig. 4.7(a). This ensures that there were no free edges where heat loss could occur.

The information on the Surrey Ion Beam Centre's PPC annealer and its calibration details can be found in Dr. A. Smith's Ph.D. dissertation [68]. In this system, the work samples were placed in a selected area of a four-inch support wafer, as shown in the sketch in Fig.4.7 (b). The selected area was chosen as it gives the most accurate temperature uniformity [68].

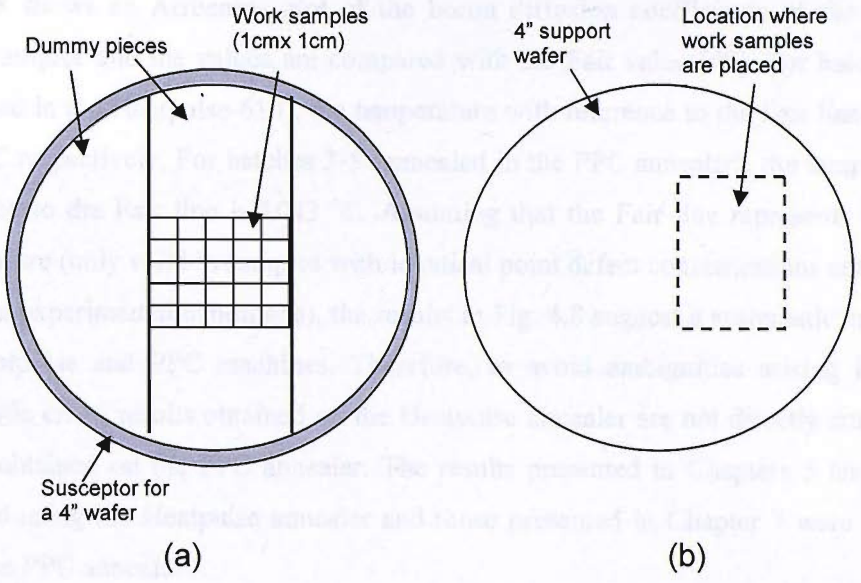

Fig. 4.7. Sketches showing the annealing procedure of work samples in the Heat pulse-610 annealer (a) and in the PPC annealer (b).

4.3.1. Absolute anneal temperature

In rapid thermal annealing, the wafer is heated to high temperatures on a short timescale (in seconds). Unlike in furnaces, the high temperature ramp-rates used in RTA prevent the wafer from coming to thermal equilibrium with the process chamber. Therefore, one of the key challenges in rapid thermal annealing is accurate measurement and control of the wafer temperature. In modern RTA equipment, the wafer temperature is measured *in situ* by an optical pyrometer as described briefly in the previous section.

Here, the accuracy of the absolute temperature of the rapid thermal annealers used in this work is illustrated from the boron diffusion coefficients of wafers annealed in the two different machines. Table 4.3 shows details of the RTA check wafers which were annealed under inert conditions.

Batch	Wafer samples	Anneal conditions	Ambient	Equipment
1	Si with B markers (oxide+nitride capped)	1000 °C, 30s	O_2 (inert)	Heatpulse-610
2	Si with B markers (oxide+nitride capped)	1000 °C, 45s	O_2 (inert)	Heatpulse-610
3,4,5	Si with low dose B implant + Damage annealed @ 900 °C, 120s	1050 °C, 45s	N_2	PPC

Table. 4.3. Details of temperature accuracy check wafers for rapid thermal annealers and the anneal conditions used.

Fig. 4.8 shows an Arrhenius plot of the boron diffusion coefficients of the temperature check samples and the values are compared with the Fair value [99]. For batches 1 and 2 (annealed in the Heatpulse-610), the temperature with reference to the Fair line is 1025 and 1034 °C respectively. For batches 3-5 (annealed in the PPC annealer), the temperature with reference to the Fair line is 1043 °C. Assuming that the Fair line represents the absolute temperature (only valid in samples with identical point defect concentrations annealed under identical experimental conditions), the results in Fig. 4.8 suggest a systematic error between the Heatpulse and PPC machines. Therefore, to avoid ambiguities arising from such a systematic error, results obtained on the Heatpulse annealer are not directly compared with results obtained on the PPC annealer. The results presented in Chapters 5 and 6 were all obtained using the Heatpulse annealer and those presented in Chapter 7 were all obtained using the PPC annealer.

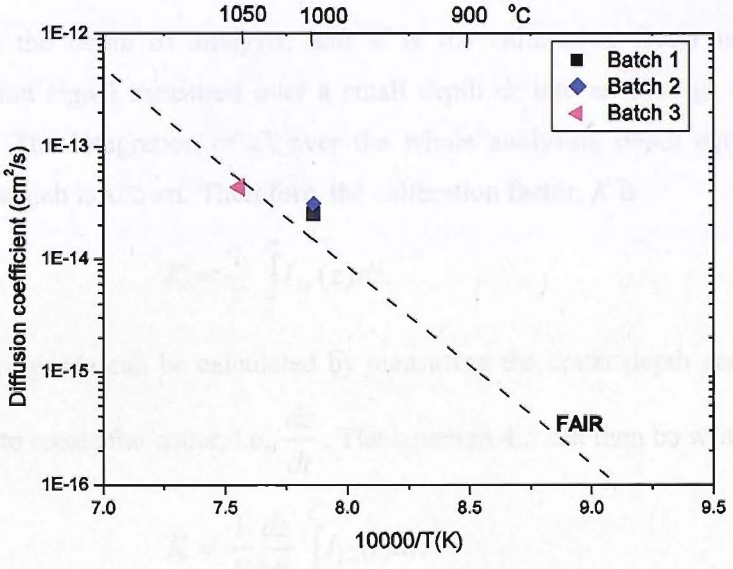

Fig. 4.8. Boron diffusion coefficients of RTA temperature check samples from batches 1 and 2 annealed in the Heatpulse-610 annealer and batch 3 annealed in the PPC annealer. The dashed line has been constructed from the data published by Fair [99]

4.4. Secondary Ion Mass Spectroscopy (SIMS)

Secondary Ion Mass Spectroscopy (SIMS) is an analytical technique used to characterise semiconductor materials. The basis of SIMS is sputtering away sample material and analysing the sputtered ions. Only a small fraction of the sputtered atoms is ionised and these ions are collected and analysed for their mass using a mass spectrometer.

The secondary ion current of a positive ion of element i, I_{i+} is given by [7]:

$$I_{i+} = I_p S \gamma_{i+} N_i \eta \tag{4.3}$$

where I_p is the primary ion beam current, S is the sputtering yield, γ_{i+} is the ionisation efficiency, N_i is the atomic fraction of i, and η is an instrumental factor. Since some of these parameters in equation (4.3) are generally poorly known, the usual approach is the use of reference sample or standard with composition and matrices similar to the unknown sample. Ion implanted samples with known doses are most commonly used as standards. The secondary ion signal integrated over the entire profile measured for the standard is related to the atomic concentration in the standard as

$$\int_0^z I_{i+}(z)dz = K \int_0^z C_i(z)dz, \tag{4.4}$$

where z is the depth of analysis, and K is the calibration factor used for converting secondary ion signal measured over a small depth dz into an average concentration C_i in atoms/cm^3. The integration of C_i over the whole analysing depth equals the fluence, F, atoms/cm^2 which is known. Therefore, the calibration factor, K is

$$K = \frac{1}{F} \int_0^z I_{i+}(z)dz. \tag{4.5}$$

The sputtering rate can be calculated by measuring the crater depth and dividing it by the time taken to create the crater, i.e., $\frac{dz}{dt}$. The equation 4.5 can then be written as

$$K = \frac{1}{F} \frac{dz}{dt} \int_0^t I_{i+}(t)dt. \tag{4.6}$$

And the calibration factor K can now be used to convert the measured secondary ion signal into absolute concentration.

$$C_i = \frac{1}{K} I_{i+}. \tag{4.7}$$

Calibrated standards are therefore very important for accurate SIMS measurements. The above relation also enables to calculate the SIMS profile (plot of concentration of element (in atoms/cm^3) vs. depth) from the ion count vs. time plot.

As shown in equation 4.3, the sputtering and secondary ion yield depends on the primary ion beam, I_p, and more specifically on the species, energy and incident angle. The most commonly used primary ion beam species for depth profiling analysis for semiconductor

materials are O_2^+ and Cs^+. For electropositive elements like B and Al in silicon, an electronegative O_2^+ beam enhances the secondary ion yield, while an electropositive (Cs^+) beam gives a better yield for electronegative elements like P, As and Sb in silicon. The typical primary ion beam energy used for analysis is 0.5 to 10keV. The sputtering yield increases with the beam energy but the depth resolution suffers. A high angle of incidence is also required to increase the sputtering yield.

In our work, SIMS analyses were performed at Loughborough Surface Analysis Ltd. For fluorine analysis, the sensitivity level of fluorine obtained by O_2^+ primary ion beam was comparable to that obtained by Cs^+ primary ion beam. Therefore, an O_2^+ primary ion beam was used to allow the relative positions of boron and fluorine to be monitored by profiling them simultaneously. The O_2^+ beam at 10keV with 0.8 μA current was rastered over a 250 μm square area. Analysis was done only on the secondary ions collected from a 60 μm square area at the crater bottom. The crater depth was measured by interference microscopy, which is accurate to ± 10nm. The Rp of the annealed fluorine SIMS profile peaks were aligned to the Rp of the as-implanted fluorine SIMS profile peak to reduce error in depth scaling arising from the SIMS analysis. Fig. 4.9 shows F SIMS profiles for samples annealed for 30s at 1000 °C with the SIMS analysis performed on different days. Although the anneal ambient was different: nitrogen and inert (oxygen anneal for silicon with capped layers), it has little effect on the fluorine SIMS profile. The very similar fluorine profiles in Fig. 4.9 indicate the repeatability and reliability of the SIMS analysis.

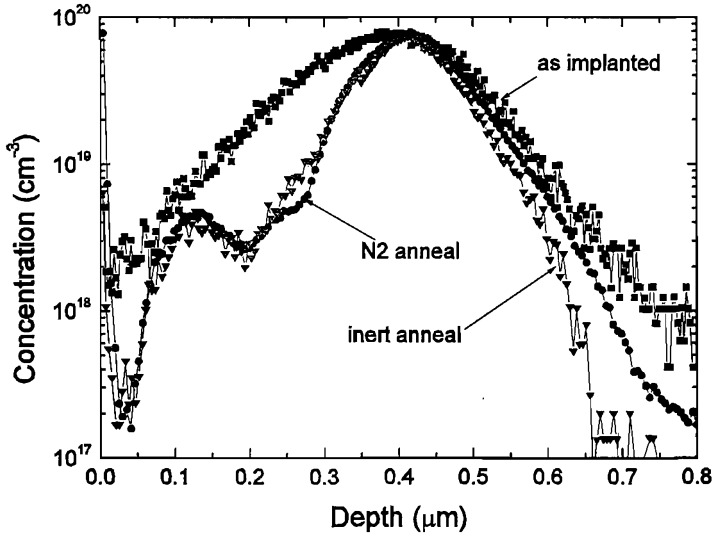

Fig. 4.9. Overlay of SIMS profiles of a 30s anneal at 1000 °C annealed samples with the SIM analysis performed at different days.

4.5. Extraction of boron diffusion coefficient in ATHENA

The annealed boron SIMS profile peaks were aligned to the as-grown boron SIMS profile peak by adding or subtracting an offset to the depth obtained from the SIMS. The boron doses in all profiles were normalised to the as-grown boron dose as loss of boron from the sample is not expected for a buried B marker layer. This procedure reduces errors in dose and depth scaling arising from the SIMS analysis. The annealed boron profiles were fitted using the optimizer program in ATHENA (SSUPREM4) [92]. This was done by importing the as-grown and the annealed boron SIMS profiles into a silicon layer defined in the ATHENA input file. The intrinsic boron diffusion coefficient parameter (Dix.0) was then optimised with all the other factors turned off, using Fermi diffusion model, until a good fit was obtained between the fitted and the measured boron SIMS profile. The input file is shown in Appendix 1. Typical fits to the measured profiles for boron peak 1 of the unimplanted sample can be found in Fig. 6.5(a) of Chapter 6. For the unimplanted samples, the fitting error is within 5% for peaks 3 and 4 and 5-10% for peaks 1 and 2.

As is shown in Chapter 7, a low dose boron implant has no effect on the fluorine profiles and hence does not affect the V-F clusters or the dislocation loops generated by the fluorine implant. The 1.45×10^{13} cm^{-2} contamination implant should therefore have no effect on the diffusion of the boron marker layers. However, to extract boron diffusion coefficients for boron marker layers in the vicinity of the contamination implant (peaks 1 and 2) it is necessary to correct the B SIMS profile to remove the contamination implant data. For boron peaks 3 and 4, this correction procedure is not necessary. Figure 4.10 shows how the unwanted boron profile (curve B: contamination after anneal) was subtracted from the measured boron SIMS profile (curve A: SIMS after anneal), taking into account the effect of the diffusion of the unwanted boron profile during the anneal. The diffusion of the contamination implant during anneal was simulated using the TED 'plus one' implantation damage model with a damage factor of 0.01 (D_{TED}= 7 $\times 10^{-13}$ cm^{-2}) [92]. It should be noted that for longer anneal times, the intrinsic diffusion coefficient value (D_{TD}= 1.53 $\times 10^{-14}$ cm^{-2}) [99] was used assuming that TED would have ceased by then. The corrected boron profile was then obtained by subtracted the contamination profile from the measured SIMS profile (curve A-B). This corrected profile was used to extract the boron diffusion coefficient.

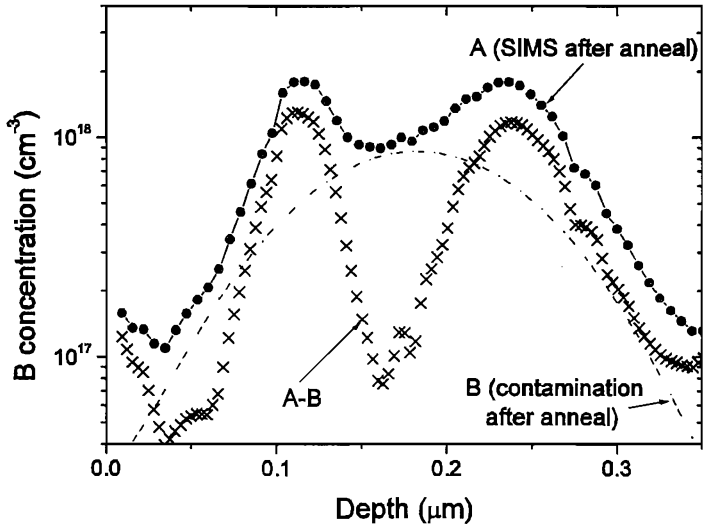

Fig. 4.10. Overlay of the boron SIMS profile after a 15s inert anneal at 1000°C (A), the contamination profile after anneal (B) and the subtracted boron profile (A-B).

To validate the data correction, we show in Fig. 4.11 a comparison between the reconstructed data (addition of contamination after anneal (B) and fit to the profile (A-B)) and the measured SIMS after anneal (A) at 1000 °C under inert conditions. For peak 1 in Fig. 4.11(a), good agreement is obtained between the reconstructed profile (B+D) and the measured SIMS profile (A), for concentrations above ~2 x10^{17} cm^{-3}. Reasonable agreement is also obtained for peak 2 for concentrations above 7x10^{17} cm^{-3}. For a longer time of 120s, Fig. 4.11(b) shows that similar agreement is obtained for peak 1 as for the short anneal time. But for peak 2, a good fit could only be obtained at concentrations above 1x10^{18} cm^{-3}. Table 4.4 summarises the fitting errors for all four boron peaks in the fluorine implanted samples after inert anneal at 1000 °C for 15 to 120s. The larger error for peaks 1 and 2 is due to the boron contamination problem. Similar fitting errors were obtained for the fluorine implanted sample annealed under interstitial injection conditions.

Anneal time (s)	Peak 1	Peak 2	Peak 3	Peak 4
15	5%	10%	≤ 5%	≤ 5%
45	10%	20%		
120	20%	30%		

Table 4.4. Summary of fitting errors for all the boron peaks in the fluorine implanted samples after inert anneal at 1000 °C for 15 to 120s.

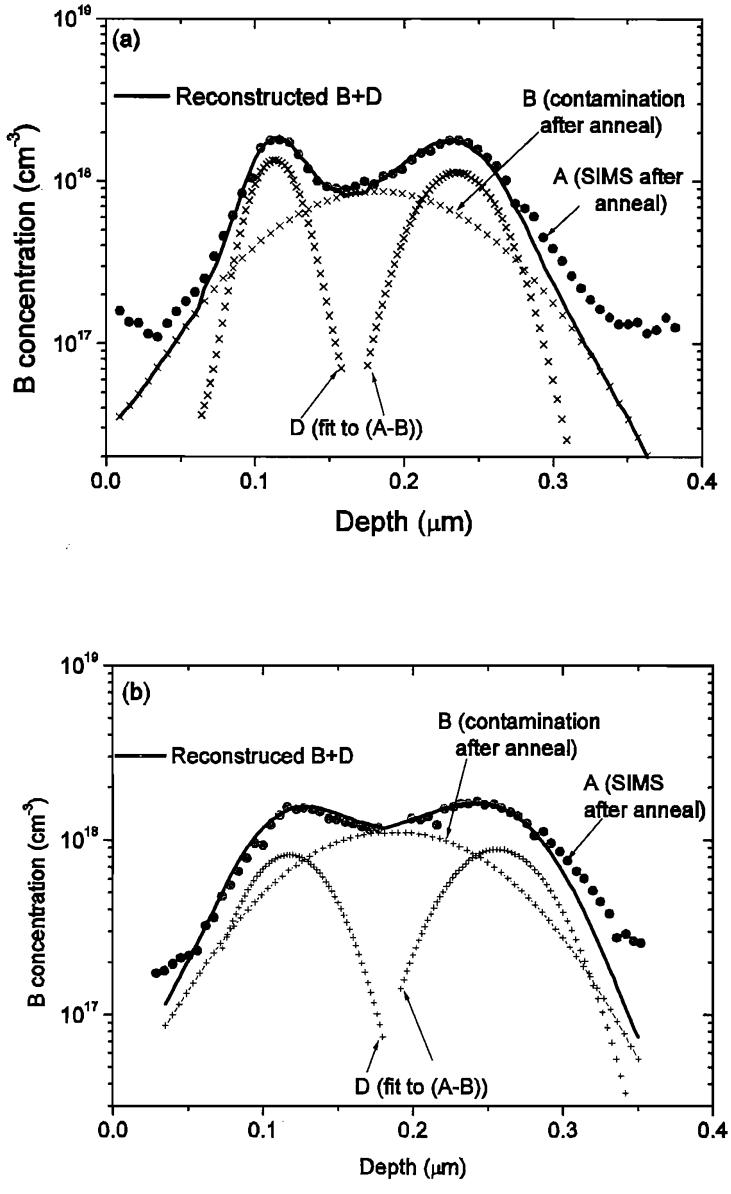

Fig. 4.11. Comparison between the reconstructed boron profile (B+D) and the measured SIMS after anneal (A) for samples inert annealed at 1000 °C for 15s (a) and 120s (b). The reconstructed boron profile was obtained by addition of contamination after anneal (B) and fit to the profile (A-B).

Chapter 5

Study of Fluorine Behaviour under Point Defect Injection

5.1. Introduction

Although the effect of fluorine is well documented in the literature, its mechanism in suppressing boron diffusion is still under research. Fluorine profiles in crystalline silicon after high temperature anneal (1000°C) do not show a typical Gaussian diffusion profile but instead various fluorine SIMS peaks in different regions of the profile, as illustrated in Fig. 5.1 [18]. Fluorine diffuses very fast, showing significant diffusion at temperatures as low as 600°C [100]. It has been proposed that the fluorine peaks are due to F trapping at different regions of residual damage such as end-of-range defects, the amorphous/crystalline interface and vacancy-fluorine clusters [12, 97]. In this chapter, experiments are performed to better understand the physical nature of the different fluorine peaks seen after high temperature anneal.

Point defect injection studies are performed to study how the fluorine SIMS peaks are influenced by the injection of interstitials and vacancies from the surface. Boron diffusion under point defect injection is studied by placing boron marker layers at depths coinciding with the typical depths of the fluorine peaks. In this chapter, the results on the effect of point defect injection on the fluorine profiles are presented. The effects of fluorine on the diffusion of boron marker layers at different depths under different point defect injections are presented in the next chapter.

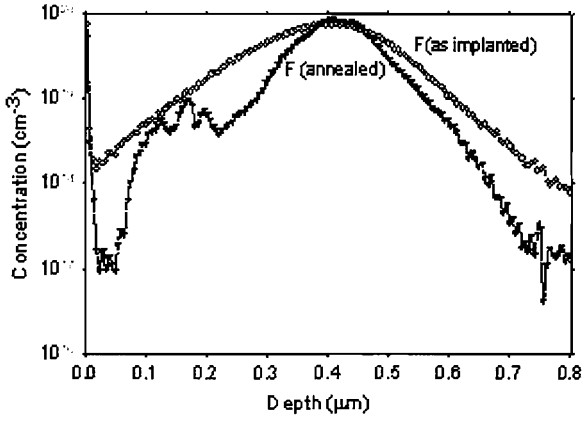

Fig. 5.1. Fluorine SIMS profiles after a 185 keV, 2.3 x 10^{15} cm^{-2} F^+ implant and after anneal at 1000 °C for 30s in nitrogen, after El Mubarek et al [18].

5.2. Experimental Procedure

Boron-doped silicon epitaxial layers were used in this experiment. The detailed information on the samples and anneal conditions are shown in Table 5.1. The growth of these layers was presented in Chapter 4. Samples from Batch 1 contain one B marker at a depth of 0.15 μm with a peak concentration of ~ 7x 10^{17} cm^{-3} (refer to Fig. 4.3(b) in Chapter 4). Samples from Batch 2 contain four boron marker layers located at depths of 0.12, 0.24, 0.45 and 0.67 μm as shown in Fig. 5.2. Each boron marker has a peak concentration of approximately $3x10^{18}$ cm^{-3} and width of ~30 nm at a concentration of $1x10^{17}$ cm^{-3}. The boron marker layer depths were chosen to coincide with the major peaks on the fluorine profile and with the end of the fluorine profile. The peak concentration of the marker layer of ~$3x10^{18}$ cm^{-3} ensures the intrinsic boron diffusion [99].

A 185keV, 2.3 $x10^{15}$ cm^{-2} F^+ was implanted into half of the wafer surface by using a photoresist half-mask. Both the implanted and non-implanted sections were divided again into three parts for defect injection study as shown in Fig. 5.3. The first part was covered with low temperature SiO_2 (LTO) and Si_3N_4 layers for inert anneal, the second part was covered with silicon nitride for vacancy injection (V-inj) and the third part was uncovered for interstitial injection (I-inj). The LTO (~100 nm) and Si_3N_4 layers (~130 nm) layers were deposited using Chemical Vapour Deposition and Plasma Enhanced Chemical Vapour Deposition at 400°C and 300°C respectively.

The wafer was then cut into 1cm x1cm pieces and annealed at 1000 °C for 10-180s in an oxygen atmosphere using the RTA system, Heatpulse-610. Dummy pieces were used along with the work samples to complete a four-inch wafer area on the RTA platen to minimise heat loss around the perimeter of the 1cm x 1cm samples. The LTO and nitride layers were stripped before Secondary Ion Mass Spectroscopy (SIMS) analysis. Transmission electron microscopy (TEM) analysis was also performed on some samples.

	Sample description	Anneal time (s)	Defect injection conditions	SIMS	TEM
Batch 1	Epitaxial silicon with 1 B marker layer	10, 30 180	Inert, I-inj, V-inj Inert, I-inj	F, B F	10s
Batch 2	Epitaxial silicon with 4 B marker layer	15 45 120	Inert, I-inj, Inert, I-inj, V-inj Inert, I-inj, V-inj	F, B F, B F, B	
Batch 3	Crystalline silicon	5, 120			120s

Table 5.1. Details of samples, their anneal conditions and analyses used in defect injection studies

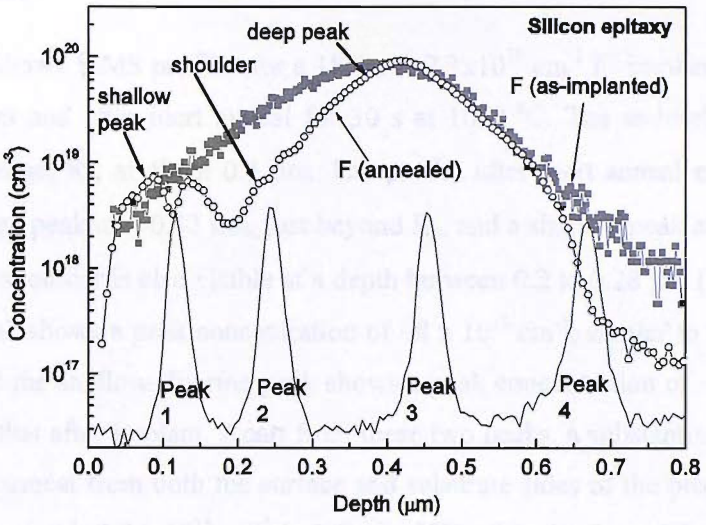

Fig. 5.2. SIMS profiles of boron marker layers after growth showing the location of the four boron peaks with respect to the fluorine profiles after implant and anneal.

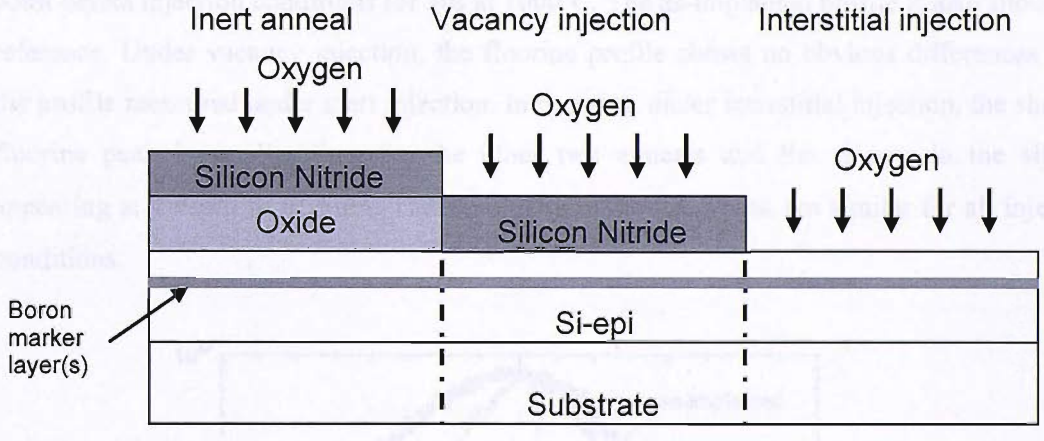

Fig. 5.3. Different surface layers utilised in samples for point defect injection: Silicon Nitride and LTO oxide layers for inert annealing, Silicon Nitride layer for vacancy injection and bare silicon surface for interstitial injection

5.3. Results

Figure 5.4 shows SIMS profiles for a 185keV, $2.3x10^{15}$ cm^{-2} F^+ implant into Batch 1 samples after implant and after inert anneal for 30 s at 1000 °C. The as-implanted profile shows a projected range, R_p, at about 0.4 μm. The profile after inert anneal exhibits two distinctive peaks: a deep peak at ~ 0.42 μm, just beyond R_p, and a shallow peak at a depth of ~ 0.13 μm (0.3 R_p). A shoulder is also visible at a depth between 0.2 to 0.28 μm (0.5~0.7 Rp). The deep fluorine peak shows a peak concentration of ~8 x 10^{19} cm^{-3}, similar to the concentration after implant and the shallow fluorine peak shows a peak concentration of ~5 x 10^{18} cm^{-3}, slightly lower than that after implant. Apart from these two peaks, a substantial amount of fluorine is lost during anneal from both the surface and substrate sides of the profile. The fluorine dose after inert anneal is 1.2 x 10^{15} cm^{-2} and thus ~ 50% of the implanted dose has been lost during anneal.

Figure 5.5 shows the fluorine profiles for Batch 1 samples after annealing under different point defect injection conditions for 30s at 1000°C. The as-implanted profile is also shown for reference. Under vacancy injection, the fluorine profile shows no obvious differences from the profile measured under inert injection. In contrast, under interstitial injection, the shallow fluorine peak is smaller than for the other two anneals and lies deeper in the silicon, appearing at a depth of 0.15μm. The shoulder and the deep peak are similar for all injection conditions.

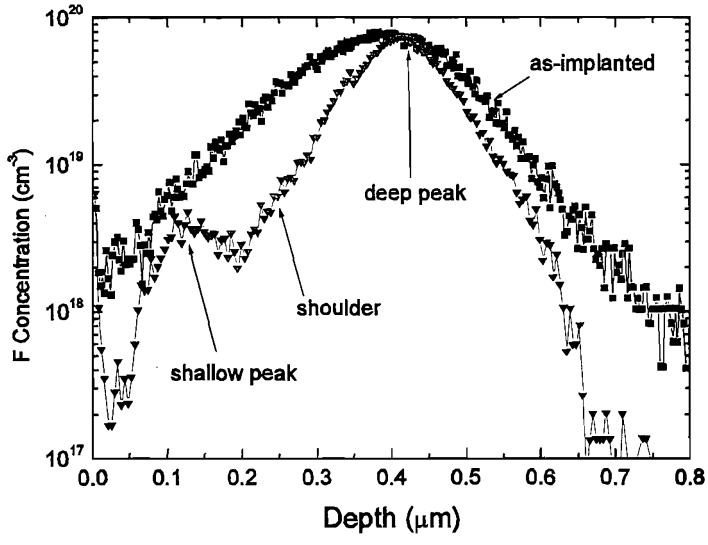

Fig. 5.4. Fluorine SIMS profiles after a 185 keV, 2.3 x 10^{15} cm^{-2} F^+ implant and after a 30 s inert anneal at 1000 °C.

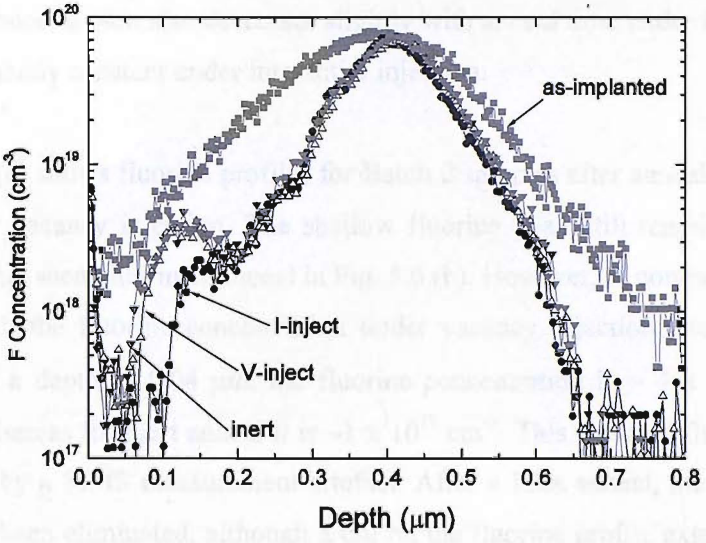

Fig. 5.5.. Fluorine SIMS profiles after a 185 keV, 2.3 x 10^{15} cm^{-2} F^+ implant and after anneal for 30 s at 1000 °C under interstitial injection (I-inject), vacancy injection (V-inject) and inert anneal conditions

To further investigate this behaviour, more anneals were performed using samples from RTA Batch 2 for a range of times (15, 45 and 120s) for each injection condition. Figure 5.6 (a) shows the evolution of the fluorine profiles over time for samples under interstitial injection. One significant observation is the dramatic change in the shallow fluorine peak with anneal time. It is already present after a 15s anneal, and is completely eliminated after a 45s anneal. The shoulder, which is noticeable even after the 15s anneal, decreases in size with anneal time. As for the deep fluorine peak, the peak concentration is approximately constant with anneal time, but the fluorine dose decreases slightly with increasing anneal time.

For comparison, Fig. 5.6 (b) shows the evolution of the fluorine profiles under inert anneal for Batch 2 samples annealed at 1000°C for 15, 45 and 120s. Similar to the trend seen under interstitial injection, the shallow peak decreases in size with increasing anneal time. The shallow peak after the 15s inert anneal is bigger than under interstitial injection, with a peak fluorine concentration of 8 x 10^{18} cm^{-3}, compared with 6 x 10^{18} cm^{-3} after interstitial injection. Moreover, the shallow peak is still present after a 45s inert anneal, whereas it was absent under interstitial injection. These results show that the shallow peak is more stable under inert anneal than under interstitial injection. For the longer anneal time of 120s, the shallow peak is completely eliminated. The shoulder also decreases in size with anneal time. For a given anneal time, more fluorine seems to be retained in the shallow peak and the shoulder under inert anneal than under interstitial injection, as will be later confirmed by integrating the

fluorine doses. As for the deep peak, the fluorine dose decreases with increasing anneal time. The peak concentration also decreases slightly with anneal time under inert anneal where as it is approximately constant under interstitial injection.

Figure 5.6 (c) shows fluorine profiles for Batch 2 samples after anneal at 1000 °C for 45 and 120s under vacancy injection. The shallow fluorine peak still remains after a 45s anneal, similar to that seen after inert anneal in Fig. 5.6 (b). However, in contrast to the profile for the inert anneal, the fluorine concentration under vacancy injection rises on approaching the surface. At a depth of 0.04 μm, the fluorine concentration is ~ 4 x 10^{17} cm^{-3} for vacancy injection whereas for inert anneal it is ~1 x 10^{17} cm^{-3}. This elevated fluorine concentration is not caused by a SIMS measurement artefact. After a 120s anneal, the shallow fluorine peak has almost been eliminated, although a tail on the fluorine profile extends from the shoulder towards the surface. The fluorine concentration reaches a minimum at a depth of 0.1 μm and then rises towards the surface, as was seen for the 45s anneal. For both 45 s and 120 s anneals, the fluorine concentration in the shoulder is higher under vacancy injection than under inert anneal. For example for the 45s anneal, the fluorine concentration at a depth of 0.2 μm is ~4 x 10^{18} cm^{-3} under vacancy injection, compared with ~3 x 10^{18} cm^{-3} under inert anneal. This is due to the tail on the fluorine profile that extends from the shoulder towards the surface. As for the deep peak, the peak concentration decreases significantly with increasing anneal time.

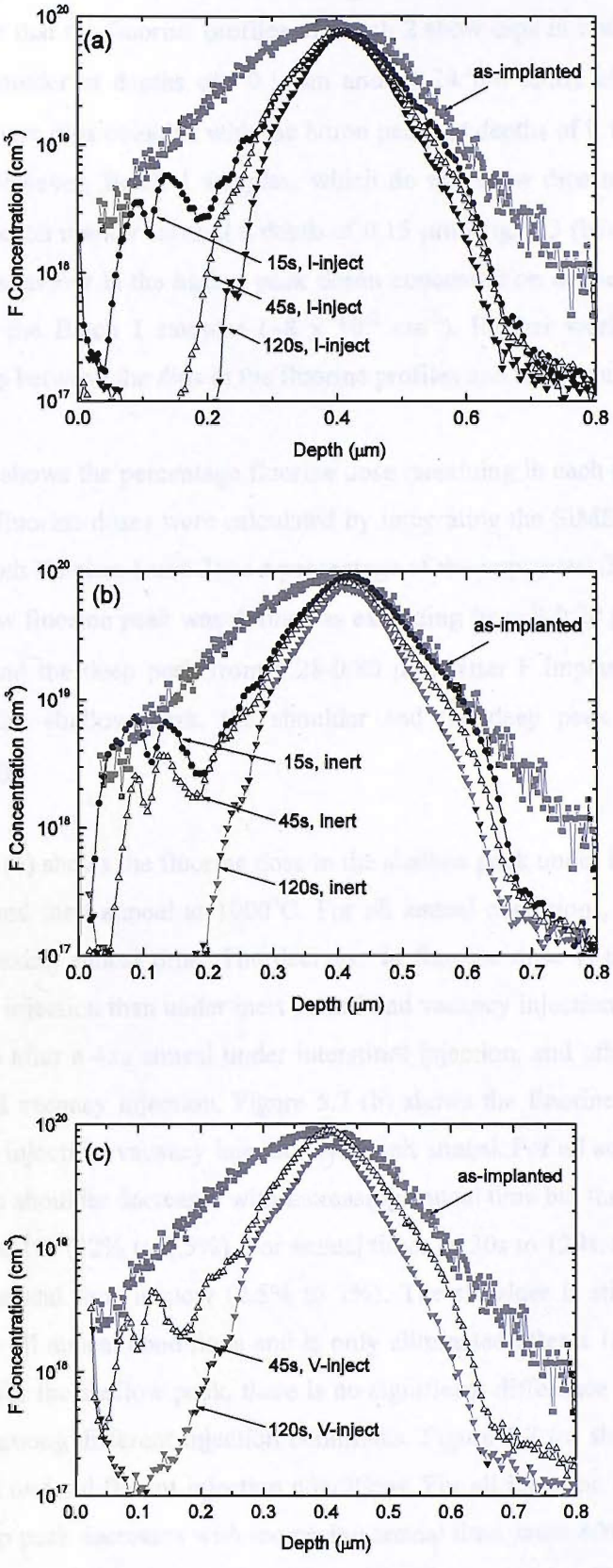

Fig. 5.6. Fluorine SIMS profiles for samples implanted with 185 keV, 2.3 x 10^{15}cm^{-2} F^+ and annealed for different times at 1000 °C under (a) interstitial injection conditions (b) inert conditions and (c) vacancy injection conditions. The as-implanted fluorine profile is shown for comparison.

Comparing the fluorine profiles for Batch 2 in Fig. 5.6 with those for Batch 1 in Fig. 5.4, it can be seen that the fluorine profiles of Batch 2 show dips in both the shallow fluorine peak and the shoulder at depths of ~0.1 μm and ~0.24 μm under all injection conditions. The depths of these dips coincide with the boron peaks at depths of 0.12 and 0.24 μm as shown in Fig. 5.2. However, Batch 1 samples, which do not show dips in the fluorine profiles, also contain a boron marker layer at a depth of 0.15 μm (Fig. 4.3 (b)). One possible cause of this different behaviour is the higher peak boron concentration in the Batch 2 samples (3 x 10^{18} cm^{-3}) than the Batch 1 samples (~8 x 10^{17} cm^{-3}). Further work is needed to confirm the relationship between the dips in the fluorine profiles and the boron marker layers.

Figure 5.7 shows the percentage fluorine dose remaining in each peak as a function of anneal time. The fluorine doses were calculated by integrating the SIMS profiles shown in Figs. 5.5 and 5.6 (both Batches 1 and 2) as a percentage of the implanted fluorine dose ($2.3x10^{15}$ cm^{-2}). The shallow fluorine peak was defined as extending from 0-0.20 μm, the shoulder from 0.20-0.28 μm and the deep peak from 0.28-0.80 μm. After F implant (0 s anneal), the fluorine doses in the shallow peak, the shoulder and the deep peak are 6.5%, 12% and 80% respectively.

Figure 5.7 (a) shows the fluorine dose in the shallow peak under interstitial injection, vacancy injection and inert anneal at 1000°C. For all anneal conditions, the fluorine dose decreases with increasing anneal time. The decrease in fluorine dose is noticeably more rapid under interstitial injection than under inert anneal and vacancy injection. The shallow peak has been eliminated after a 45s anneal under interstitial injection, and after a 120s anneal under inert anneal and vacancy injection. Figure 5.7 (b) shows the fluorine dose in the shoulder under interstitial injection, vacancy injection and inert anneal. For all anneal conditions, the fluorine dose in the shoulder decreases with increasing anneal time but the decrease is extremely rapid for the first 10s (12% to 2.5%). For anneal times of 30s to 120s, the decrease in fluorine dose with the anneal time is slow (2.5% to 1%). The shoulder is still present even after a 120s anneal for all anneal conditions and is only eliminated after a 180s anneal. Unlike the trend observed for the shallow peak, there is no significant difference in the dose remaining in the shoulder among different injection conditions. Figure 5.7 (c) shows the fluorine dose in the deep peak under different injection conditions. For all injection conditions, the fluorine dose in the deep peak decreases with increasing anneal time, from 80% to 60% in the first 10s and from 60% to 40% in the next 170s. Half of the fluorine dose still remains after a 180s anneal. The decrease of dose in the deep peak does not show any obvious differences among the different injection conditions.

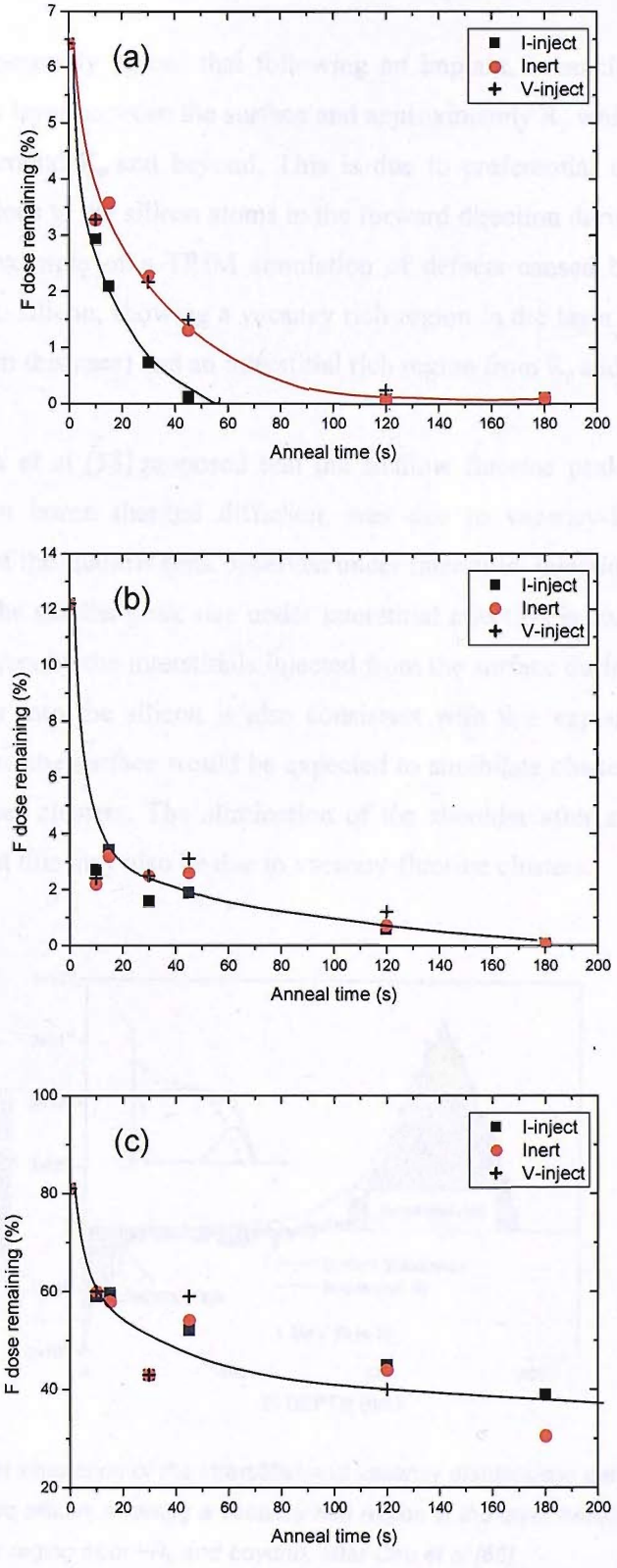

Fig. 5.7. Fluorine dose remaining under different injection conditions as a function of anneal time for samples implanted with 185 keV, 2.3 x $10^{15}cm^{-2}$ F^+ and annealed at 1000 °C. Fig. 5.7(a) shows F dose remaining in the shallow peak, (b) in the shoulder and (c) in the deep fluorine peak.

5.4. Discussion

It is now generally agreed that following an implant, vacancies are the dominating defect species in a layer between the surface and approximately R_p while self-interstitials are mainly observed around R_p and beyond. This is due to preferential momentum transfer from the impinging ions to the silicon atoms in the forward direction during implant [7, 66]. Figure 5.8 shows an example of a TRIM simulation of defects caused by a 1MeV, 1x 10^6 cm^{-2} Si^+ implant into silicon, showing a vacancy rich region in the layer between the surface and ~R_p (~1300nm in this case) and an interstitial rich region from R_p and beyond [66].

El Mubarek et al [18] proposed that the shallow fluorine peak, which is responsible for a reduction in boron thermal diffusion, was due to vacancy-fluorine (V-F) clusters. The behaviour of the shallow peak observed under interstitial injection in Fig. 5.5 tends to support this idea. The smaller peak size under interstitial injection is consistent with the annihilation of V-F clusters by the interstitials injected from the surface during annealing. The shift of the peak deeper into the silicon is also consistent with this explanation, since the interstitials injected from the surface would be expected to annihilate clusters lying closer to the surface before deeper clusters. The elimination of the shoulder after a 120s anneal in Fig. 5.6 (a) suggests that this may also be due to vacancy-fluorine clusters.

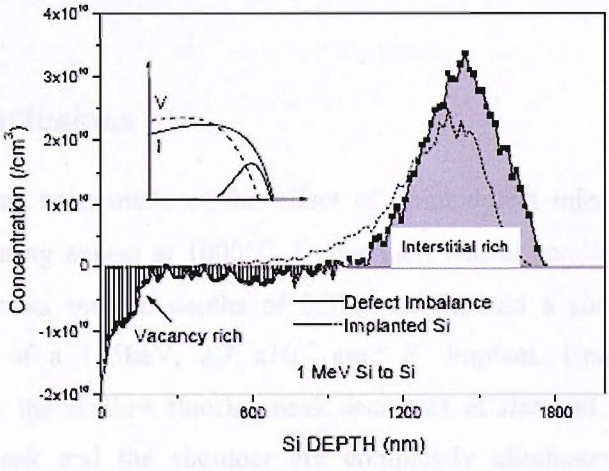

Fig. 5.8. TRIM simulation of the interstitial and vacancy distributions generated by a 1 MeV, 1x10^6 cm^{-2} Si$^+$ implant into silicon, showing a vacancy rich region in the layer between the surface and ~R_p and an interstitial rich region from ~R_p and beyond, after Chu et al [66].

These results are consistent with the work of Pi et al [101] who used positron annihilation spectroscopy (PAS) to study fluorine profiles and suggested that vacancy dominated V-F clusters are formed in the region of 0~0.5R_p and fluorine dominated V-F clusters are formed

in the region of $0.5R_p$~$1.3R_p$. In our work, the shallow fluorine peak lies between 0.2~$0.5R_p$ and the shoulder lies between 0.5~$0.7R_p$ (Fig. 5.4). These depths broadly correspond to the work of Pi et al and suggest that the shallow fluorine peak may be due to vacancy-rich V-F clusters and the shoulder to fluorine-rich V-F clusters.

Comparison between Figs. 5.6(a) and 5.6(b) clearly show that the V-F clusters are annihilated in a shorter time under interstitial injection than inert anneal. This effect can be explained by the extra interstitials injected from the surface under interstitial injection. However, even under interstitial injection, V-F clusters are stable for an anneal time of up to 30s at 1000°C. This anneal condition is sufficient for many applications in device fabrication. Under inert anneal, V-F clusters are stable for even longer times.

While the vacancy fluorine clusters are annihilated under interstitial injection, Fig. 5.5 shows that they are unchanged under vacancy injection. The vacancy injection occurs due to the compressive strain at the silicon caused by the deposited nitride layer and thus its effect is dependent on the thickness of the layer [88]. The retardation of boron diffusion by vacancy injection is not as strong as the enhancement of boron diffusion caused by interstitial injection for a given nitride thickness [89]. Further anneals with a thicker nitride layer or a longer anneal time under vacancy injection condition will be necessary to see an effect on the vacancy fluorine clusters.

5.5. Conclusions

A study has been made of the effect of point defect injection on ion implanted fluorine profiles during anneal at 1000°C. Under inert anneal conditions, SIMS analysis has shown fluorine peaks seen at depths of $0.3R_p$ and R_p, and a shoulder between 0.5~$0.7R_p$ after annealing of a 185keV, 2.3 $x10^{15}$ cm^{-2} F^+ implant. Under interstitial injection anneal conditions, the shallow fluorine peak decreases in size and for long anneal times, both the shallow peak and the shoulder are completely eliminated. This result provides strong evidence that the shallow peak and the shoulder are due to vacancy-fluorine clusters. The elimination of both the shallow fluorine peak and the shoulder can be explained by the annihilation of vacancies in the clusters by recombination with injected interstitials. It is proposed that the shallow fluorine peak is due to vacancy-rich clusters and the shoulder is due to fluorine-rich clusters.

Chapter 6

Reduced Boron Diffusion under Point Defect Injection in Fluorine Implanted Silicon

6.1. Introduction

Point defect injection studies are performed to better understand the physical nature of the different fluorine peaks seen after high temperature anneal. The results on the effect of point defect injection on the fluorine profiles have been presented in Chapter 5. In this chapter, boron diffusion under point defect injection is studied by placing boron marker layers at depths coinciding with the typical depths of the fluorine peaks. The effects of fluorine on the diffusion of boron marker layers at different depths under different point defect injections are presented. To understand the fluorine mechanism in suppressing boron diffusion, correlations are made between the boron and fluorine profiles.

The experimental procedure has been presented in section 5.2 of the previous chapter. Boron marker layers from the Batch 2 sample is shown again in Fig. 6.1. Boron peak 1 was chosen to coincide with the shallow fluorine peak, peak 2 with the shoulder, peak 3 with the deep peak and peak 4 beyond the deep peak. Each boron marker has a width of ~30 nm at a concentration of $1x10^{17}$ cm^{-3} and a peak concentration of approximately $3x10^{18}$ cm^{-3}, which ensures the intrinsic boron diffusion [99].

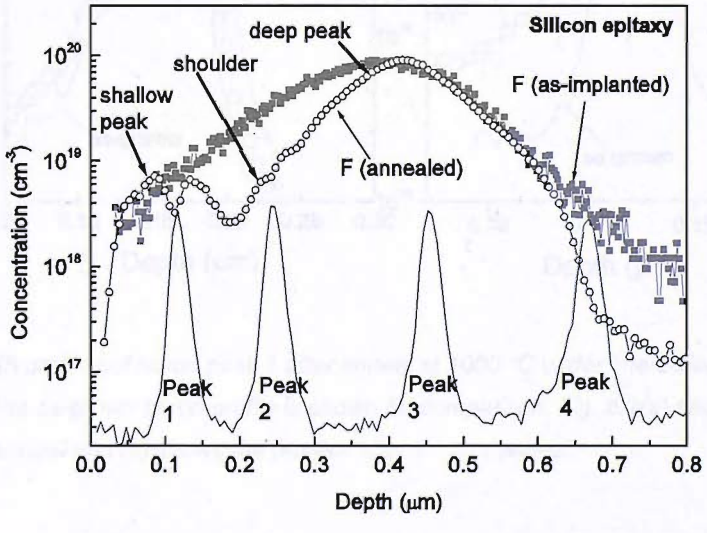

Fig. 6.1. SIMS profiles of boron marker layers after growth showing the location of the four boron peaks with respect to the fluorine profiles after implant and anneal.

6.2. Results

6.2.1. Boron peak 1

Figure 6.2 shows boron SIMS profiles of unimplanted samples annealed at 1000°C under inert and interstitial injection conditions for 30s (a) and 120s (b). The 30s anneal sample is from batch 1 and the 120s anneal sample is from batch 2. The as-grown boron profile is also shown for reference. Boron diffusion is enhanced under interstitial injection compared to inert anneal for both anneal times of 30s and 120s. This is an expected result since boron diffusion is mediated by interstitials and the interstitial injection from the surface enhances boron diffusion [38].

Figure 6.3 shows the corresponding boron SIMS profiles of samples given a prior 185keV, $2.3\times10^{15}cm^{-2}$ F^{+} implant. For a 30s anneal (Fig. 6.3(a)), the same amount of boron diffusion is obtained for interstitial injection and inert anneal, suggesting that the effect of interstitial injection is not seen in the fluorine implanted sample. This is in contrast to the behaviour observed in the unimplanted sample in Fig. 6.2(a). For a longer anneal of 120s (Figure 6.3(b)), interstitial injection enhances boron diffusion compared to the inert anneal, similar to the behaviour observed in the unimplanted sample in Fig. 6.2(b).

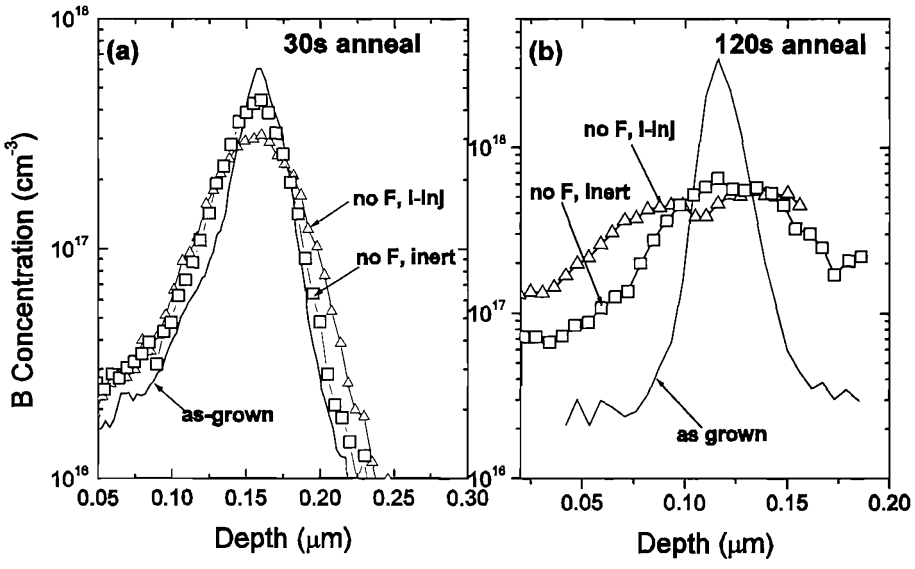

Fig. 6.2. SIMS profiles of boron peak 1 after anneal at 1000 °C under interstitial injection and inert conditions. The as-grown boron profile is shown for comparison. Fig. 6.2(a) shows the boron profiles after a 30 s anneal and (b) shows the profiles after a 120 s anneal.

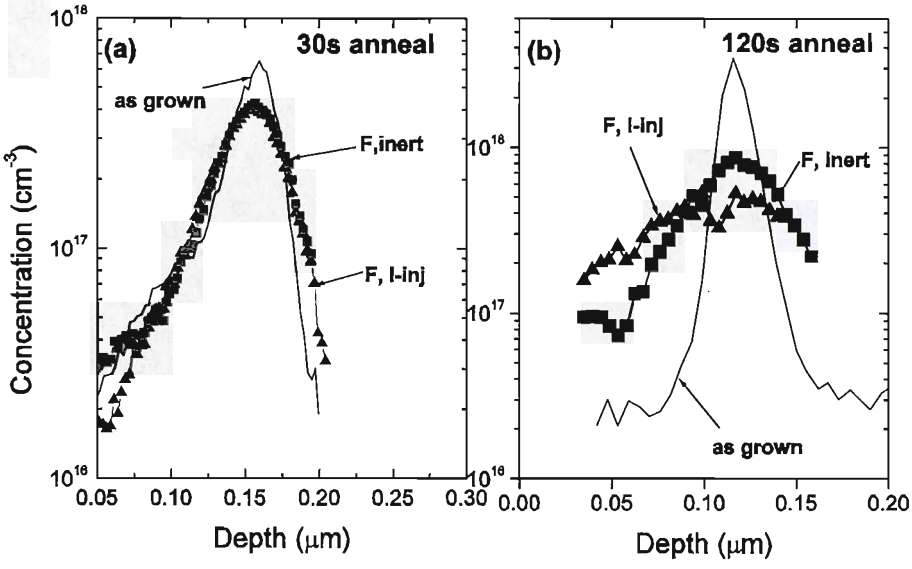

Fig. 6.3. SIMS profiles of boron peak 1 after a 185 keV, 2.3 x 10^{15} cm^{-2} F^+ implant and an anneal at 1000 °C under interstitial injection and inert conditions. The as-grown boron profile is shown for comparison. Fig. 6.3(a) shows the boron profiles after a 30 s anneal and (b) shows the profiles after a 120 s anneal.

To further investigate the effect of fluorine on boron diffusion, we compare in Figure 6.4 the fluorine implanted and unimplanted boron SIMS profiles of batch 2 samples after anneal at 1000°C for 15s (a) and 120s (b) under interstitial injection conditions. The as-grown boron profile is also shown for reference. For the 15s anneal under interstitial injection, the fluorine implanted sample shows a much smaller boron diffusion than the unimplanted sample. For a longer anneal of 120s, both fluorine implanted and unimplanted samples show the same amount of boron diffusion. Therefore, for a short anneal time, fluorine strongly suppresses boron diffusion even in the presence of interstitial injection from the surface.

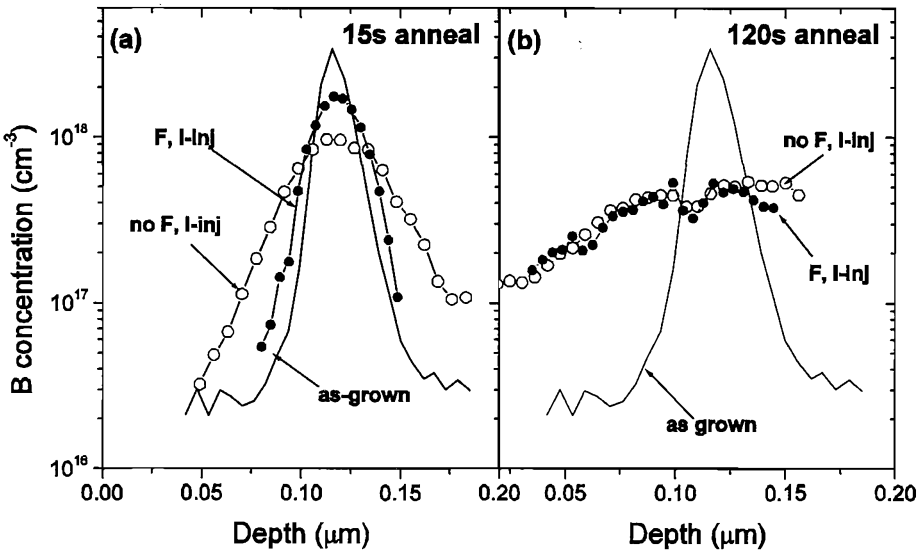

Fig. 6.4. Comparison of boron SIMS profiles in fluorine implanted (185 keV, 2.3 x 10^{15} cm^{-2}) and unimplanted samples annealed at 1000 °C under interstitial injection. The as-grown boron profile is shown for comparison. Fig. 6.4(a) shows the boron profiles after a 15 s anneal and (b) shows the profiles after a 120 s anneal.

The SIMS profiles in Figs. 6.2-6.4 were used to extract boron diffusion coefficients using the parameter optimizer available in the ATHENA software (SSUPREM4) [92]. The detail simulation procedure is presented in section 4.5 in Chapter 4. Typical fits to the measured profiles are shown for boron peak 1 in Fig. 6.5 for unimplanted (a) and fluorine implanted (b) samples under interstitial injection conditions for anneal times of 15 to 120s. The average fitting error varies from ~5% for a short anneal time (15s) to ~20% for a long anneal time (120s), as presented in detail in Chapter 4. It should be noted that only the left hand sides of the annealed profiles are fitted, especially for longer anneals, because of the close proximity of peak 2. Fig. 6.6 shows the time-averaged diffusion coefficients for boron peak 1 as a function of anneal time. Four different anneal conditions are plotted: (i) unimplanted, inert anneal (no F, inert), (ii) unimplanted, interstitial injection (no F, I-inj), (iii) fluorine implanted, inert anneal (F, Inert) and (iv) fluorine implanted, interstitial injection (F, I-inj). For the unimplanted samples given an inert anneal, the diffusion coefficient is constant, with a value of 3.1 x 10^{-14} cm^2/s which is slightly larger than the value of 1.53 x 10^{-14} cm^2/s reported by Fair for intrinsic boron diffusion [99]. The diffusion coefficient under interstitial injection also shows a constant value for all anneal times. This indicates that interstitials are injected into the silicon at a constant rate for times up to 120s. Our results are in accordance with the linear oxidation expected for short anneal (oxidation) times since the surface reaction is the rate-limiting factor [6]. This enhancement, which is independent of the anneal time, is in agreement with previous reports by Skarlatos et al [102] and Park et al [103] who also used

boron marker layers and dry O_2 oxidation at 900°C for times 30min- 4hours. Under interstitial injection, the boron diffusion coefficient has a value of 1.2 x 10^{-13} cm^2/s, which is a factor of 3.8 higher than for the inert anneal.

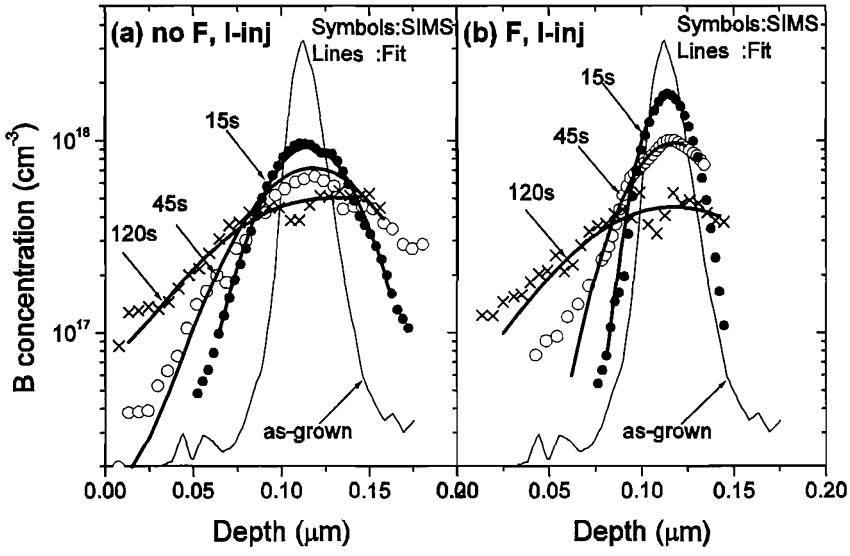

Fig. 6.5. Simulated and measured boron profiles after an anneal at 1000 °C for different times under interstitial injection for unimplanted (a) and fluorine implanted (185 keV, 2.3 x 10^{15} cm^{-2}) samples. The as-grown boron profile is shown for reference.

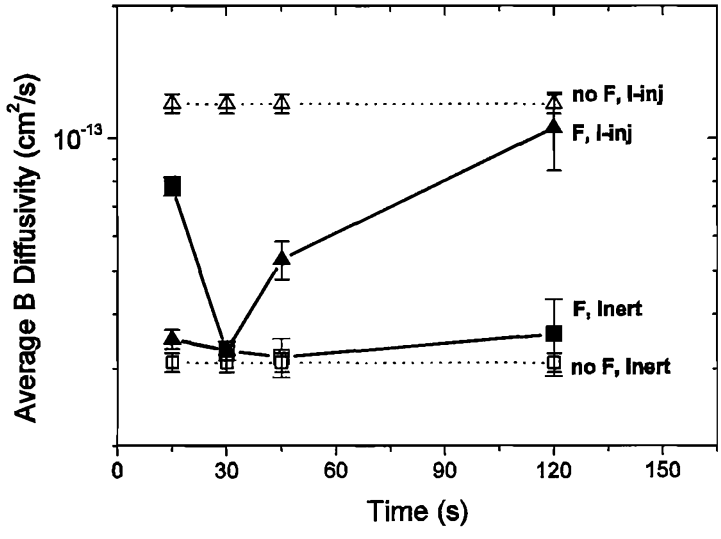

Fig. 6.6. Average boron diffusion coefficient of boron peak 1 as a function of anneal time for fluorine implanted (185 keV, 2.3 x 10^{15} cm^{-2}) and unimplanted samples annealed at 1000 °C under interstitial injection and inert conditions.

For the fluorine implanted samples, the diffusion coefficient varies with time. The diffusion coefficient obtained under interstitial injection is initially approximately constant for anneal times of 15 and 30 s and similar to the value obtained for an inert anneal in an unimplanted sample (3.1 x 10^{-14} cm^2/s). It then increases strongly with anneal time and approaches the value obtained for an unimplanted sample under interstitial injection (1.2 x 10^{-13} cm^2/s). This indicates that fluorine becomes progressively less effective in suppressing boron diffusion as the anneal time increases. Under inert anneal conditions, a similar trend is seen but the low value of diffusion coefficient is obtained for longer anneal times. For anneal times of 30 and 45 s, the diffusion coefficient is approximately the same as that for an inert anneal in an unimplanted sample (3.1 x 10^{-14} cm^2/s) and then increases slightly for an anneal time of 120 s to a value of 4 x 10^{-14} cm^2/s. However, the 15 s anneal gives a diffusion coefficient of 8x 10^{-14} cm^2/s, a value much higher than expected which deviates from the trend. Further investigation is required to confirm this result.

In summary, the results of boron peak 1 show that fluorine strongly suppresses boron diffusion for short time anneals even under interstitial injection conditions. However, this effect reduces as the anneal time increases.

6.2.2. Boron peak 2

The effect of fluorine on the diffusion of boron peak 2 under different anneal conditions is presented in this section. Boron peak 2 is located in the fluorine shoulder as shown in Fig. 6.1. Figure 6.7 compares boron profiles under inert and interstitial injection conditions after anneal at 1000°C for 15s (a), 45s (b) and 120s (c). For a 15s anneal in Fig. 6.7 (a), the boron diffusion is less under interstitial injection than inert anneal. This is a surprising result and is the opposite behaviour to that seen in Fig. 6.2 for sample without a fluorine implant. This unexpected behaviour is no longer seen for the longer anneal of 45s and 120s, where boron diffusion under interstitial injection and inert anneal are similar (Fig. 6.7(b) and (c)).

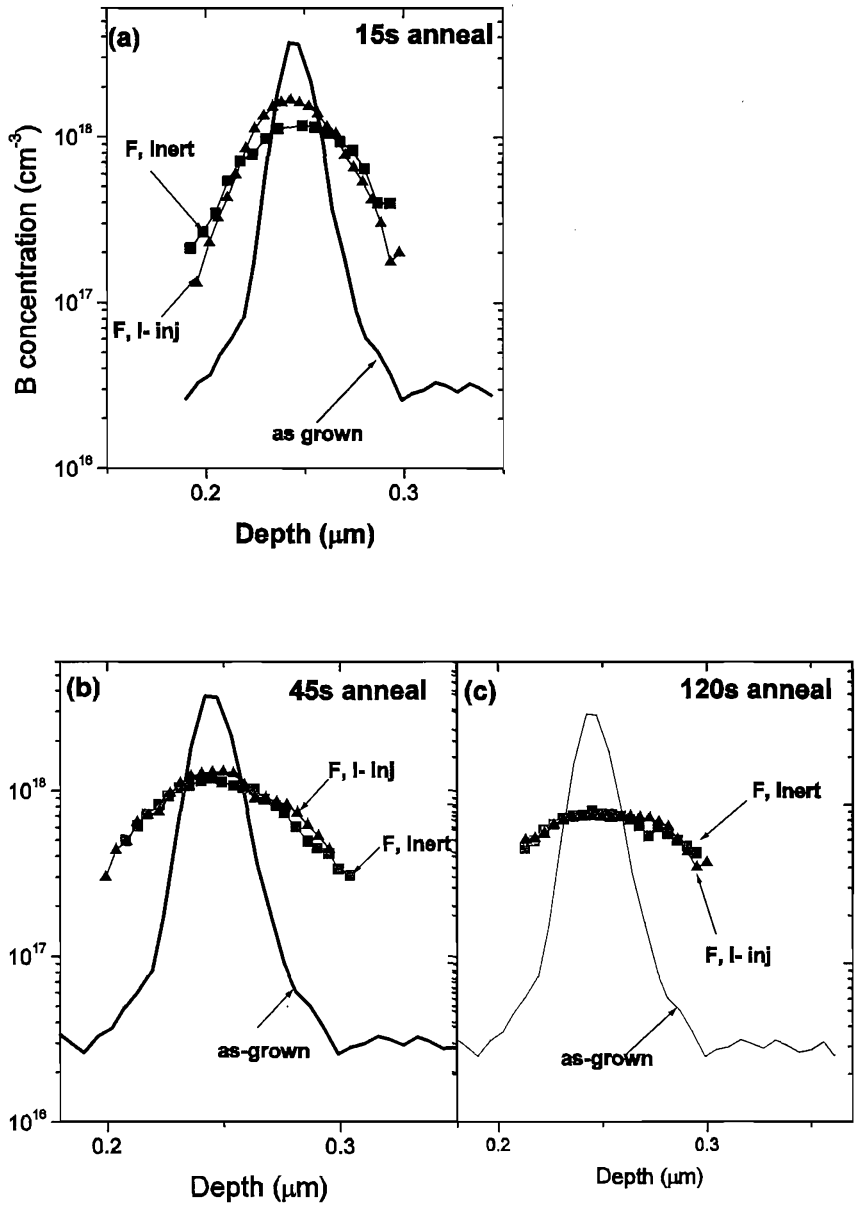

Fig. 6.7. SIMS profiles of boron peak 2 after a 185 keV, 2.3 x 10^{15} cm^{-2} F^+ implant and an anneal at 1000 °C under interstitial injection and inert conditions. The as-grown boron profile is shown for comparison. Fig. 6.7(a) shows the boron profiles after a 15s anneal, (b) a 45s anneal and (c) a 120 s anneal.

To further investigate the effect of fluorine on boron diffusion, Figure 6.8 compares fluorine implanted and unimplanted boron SIMS profiles after anneal at 1000°C for 15s (a), 45s (b) and 120s (c) under interstitial injection condition. For the 15s anneal, the fluorine implanted sample shows a similar amount of boron diffusion for both fluorine implanted and unimplanted samples, while for the 120s anneal, less boron diffusion is observed in the fluorine implanted sample than in the unimplanted sample. These results show that for boron peak 2 under interstitial injection, fluorine suppresses boron diffusion at long anneal times

but not at short anneal times. This is the opposite trend to that seen for peak 1 in Fig. 6.4, where fluorine suppresses boron diffusion at short anneal times, but not at long anneal times.

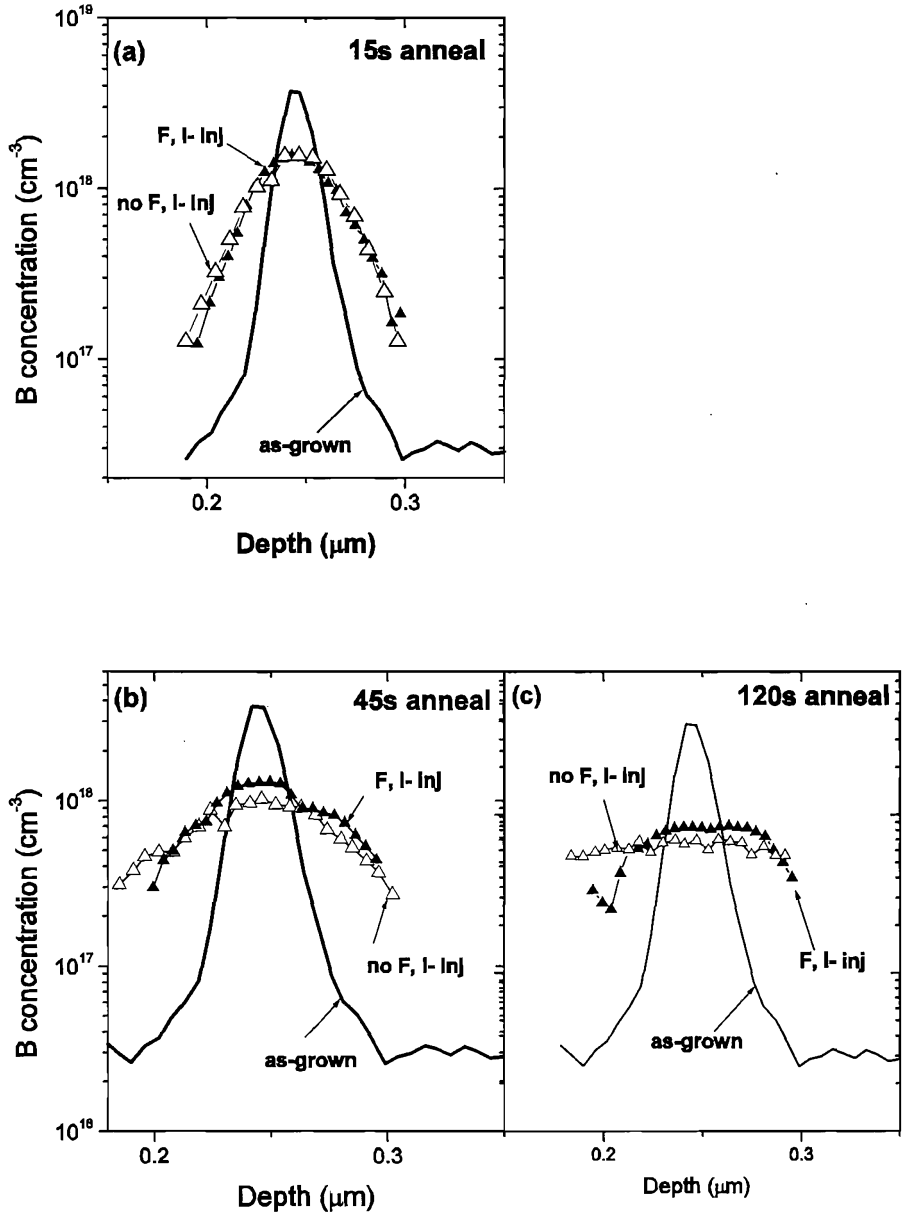

Fig. 6.8. Comparison of boron SIMS profiles in fluorine implanted (185 keV, 2.3 x 10^{15} cm^{-2}) and unimplanted samples annealed at 1000 °C under interstitial injection. The as-grown boron profile is shown for comparison. Fig. 6.8(a) shows the boron profiles after a 15 s anneal, (b) a 45s anneal and (c) a 120 s anneal.

Fig. 6.9 shows the time-averaged diffusion coefficient of boron peak 2 as a function of anneal time. For the fluorine implanted samples under interstitial injection, the diffusion coefficient decreases with increasing anneal time and reaches a value for a 120s anneal that is three times lower than that for the unimplanted sample (4 x 10^{-14} cm^2/s and 1.2 x 10^{-13} cm^2/s). This confirms the trend seen in Fig. 6.8 that fluorine suppresses boron diffusion at long anneal

times. The same trend of decreasing diffusion coefficient with anneal time is observed under inert anneal. However, for an anneal time of 15s, the value of diffusion coefficient under interstitial injection is lower than that under inert anneal. For anneal times of 45s and 120s, the same trend is seen but the difference is small and falls within the error bars of the extracted values of diffusion coefficient. Nevertheless, these results suggest that in the fluorine implanted samples, the injection of interstitials somehow works in a positive way to reduce boron diffusion. These results indicate that the effects of the shallow fluorine peak and the shoulder on boron diffusion are significantly different.

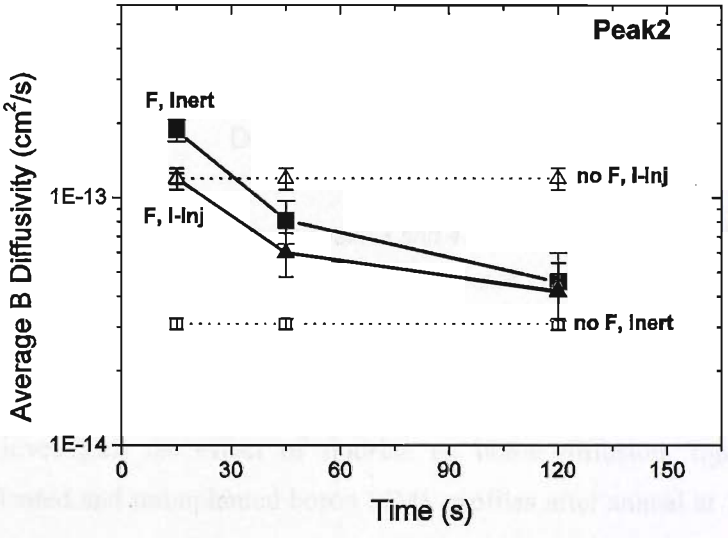

Fig. 6.9. Average boron diffusion coefficient of boron peak 2 as a function of anneal time for fluorine implanted (185 keV, 2.3 x 10^{15} cm^{-2}) and unimplanted samples annealed at 1000 °C under interstitial injection and inert conditions.

6.2.3. Boron peaks 3 and 4

In this section, the effect of fluorine on the diffusion of boron peaks 3 and 4 is studied under different anneal conditions. Since both peaks are located in the deep fluorine peak (see Fig. 6.1), their SIMS data are analysed together. Firstly, we compare in Fig. 6.10 the effect of interstitial injection in the fluorine implanted samples annealed at 1000°C for 15s (a) and 120s (b). For the 15s anneal in Fig. 6.10 (a), both peaks show smaller boron diffusion under interstitial injection than inert anneal. This is a surprising result since boron diffusion is mediated by interstitials and hence it would be expected that the boron diffusion would be greater under interstitial injection than inert anneal. For the longer anneal of 120s in Fig. 6.10 (b), similar behaviour is observed, but the difference is smaller.

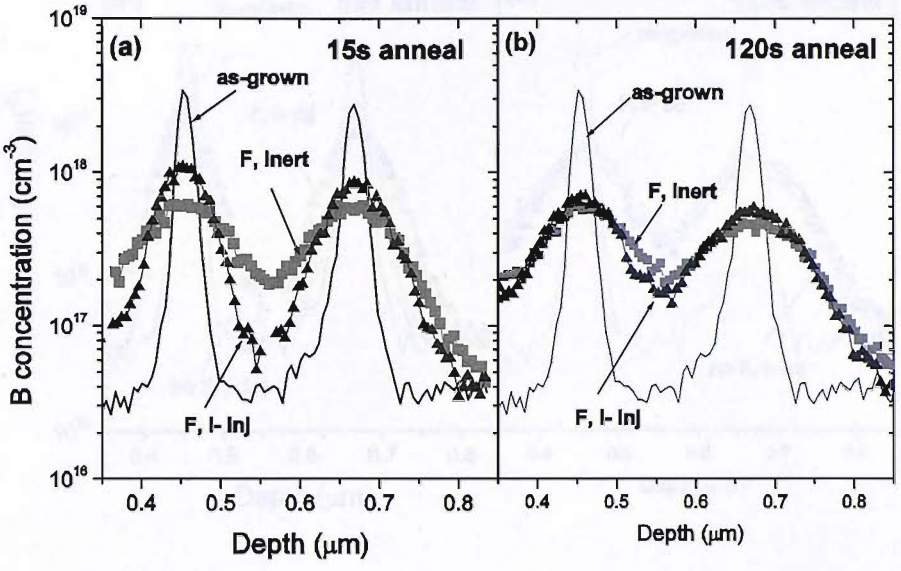

Fig. 6.10. SIMS profiles of boron peaks 3 and 4 after a 185 keV, 2.3 x 10^{15} cm^{-2} F^+ implant and an anneal at 1000 °C under interstitial injection and inert conditions. The as-grown boron profile is shown for comparison. Fig. 6.10 (a) shows the boron profiles after a 30 s anneal and (b) shows the profiles after a 120 s anneal.

To investigate the effect of fluorine on boron diffusion, figure 6.11 compares fluorine implanted and unimplanted boron SIMS profiles after anneal at 1000°C for 15s (a) and 120s (b) under interstitial injection condition. For the 15s anneal, the fluorine implanted sample shows more boron diffusion than the unimplanted sample while for the 120s anneal, approximately the same amount of boron diffusion is observed. The same trends are seen in peak 3 and peak 4. These results show that under interstitial injection, the fluorine implant enhances boron diffusion in peaks 3 and 4 for short anneal times but not for long anneal times.

Figures 6.12 show the time-averaged boron diffusion coefficients as a function of anneal time for peak 3 (left fig.) and peak 4 (right fig.) respectively. For the fluorine implanted samples, both peaks clearly show that the diffusion coefficient decreases with increasing anneal time, similar to the trend observed for boron peak 2. The same trend is seen for interstitial injection and inert anneal, but for anneal times of 15 and 45s, interstitial injection gives less boron diffusion than inert anneal. For an anneal time of 120s, the same trend is seen, but the difference is small and within the error bars. These results confirm the trend seen for peak 2 (Fig. 6.9) and indicate that interstitial injection is somehow working in a positive way to reduce boron diffusion.

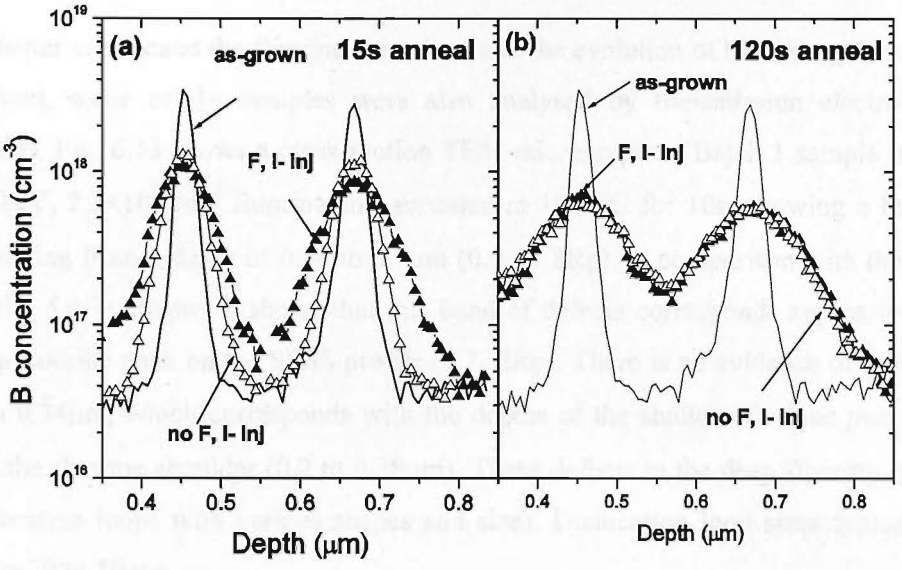

Fig. 6.11. Comparison of boron SIMS profiles of boron peaks 3 and 4 in fluorine implanted (185 keV, 2.3 x 10^{15} cm^{-2}) and unimplanted samples annealed at 1000 °C under interstitial injection. The as-grown boron profile is shown for comparison. Fig. 6.11(a) shows the boron profiles after a 15 s anneal and (b) shows the profiles after a 120 s anneal.

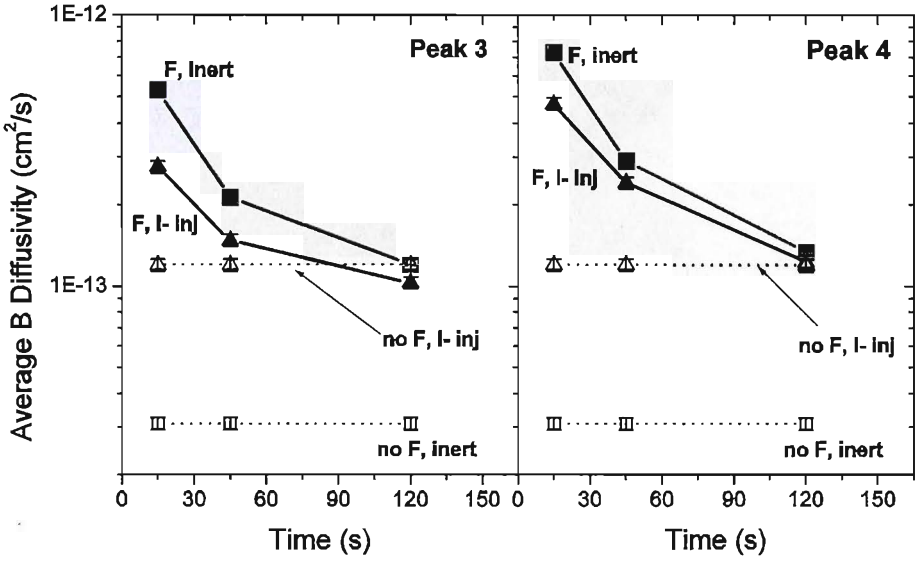

Fig. 6.12. Average boron diffusion coefficient of boron peaks 3 (left) and 4 (right) as a function of anneal time for fluorine implanted (185 keV, 2.3 x 10^{15} cm^{-2}) and unimplanted samples annealed at 1000 °C under interstitial injection and inert conditions.

6.2.4. TEM analysis

To better understand the fluorine behaviour and the evolution of the damage from the fluorine implant, some of the samples were also analysed by transmission electron microscopy (TEM). Fig. 6.13 shows a cross-section TEM micrograph of Batch 1 sample implanted with 185keV, $2.3\times10^{15}cm^{-2}$ fluorine and annealed at 1000°C for 10s, showing a band of defects extending from a depth of 0.34 to 0.7μm (0.9~ 1.8Rp). A comparison with the SIMS profile in Fig. 5.4 in chapter 5 shows that this band of defects corresponds approximately with the deep fluorine peak on the SIMS profile (0.7- 2Rp). There is no evidence of defects shallower than 0.34μm, which corresponds with the depths of the shallow fluorine peak (0 to 0.2μm) and the fluorine shoulder (0.2 to 0.28μm). These defects in the deep fluorine peak consist of dislocation loops with various shapes and sizes. Dislocation loop sizes typically fall in the range 20 to 80 nm.

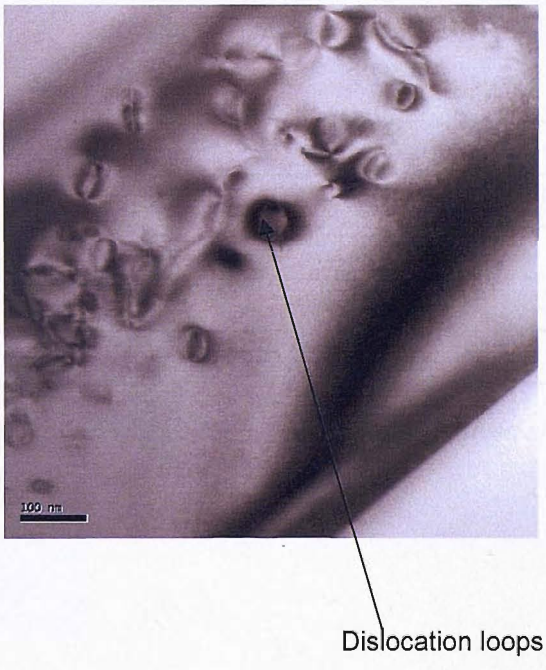

Fig. 6.13. Cross-section TEM micrographs (bright field) of samples implanted with 185 keV, 2.3×10^{15} cm^{-2} F^+ and annealed for 10 s at 1000 °C under inert conditions. The magnification bar is 100 nm.

Figure 6.14 compares cross-section TEM images of Batch 3 samples implanted with fluorine and annealed at 1000°C for 120s under inert anneal (a) and interstitial injection (b). Dislocation loops are still present after 120s, occupying the same depths seen for the short anneal time in Fig. 6.13 (0.34 to 0.7 μm). However, the density of loops appears to be significantly lower in the sample annealed under interstitial injection conditions. Counting the dislocation loops in the cross-section TEM micrographs (Fig. 6.14 inset), the loop density for

interstitial injection is ~ 1.2 x 10^{10} defects/cm^2 and for inert anneal is ~ 2 x 10^{10} defects/cm^2. Therefore, the loop density is lower by a factor of ~ 2 under interstitial injection than inert anneal. To better quantify the dislocation loop densities, plan-view TEM images were taken, as shown in Fig. 6.15 for samples annealed at 1000°C for 120s under inert anneal (a) and interstitial injection (b). From the plan-view TEM images in Fig. 6.15, the defects can be categorised into three types: (i) very small loops, which appear as bright spots, less than 10nm in diameter, (ii) medium sized dislocation loops as shown by red arrows and (iii) big irregular shaped loops as shown by blue arrows in Fig. 6.15. The loop density measured from the plan-view TEM for interstitial injection is ~ 2.7 x 10^9 defects/cm^2 and for inert anneal is ~6.3 x 10^9 defects/cm^2, as summarised in Table 6.1. Here we observed again that the loop density is lower by a factor of ~ 2 under interstitial injection than inert anneal. The sizes of the dislocation loops were also characterised from the plan-view TEM images and are summarised in Table 6.1. The sizes of medium-sized dislocation loop typically fall in the range 20 to 40 nm under inert anneal and 50 to 80 nm under interstitial injection conditions.

Defect type	Density (cm^{-2})		Size (nm)	
	Inert anneal	I-inj	Inert anneal	I-inj
Small	many	few	<10	10-20
Medium	6.3 x 10^9	2.7 x 10^9	20-40	50-80
Irregular	few	few	-	-

Table 6.1. Summary of the types and counts of defects observed under plan-view TEM for inert anneal and interstitial injection.

(a) (b)

Fig. 6.14. Cross-section TEM micrographs (bright field) of samples implanted with 185 keV, 2.3 x 10^{15} cm^{-2} F^+ and annealed for 120 s at 1000 °C under (a) inert conditions and (b) interstitial injection from the surface. The magnification bar is 100 nm in both cases.

(a) (b)

*Fig. 6.15. Plan-view TEM micrographs (weak beam dark field, **B**=[0 0 1], **g** =<400>) of samples implanted with 185 keV, 2.3 x 10^{15} cm^{-2} F^+ and annealed for 120 s at 1000 °C under (a) inert conditions and (b) interstitial injection from the surface. The magnification bar is 100 nm in both cases.*

6.3. Discussion

Fluorine SIMS results in the previous chapter provide strong evidence that the shallow fluorine peak and the shoulder are due to vacancy-fluorine clusters. To better understand the nature of the V-F clusters, a comparison is made between the fluorine SIMS profiles in Fig. 5.6 (a) with the boron diffusion coefficients for boron peak 1 in Fig. 6.6. For the fluorine implanted sample under interstitial injection, the rise of the boron diffusion coefficient for the 45s anneal coincides with the elimination of the shallow fluorine peak. Therefore, suppression of boron diffusion correlates with the presence of the shallow fluorine peak at $\sim 0.3R_p$. These results confirm that the shallow fluorine peak is due to V-F clusters and that these clusters are responsible for boron diffusion suppression. It is expected that the V-F clusters would create an undersaturation of the interstitial concentration in the vicinity of the boron profile located around $0.3R_p$ of the fluorine implant. Since boron diffusion is interstitial-mediated, an undersaturation of the interstitial concentration leads to retarded boron diffusion. The elimination of the shallow fluorine peak can be explained by the annihilation of vacancies in the clusters by recombination with injected interstitials. The correlation between V-F clusters and boron diffusion is also applicable to the samples under inert anneal. In this case, boron diffusion suppression is still observed after 45s anneal due to the presence of fluorine shallow peak and the suppression is no longer seen after 120s anneal with the elimination of the shallow peak.

To further investigate the properties of the V-F clusters, values of instantaneous boron diffusion coefficient are extracted for different time intervals (0-15s, 15-45s and 45-120s) by taking the SIMS profile at the start of each time period as input to the simulation program. The results are shown in Fig. 6.16 and give an indication of the time dependence of the boron diffusion coefficient. For the shallow fluorine peak under interstitial injection conditions (F, I-inj) in Fig. 6.16 (a) shows that the instantaneous boron diffusion coefficient increases to the value of unimplanted samples under interstitial injection (no F, I-inj, dashed line). Therefore, after the elimination of the shallow fluorine peak, the effect of fluorine in suppressing boron diffusion ends and the injected interstitials dominate the boron diffusion. The intermediate value of instantaneous boron diffusion coefficient for the 15-45s time period suggests that the V-F clusters are eliminated after a time nearly half way through this time period.

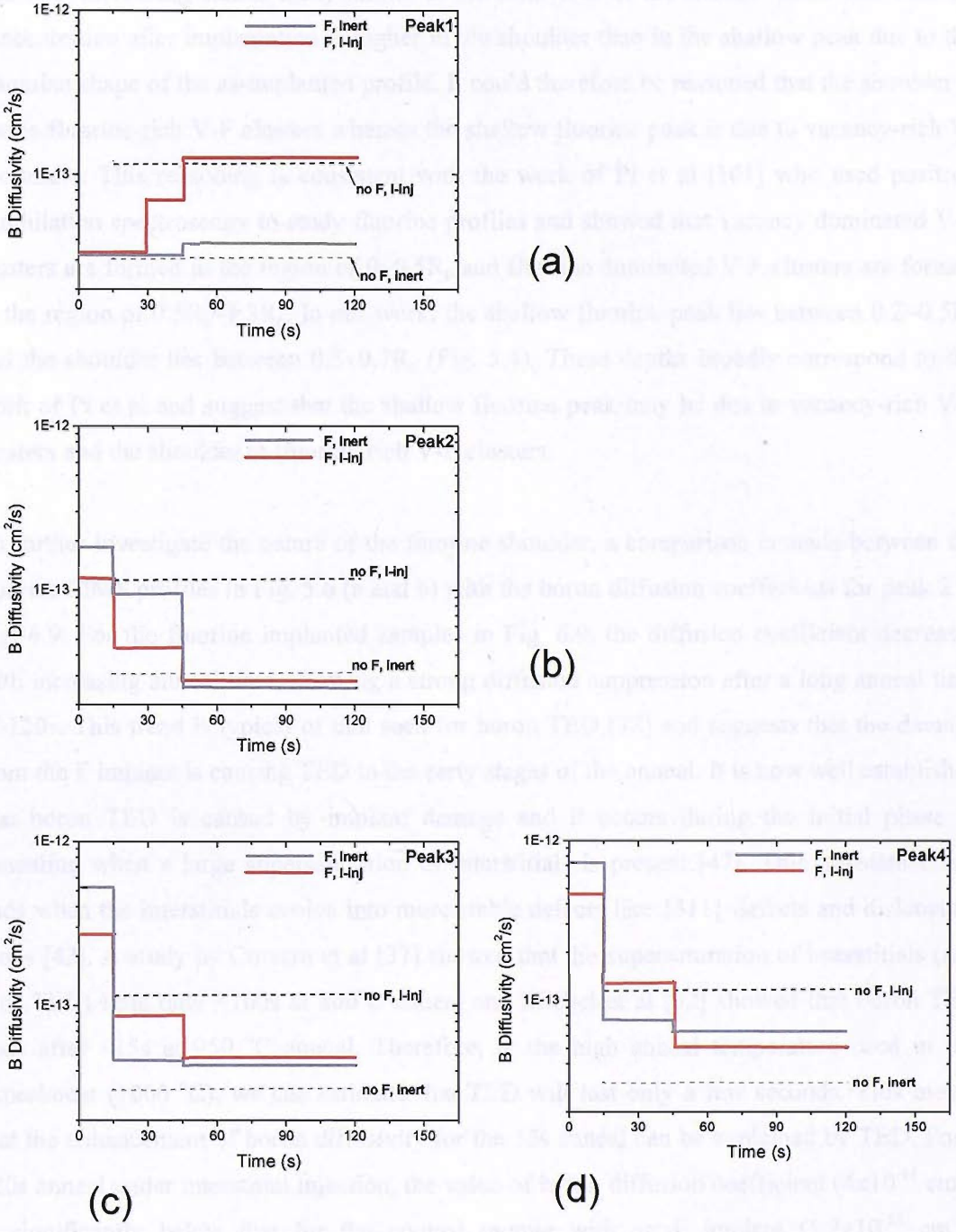

Fig. 6.16. Instantaneous boron diffusion coefficient of boron peaks 1 to 4 as a function of anneal time for fluorine implanted (185 keV, 2.3 x 10^{15} cm^{-2}) and unimplanted samples annealed at 1000 °C under interstitial injection and inert conditions.

We now discuss the nature of the fluorine shoulder. The fluorine SIMS profiles in Fig. 5.6 (a) and (b) suggest that the shoulder may be due to V-F clusters since the shoulder decreases in size with increasing anneal time, similar to the behaviour of the shallow peak. The fluorine concentration after implantation is higher in the shoulder than in the shallow peak due to the Gaussian shape of the as-implanted profile. It could therefore be reasoned that the shoulder is due to fluorine-rich V-F clusters whereas the shallow fluorine peak is due to vacancy-rich V-F clusters. This reasoning is consistent with the work of Pi et al [101] who used positron annihilation spectroscopy to study fluorine profiles and showed that vacancy dominated V-F clusters are formed in the region of $0\sim0.5R_p$ and fluorine dominated V-F clusters are formed in the region of $0.5R_p\sim1.3R_p$. In our work, the shallow fluorine peak lies between $0.2\sim0.5R_p$ and the shoulder lies between $0.5\sim0.7R_p$ (Fig. 5.4). These depths broadly correspond to the work of Pi et al and suggest that the shallow fluorine peak may be due to vacancy-rich V-F clusters and the shoulder to fluorine-rich V-F clusters.

To further investigate the nature of the fluorine shoulder, a comparison is made between the fluorine SIMS profiles in Fig. 5.6 (a and b) with the boron diffusion coefficients for peak 2 in Fig. 6.9. For the fluorine implanted samples in Fig. 6.9, the diffusion coefficient decreases with increasing anneal time, showing a strong diffusion suppression after a long anneal time of 120s. This trend is typical of that seen for boron TED [32] and suggests that the damage from the F implant is causing TED in the early stages of the anneal. It is now well established that boron TED is caused by implant damage and it occurs during the initial phase of annealing when a large supersaturation of interstitials is present [47]. This transient effect ends when the interstitials evolve into more stable defects like {311} defects and dislocation loops [43]. A study by Cowern et al [37] showed that the supersaturation of interstitials (and thus TED) lasts only ~100s at 800°C anneal and Michel et al [32] showed that boron TED ends after ~15s at 950 °C anneal. Therefore, at the high anneal temperature used in our experiment (1000 °C), we can estimate that TED will last only a few seconds. This means that the enhancement of boron diffusivity for the 15s anneal can be explained by TED. For a 120s anneal under interstitial injection, the value of boron diffusion coefficient ($4x10^{-14}$ cm^{-2}) is significantly below that for the control sample with no F implant ($1.2x10^{-13}$ cm^{-2}), suggesting that a suppression of boron diffusion. This result tends to confirm that the fluorine shoulder is due to V-F clusters.

To further investigate the behaviour of the fluorine shoulder, we consider the instantaneous diffusion coefficients for boron peak 2 in Fig. 6.16 (b). For interstitial injection (red line), the results show that the instantaneous boron diffusion coefficient drops to a value slightly below that for no fluorine implant (no F, inert) for the 45-120s time interval. This confirms that

boron diffusion is being suppressed for long anneals and hence further confirms that the fluorine shoulder is due to V-F clusters. For inert anneal, a similar trend is observed and for the 45-120s time interval, the instantaneous boron diffusion coefficient of the fluorine implanted sample (F, inert) is only a factor of 0.8 to that of the inert anneal control sample without a fluorine implant (no F, inert). This suggests that the V-F clusters in the shoulder may be reducing boron thermal diffusion. However, the effect is small and further work is needed to confirm this conclusion.

Figure 6.16 (b) also shows that the instantaneous diffusion coefficient is lower under interstitial injection than inert anneal for both the 0-15s and the 15-45s time intervals. This suggests that boron diffusion is smaller under interstitial injection than inert anneal and confirms the trend seen in Fig. 6.9. This behaviour will be discussed later as part of the discussion of peaks 3 and 4.

We now discuss the diffusion of boron peaks 3 and 4 which are located in the interstitial-rich region of the fluorine damage profile. Fig. 6.12 shows that the average boron diffusion coefficient is lower under interstitial injection than under inert anneal. This is a surprising result, since boron diffusion is mediated by interstitials and hence it would be expected that the boron diffusion would be greater under interstitial injection than inert anneal. To interpret this result, the plan-view TEM micrographs in Fig. 6.15 are considered, which show that dislocation loops are larger and fewer in number under interstitial injection than inert anneal. The evolution of defects (free interstitials transforming to {311} defects and dislocation loops) after ion implantation depends on both anneal temperature and the implanted dose [105]. In our experiment, it seems that the interstitials injected from the surface are accelerating the evolution of the defects. Once formed, dislocation loops of different sizes exchange interstitials in such a way that big loops grow larger at the expense of the smaller loops. This phenomenon is called the Ostwald ripening mechanism [104]. The driving force for this loop growth is a decrease in the formation energy as the loop size increases [43, 44]. The results in Figs. 6.12 and 6.15 suggest that this acceleration of the Ostwald ripening process is responsible for the lower boron diffusion under interstitial injection than inert anneal.

To further investigate this behaviour, we consider the values of instantaneous boron diffusion coefficient in Figs. 6.16 (c) and (d) for peaks 3 and 4 respectively. For boron peak 3, Fig. 6.16 (c) shows that the instantaneous boron diffusion in the 0-15s time interval is higher under inert anneal than interstitial injection. However, after an anneal of 45-120s, the diffusion coefficients have decreased by a factor of ~10 and similar values are obtained for inert anneal and interstitial injection. As discussed for peak 2, this trend is typical of TED and

suggests that damage from the F implant is causing TED in the first 15s of the anneal. The same trend is seen for peak 4 in Fig. 6.16 (d), though larger values of instantaneous boron diffusion coefficient are obtained for all anneal times and injection conditions. The results in Fig. 6.16 indicate that in fluorine implanted silicon, there is less TED under interstitial injection than inert anneal, and the results in Fig. 6.15 suggests that this is due to accelerated Ostwald ripening under interstitial injection. Much research has been done on the thermal evolution of implantation defects formed by amorphising implants [37, 43, 104]. Fig. 6.17 depicts a model for the evolution of EOR defect bands proposed by Cowern et al [104]. It outlines the concept of Ostwald ripening within the EOR defect band and also the out-diffusion of the interstitials towards the surface through a gradient, S_I. If the dislocation loops are a long way from the surface, as is the case in the present work, there is little out-diffusion of interstitials to the surface and the majority of the interstitials are retained in the dislocation loop band. This is known as conservative Ostwald ripening. Alternatively, if the dislocation loops are close to the surface (or the space between dislocation loops is comparable to the distance from the surface), there is a significant flux of interstitials to the surface and this is known as non-conservative Ostwald ripening. The fluorine implant dose in our experiment is below the amorphization dose, but nevertheless a band of dislocation loops is formed and hence it would be expected that the Ostwald ripening process would occur. It is now generally accepted that TED is caused by the interstitials created by implant damage and by interstitials released from {311} defects prior to their evolution into dislocation loops. The accelerated Ostwald ripening seen in this thesis under interstitial injection would be expected to rise to earlier ripening of {311} defects and hence enhanced boron diffusion would be seen over a shorter period of time. This mechanism would explain the smaller values of average boron diffusion coefficient in Fig. 6.12 under interstitial injection than inert anneal. It is also consistent with the lower value of instantaneous boron diffusion coefficient in Fig. 6.16 under interstitial injection than inert anneal for the 0-15s time period.

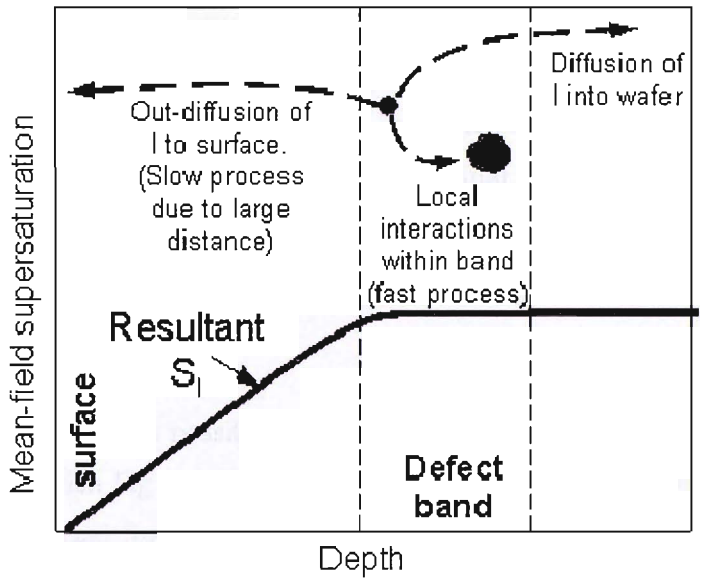

Fig. 6.17. Schematic showing the different paths of interstitials in a non-conservative Ostwald ripening, after Cowern et al [104].

Another interesting trend is seen in Fig. 6.16 (c) for an anneal of 45-120s under interstitial injection in that the instantaneous boron diffusion coefficient in the F-implanted sample ($4x10^{-14}$ cm^{-2}) is significantly lower than that in the unimplanted control sample ($1.2x10^{-13}$ cm^{-2}). The suppression of B transient enhanced diffusion has been attributed to the retention of interstitials in the dislocation loops by El Mubarek et al [25]. The results in Fig. 6.16 (c) and (d) suggest that a similar mechanism is occurring here. This behaviour could again be related to the accelerated ripening of the dislocation loops under interstitial injection in the fluorine implanted samples. If the majority of interstitials were tied up in the dislocation loops so that the interstitial flux in the dislocation band was small, then the boron diffusion in the fluorine implanted samples might well be lower than that in the unimplanted control samples, where there would be considerable flux of interstitials from the surface. Another factor contributing to the lower instantaneous boron diffusion coefficient in the fluorine implanted samples could be the capture of interstitials injected form the surface at dislocation loops as dislocation loops are well known to be a good sink for interstitials [102,103,106,107]. Park et al [103] also reported a ~50% suppression of boron oxidation enhanced diffusion (OED) by dislocation loops during oxidizing anneal at 900°C for 30min (equivalent to the conditions of 1000°C for ~120s in our experiment). In their experiment, a Si^+ implant (near surface) and damage anneal were done first to form loops and then an oxidizing anneal was used to diffuse the boron marker layers located at a deeper substrate. The reduction of boron OED was attributed to the blockage of interstitials by the dislocation loops. In our experiment, loops are formed at the same time as the boron anneal, and both loops and boron marker are

located in the same region. However, the loop evolution behaviour and its effect in reducing boron enhanced diffusion are similar. Under inert anneal, the results in Figs. 6.16 (c) and (d) show slightly more boron diffusion in fluorine implanted samples than in the unimplanted control samples. As there is expected to be little interstitial injection from the surface during inert anneal, this enhanced diffusion in the fluorine implanted samples presumably gives a measure of the interstitial flux in the dislocation band during the conservative Ostwald ripening process.

Finally, we will look at some possible explanations for the annihilation of the V-F clusters under inert anneal which Fig. 5.6 (b) shows occurs after 120s anneal. Firstly, there may be some interstitials injected from the surface even under inert anneal. In our experiment, the inert injection condition is achieved by capping the silicon with both a LTO and Si_3N_4 layers. Karunaratne et al [89] and Bonar et al [86], who have used a similar procedure for inert anneal, have reported values of boron diffusion coefficient of 9.9 x 10^{-15} and 1.89 x 10^{-14} cm^2/s respectively, which are very similar to the value of 1.53 x 10^{-14} cm^2/s reported by Fair for intrinsic diffusion of boron [99]. However, we have shown that the boron diffusion coefficient under inert anneal in our experiment (Fig. 6.6 for example) is 3.1 x 10^{-14} cm^2/s, which is a factor of ~2 larger than the Fair value. From these arguments, we cannot completely discount the possibility of some interstitials being injected from the surface under inert anneal. Another possibility is that thermally generated interstitials could be annihilating the V-F clusters. The thermodynamics of native point defects state that for any temperature other than 0 K, finite concentrations of point defects will exist in thermal equilibrium [38]. Bracht et al [90] have experimentally determined the thermal equilibrium concentration of self-interstitials and vacancies at 1000°C to be ~ 1x 10^{12} cm^{-3} and ~ 1x 10^{15} cm^{-3} respectively. These thermally generated point defects are several orders of magnitude lower than the fluorine concentration (~7 x 10^{18} cm^{-3}) after a 15s inert anneal, so it is unlikely that thermally generated self-interstitials play a dominant role in the V-F cluster annihilation. A third possibility is that there is some flow of interstitials towards the surface even in a conservative Ostwald ripening process. The interstitials could then annihilate the V-F clusters in the shallow peak as observed in Fig. 5.6(b). Further work is needed to distinguish between these possibilities.

6.4. Conclusions

In summary, a study has been made of the effect of point defect injection on ion implanted fluorine profiles and boron marker layers located at different depths during anneal at 1000 °C. By correlating the boron diffusion coefficients with fluorine SIMS profiles and TEM images, we have examined the nature of the different fluorine peaks and the mechanisms responsible for boron diffusion suppression.

SIMS analysis has shown fluorine peaks seen at depths of $0.3R_p$ and R_p, and a shoulder between $0.5\sim0.7R_p$ after annealing of a 185keV, 2.3 $x10^{15}$ cm^{-2} F^+ implant, as shown in Chapter 5. The presence of the shallow fluorine peak at $0.3R_p$ correlates with the suppression of boron diffusion in a boron marker located at the same depth. Therefore, this result provides strong evidence that the shallow fluorine peak is due to vacancy-fluorine clusters and that these clusters are responsible for the suppression of boron diffusion. The elimination of the shallow fluorine peak has been explained by the annihilation of vacancies in the clusters by recombination with injected interstitials.

SIMS profiles have shown that the fluorine shoulder decreases in size with increasing anneal times, similar to the behaviour of the shallow peak. It is proposed that the F shoulder is due to fluorine-rich VF clusters, whereas the shallow F peak is due to vacancy-rich VF clusters. The boron diffusion coefficient of a boron marker layer located in the shoulder region decreases with increasing anneal time, which has been explained by TED. Under interstitial injection, the average boron diffusion coefficient at long anneal times is 3 times lower in fluorine implanted samples than in unimplanted control samples. This result has been explained by the suppression of boron diffusion by the fluorine-rich VF clusters.

For boron peaks located in the interstitial-rich region of the fluorine damage profile, the average boron diffusion coefficient decreases with increasing anneal time and shows a lower value under interstitial injection than under inert anneal. Plan-view TEM micrographs show that the dislocation loops are larger and fewer under interstitial injection than inert anneal. It is therefore proposed that the injected interstitials are accelerating evolution of interstitial defects into dislocation loops, that is accelerating the Ostwald ripening process.

Chapter 7

Effect of device process flow on Vacancy-Fluorine Clusters

7.1. Introduction

In Chapters 5 and 6, we investigated the behaviour of fluorine using a point defect injection technique. By correlating F SIMS profiles with boron diffusion profiles, we provided strong evidence that the boron diffusion suppression was due to V-F clusters. Our studies were done at only one fluorine energy (185 keV) and one anneal temperature (1000°C). In this chapter, we pursue a detailed, systematic study of fluorine behaviour in silicon when various experimental conditions are varied, such as anneal time and temperature, implant energy and implantation damage. In this way, we aim to get a better understanding of fluorine behaviour under a wide range of conditions which are of interest in device fabrication.

Firstly, we will study fluorine behaviour in silicon at temperatures in the range of 820 to 1050°C for times in the range of 45 s to 1.5 hrs, so that we can verify the thermal anneal conditions at which the different F peaks are formed and eliminated. Secondly, we will investigate the fluorine behaviour when damage from co-implanted B^+ or As^+ is present. In MOSFET device fabrication, various dose ranges are used in doping implants: for example, a low dose ~ 10^{13} cm^{-2} implant is used for the halo and a high dose ~ 10^{15} cm^{-2} implant is used for the extension and highly-doped drain (HDD) [39]. Hence it is vitally important to investigate how implantation damage from these implants affects the fluorine behaviour, especially the V-F clusters. Lastly, we will investigate the effect of decreasing F implant energy on the fluorine behaviour because lower implantation energies are being increasingly used due to the device scaling in modern transistors. The results on the effect of anneal temperature and time are presented in section 7.3, the effect of implantation damage in section 7.4 and the effect of F implantation energy in section 7.5. Finally, section 7.6 presents the implementation of fluorine implantation in a production silicon bipolar technology at STMicroelectronics, Sicily, Italy. We will demonstrate that the fluorine implant dramatically suppresses boron diffusion in the base and leads to a value of f_T as high as 110 GHz in an appropriately optimised device.

7.2. Experimental procedure

Czochralski-grown <100>-oriented, p-type wafers with a resistivity of 17-33 Ω–cm were used. Each wafer from Batch 4 was given one of the following four types of implants: 5 keV, 7×10^{12} cm^{-2} B^+, 5 keV, 2×10^{15} cm^{-2} B^+, 10 keV, 1×10^{13} cm^{-2} As^+ or 5×10^{13} cm^{-2} As^+. Each wafer was then implanted with either 100 keV, 1×10^{15} cm^{-2} F^+ or 185 keV 2.3×10^{15} cm^{-2} F^+ (Batch 4 in Table 7.1). A second batch of silicon wafers, Batch 5, was also implanted with B implants under similar conditions to the Batch 4. It was then divided into two sections for 50 and 185 keV F implants with doses of 1×10^{15} and 2.3×10^{15} cm^{-2} respectively. Fig. 7.1 shows the as-implanted fluorine profiles with peak concentrations of ~ 1×10^{20} cm^{-3} for the 50 and 185keV F implants and ~ 5×10^{19} cm^{-3} for the 100 keV F implant. The wafers were then cut into 1 cm x 1 cm pieces and a rapid thermal anneal was performed for a time in the range 10 s to 1.5 hrs and at a temperature between 820 and 1050 °C in a nitrogen ambient. The rapid thermal anneal was either performed on a Process Product Corporation (PPC) rapid thermal annealer at the University of Surrey for Batch 4 samples or on a Heatpulse-610 rapid thermal annealer at Innos Ltd for Batch 5 samples. Details of the samples are shown in Table 7.1. The boron and fluorine atomic profiles were measured by Secondary Ion Mass Spectroscopy (SIMS) using 10keV, 0.8 μA O_2^+ primary ion bombardment.

Simulation of the vacancy and interstitial distributions generated after implant was done using a Monte Carlo simulation program called TRIM (the Transport of Ions in Matter) [108]. It uses a binary collision model of ion-solid interactions to calculate the range and damage distribution. In this program, it is assumed that the target as an amorphous layer and there is no dynamic annealing or damage evolution taking place. Appendix II shows the steps taken to convert TRIM output data (count/ion/Angstrom) to the damage distribution graph (count/cm^3).

	F energy (keV)	**Co-implant**	**Anneal conditions**	**RTA equipment**
Batch 4	100, 185	B^+ (or) As^+	820- 1050 °C 45s- 1.5hrs	PPC
Batch 5	50, 185	B^+	900 & 1000 °C 10s- 6min	Heatpulse-610

Table 7.1. Details of the samples, anneal conditions and RTA equipment used in this study

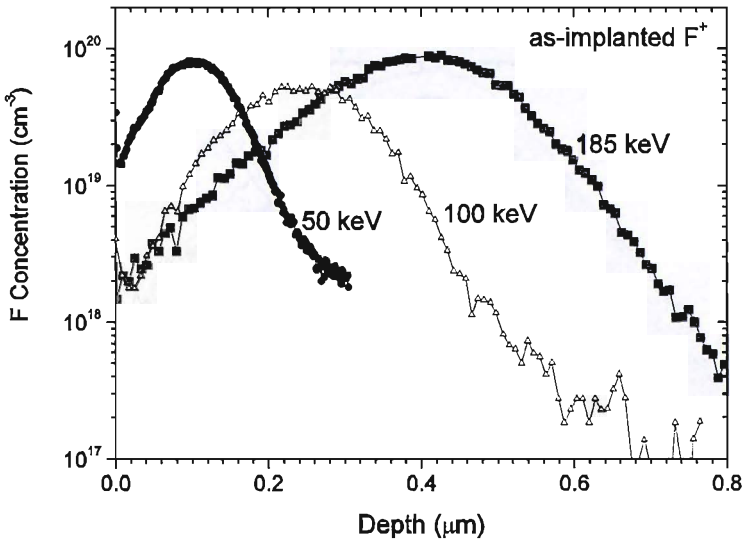

Fig. 7.1. As-implanted Fluorine SIMS profiles for samples implanted with 50 keV, $1\times10^{15}cm^{-2}$, 100 keV, $1\times10^{15}cm^{-2}$ and 185 keV, $2.3\times10^{15}cm^{-2}$ F^+.

7.3. Effect of anneal temperature and time

7.3.1. Results

Figure 7.2 shows F SIMS profiles of Batch 4 samples given a 185keV, 2.3x 10^{15} cm^{-2} F^+ implant and a 45s anneal at a temperature of 820, 900, 1000 or 1050 °C. At the two lowest temperatures (820 and 900 °C), we can see that a shallow fluorine peak is not clearly delineated, whereas for the two highest temperatures (1000 and 1050 °C), a significant shallow peak is observed. Looking at the profiles at depths between 0 and 0.27μm in more detail after a 820 °C anneal, the fluorine concentration is ~1 x10^{19} cm^{-3} at depths between 0.15 and 0.32 μm, forming a small plateau. After a 900 °C anneal, the fluorine concentration is lower (~ 7 x10^{18} cm^{-3}) and the plateau extends further towards the surface to a distance of ~0.05 μm from the surface. In contrast, after a 1000 °C anneal, a distinct shallow peak is formed centred at a depth of 0.17 μm (0.4Rp) with a dip in fluorine concentration at a depth of 0.27 μm and a peak concentration of ~5 x10^{18} cm^{-3}. Furthermore, the peak does not extend as far towards the surface as was seen for the plateau after a 900 °C anneal. After a 1050 °C anneal, a clear shallow peak is again seen at a depth of approximately 0.17 μm (0.4Rp), but the peak concentration is lower (~4 x10^{18} cm^{-3}). Furthermore, the peak does not extend as far towards the surface as was seen for the 1000 °C anneal and the dip in fluorine concentration at a depth of 0.27 μm is more pronounced.

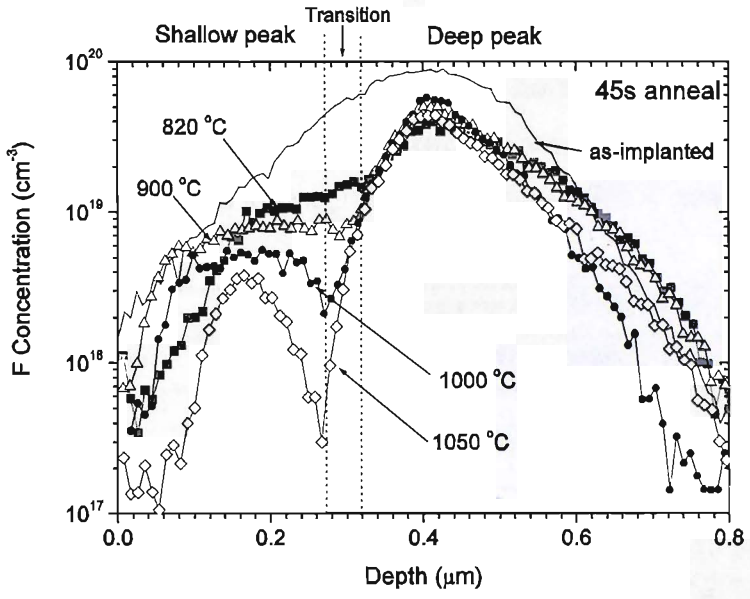

Fig. 7.2. Fluorine SIMS profiles for samples implanted with 185 keV, 2.3×10^{15}cm^{-2} F^{+} and annealed for 45s at 820, 900, 1000 or 1050 °C in nitrogen

Figure 7.2 shows a deep fluorine peak at a depth of 0.42 μm, which is slightly beyond the range of the fluorine implant (0.4 μm). The deep peak is more stable than the shallow peak, although some fluorine loss is observed. In the previous chapter, the fluorine profiles showed a distinctive shoulder between the shallow peak and the deep peak (at depths between 0.2 to 0.28 μm in Fig. 5.4 for example). However, in this chapter, a clear shoulder is not discernable. Nevertheless, a transition region can be seen in Fig. 7.2 at depths between 0.27 and 0.32 μm. The limits of this transition region were defined by the position of the dip in fluorine concentration after anneal at 1000 °C and the intersection of the plateau region with the deep fluorine peak after anneal at 820 °C. The position of the transition region in Fig. 7.2 is slightly deeper than the shoulder observed in Fig. 5.4.

Table 7.2 summarises the fluorine dose remaining in the different F peaks after anneal under different anneal conditions. The shallow F peak was defined as extending from 0 to 0.27 μm (0- 0.7 Rp), the transition from 0.27 to 0.32 μm (0.7 -0.8 Rp) and the deep peak from 0.32 to 0.8 μm (0.8 -2Rp). We observe that the total dose remaining is only 47% even for the lowest anneal temperature and it further reduces to 34% for the highest anneal temperature. In the shallow peak and the transition region, the general trend is that the fluorine dose decreases as the anneal temperature increases. The fluorine doses in the shallow peak and the transition region after implant are small (16 and 13%) and further reduce to only 2% after annealing at the highest temperature. The SIMS detection limit for fluorine is around 1×10^{17} cm^{-3} which

corresponds to a F dose of 8×10^{12} cm^{-2} (±0.3%). Therefore, it should be noted that 2% dose in the shallow fluorine peak and the transition region after a 1050 °C anneal is still significant. For the deep fluorine peak, the fluorine concentration lies between 7×10^{14} and 9×10^{14} cm^{-2} (30 and 39%) for all anneal temperatures. The F concentration in the deep peak is highest (9×10^{14} cm^{-2}) after a 900 °C anneal and lowest (7×10^{14} cm^{-2}) after a 1050 °C anneal.

	F dose remaining in different peaks (cm^{-2})				
Anneal conditions	Total dose	Plateau	Shallow peak	Transition	Deep peak
		(0-0.27 μm)		(0.27 -0.32 μm)	(0.32 - 0.8 μm)
As-implanted	2.3 $x10^{15}$ (100%)	3.6 $x10^{14}$ (16%)		3.0 $x10^{14}$ (13%)	1.63 $x10^{15}$ (71%)
820 °C 45s	1.08 $x10^{15}$ (47%)	1.5 $x10^{14}$ (7%)	-	1.0 $x10^{14}$ (4%)	8.3 $x10^{14}$ (36%)
900 °C 45s	1.12 $x10^{15}$ (49%)	1.6 $x10^{14}$ (7%)	-	6 $x10^{13}$ (3%)	9 $x10^{14}$ (39%)
1000 °C 45s	9.5 $x10^{14}$ (41%)	-	1 $x10^{14}$ (4%)	4 $x10^{13}$ (2%)	8.2 $x10^{14}$ (36%)
1050 °C 45s	7.8 $x10^{14}$ (34%)	-	4 $x10^{13}$ (2%)	4 $x10^{13}$ (2%)	7.0 $x10^{14}$ (30%)

Table 7.2. Summary of F dose remaining in the different F peaks for a 185keV F^+ implant annealed for 45s at a temperature between 820 and 1050 °C

Next, we investigate the fluorine profiles after anneals for various times at each anneal temperature. Figure 7.3 shows F SIMS profiles of Batch 4 samples given a 185 keV, $2.3\times10^{15}cm^{-2}$ F^+ implant and an inert anneal at 820 °C for times between 45 s to 1.5 hours. After a 45 s anneal, a small plateau is formed at depths between 0.15 and 0.27 μm with a fluorine concentration of ~1 $x10^{19}$ cm^{-3}. The peak fluorine concentration at the plateau slightly decreases to ~9 $x10^{18}$ cm^{-3} after a 2 min anneal and the plateau extends further towards the surface to a distance of ~0.05 μm from the surface. The same trend is observed for a 30 min anneal, with the fluorine concentration reducing to ~ 6 x 10^{18} cm^{-3} and the plateau reaching to a distance of ~0.02 μm from the surface. The plateau formed after a 1.5 hrs anneal is almost identical to that after a 30 min anneal, indicating that no fluorine movement occurs in the plateau during the last 60 min of the 1.5 hr anneal. A transition region, as defined in Fig. 7.2, is shown for comparison. As for the deep peak, the peak concentration decreases and the fluorine profile broadens after the 45 s anneal. For the longer anneal times, the descending slope at the substrate side of the profile moves towards the surface and the peak concentration of the deep peak increases as the anneal time increases. This is a surprising result, as it represents a reversal of the trend seen in the first 45 s of the anneal.

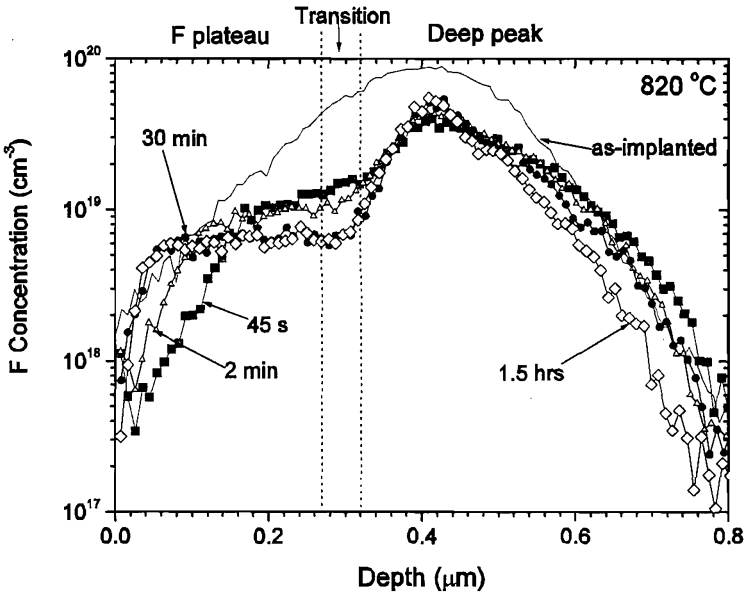

Fig. 7.3. Fluorine SIMS profiles for samples implanted with 185 keV, $2.3x10^{15}cm^{-2}$ F^+ and annealed for 45s- 1.5hrs at 820 °C in nitrogen

Table 7.3 shows the fluorine dose remaining in the different fluorine peaks after anneal at 820°C for the different anneal times presented in Fig. 7.3. The fluorine plateau was defined as extending from 0 to 0.27 μm (0- 0.7 Rp), the transition region from 0.27 to 0.32 μm (0.7 to 0.8 Rp) and the deep peak from 0.32 to 0.8 μm (0.8 -2Rp). The majority of dose loss occurs in the first 45s anneal, down to 48% and there is a further dose loss of only 7% in the subsequent anneals. The general trend in the plateau and the transition region is that the fluorine dose decreases slightly as the anneal time increases. For the deep peak, the F dose is 8.3 $x10^{14}$ cm^{-2} after 45s, increases slightly to 8.7 $x10^{14}$ cm^{-2} after 2 min and then decreases to 7.0 $x10^{14}$ cm^{-2} after 1.5 hrs. Although the dose loss in both the plateau and the deep peak is rather small, distinctive changes in the SIMS profiles are seen in Fig.7.3.

	F dose remaining in different peaks (cm^{-2})			
Anneal conditions	Total dose	F plateau (0 - 0.27 μm)	Transition (0.27- 0.32 μm)	Deep peak (0.32 - 0.8 μm)
As-implanted	2.3 $x10^{15}$ (100%)	3.6 $x10^{14}$ (16%)	3.0 $x10^{14}$ (13%)	1.63 $x10^{15}$ (71%)
820 °C 45s	1.1 x 10^{15} (48%)	1.5 $x10^{14}$ (7%)	1.0 $x10^{14}$ (4%)	8.3 $x10^{14}$ (36%)
820 °C 2 min	1.1 $x10^{15}$ (48%)	1.6 $x10^{14}$ (7%)	8.0 $x10^{13}$ (3%)	8.7 $x10^{14}$ (38%)
820 °C 30 min	1.0 $x10^{15}$ (44%)	1.5 $x10^{14}$ (6%)	5.0 $x10^{13}$ (2%)	8.2 $x10^{14}$ (36%)
820 °C 1.5 hrs	9.4 $x10^{14}$ (41%)	1.4 $x10^{14}$ (6%)	5.0 $x10^{13}$ (2%)	7.0 $x10^{14}$ (33%)

Table 7.3. Summary of F dose remaining in the different F peaks in samples implanted with 185 keV F^+ and annealed at 820 °C for 45 s to 1.5 hrs.

Figure 7.4 shows the fluorine SIMS profiles of Batch 4 samples given 185keV, 2.3×10^{15} cm^{-2} F^+ implant and an inert anneal at 900 °C for 45 s or 2 min. At depths between 0 and 0.27 μm, both annealed fluorine profiles exhibit similar plateaus with a concentration of $7x10^{18}$ cm^{-3}. For the deep peak, the descending slope at the substrate side of the profile moves towards the surface as the anneal time increases, as was observed for the 820 °C anneal in Fig. 7.3.

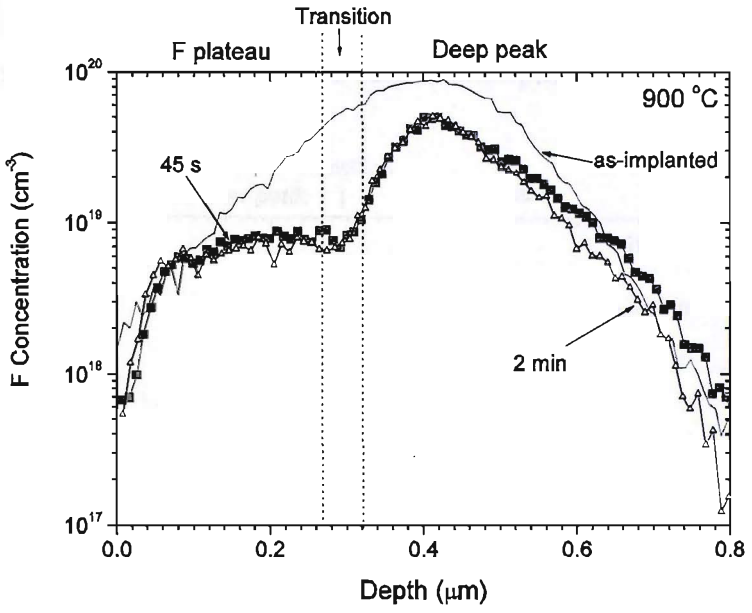

Fig. 7.4. Fluorine SIMS profiles for samples implanted with 185 keV, $2.3\times10^{15}cm^{-2}$ F^+ and annealed for 45s- 2min at 900 °C in nitrogen

Table 7.4 shows the fluorine dose remaining in the different F peaks after anneal at 900°C for the different anneal times presented in Fig. 7.4. The doses in the fluorine plateau, transition region and deep peak decrease slightly as the anneal time increases.

	F dose remaining in different peaks (cm^{-2})			
Anneal conditions	Total dose	F plateau (0 - 0.27 μm)	Transition (0.27-0.32μm)	Deep peak (0.32 - 0.8 μm)
As-implanted	$2.3\ x10^{15}$ (100%)	$3.6\ x10^{14}$ (16%)	$3.0\ x10^{14}$ (13%)	$1.63\ x10^{15}$ (71%)
900 °C 45s	$1.12\ x10^{15}$ (49%)	$1.6\ x10^{14}$ (7%)	$6\ x10^{13}$ (2.6%)	$9.0\ x10^{14}$ (39%)
900 °C 2 min	$1.05\ x10^{15}$ (46%)	$1.5\ x10^{14}$ (6.7%)	$5\ x10^{13}$ (2.3%)	$8.5\ x10^{14}$ (37%)

Table 7.4. Summary of F dose remaining in the different F peaks in samples implanted with 185 keV F^+ and annealed at 900 °C for 45 s to 2 min.

Figure 7.5 shows the fluorine SIMS profiles of Batch 4 samples given 185keV, 2.3×10^{15} cm^{-2} F^+ implant and an inert anneal at 1050°C for 45 s or 2 min and Table 7.5 shows the

corresponding fluorine dose remaining in the different F peaks. In Fig. 7.5, a distinctive shallow peak is observed after a 45 s anneal at a depth of 0.17 μm and is almost completely eliminated after a 2 min anneal. The shallow fluorine peak has a peak concentration of ~$4x10^{18}$ cm^{-3} after a 45s anneal and ~4×10^{17} cm^{-3} after a 2 min anneal. The dose loss in the shallow peak between 45 s to 2 min anneal is 1.8% as shown in Table 7.5. The fluorine dose in the deep peak decreases slightly from 7.0 $x10^{14}$ cm^{-2} after a 45 s anneal to 6.2 $x10^{14}$ cm^{-2} after a 2 min anneal (3%). Given the initial dose at each region, a significant decrease is seen in the shallow F peak at 1050 °C, but the deep fluorine peak is relatively stable.

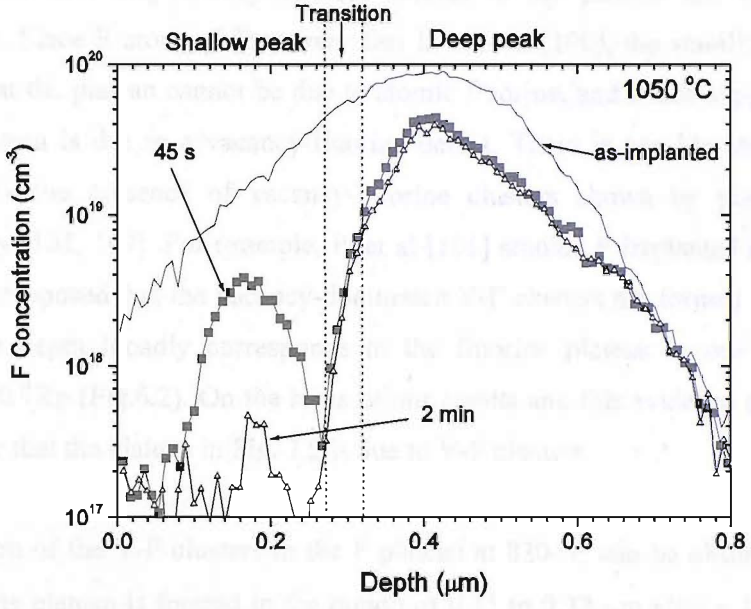

Fig. 7.5. Fluorine SIMS profiles for samples implanted with 185 keV, $2.3x10^{15}cm^{-2}$ F^+ and annealed for 45s- 2min at 1050 °C in nitrogen

	F dose remaining in different peaks (cm^{-2})			
Anneal conditions	Total dose	Shallow peak (0-0.27 μm)	Transition (0.27 -0.32 μm)	Deep peak (0.32 - 0.8 μm)
As-implanted	2.3 $x10^{15}$ (100%)	3.6 $x10^{14}$ (15%)	3.0 $x10^{14}$ (13%)	1.6 $x10^{15}$ (71%)
1050 °C 45s	7.8 $x10^{14}$ (34%)	4 $x10^{13}$ (2%)	4 $x10^{13}$ (2%)	7.0 $x10^{14}$ (30%)
1050 °C 2min	6.5 $x10^{14}$ (28%)	5 $x10^{12}$ (0.2%)	2 $x10^{13}$ (0.8%)	6.2 $x10^{14}$ (27%)

Table 7.5. Summary of F dose remaining in the different F peaks in samples implanted with 185 keV F^+ and annealed at 1050 °C for 45 s to 2 min.

7.3.2. Discussion

As shown in Fig. 7.2, fluorine plateaus are formed after annealing at 820 and 900 °C at depths between 0 to ~0.27 μm, in a similar region where the shallow F peak is seen for higher anneal temperatures (1000 and 1050 °C). In the previous chapter, we have presented strong evidence that the shallow F peak is due to vacancy-fluorine (V-F) clusters. Therefore, it is very likely that the F plateau is also due to a vacancy-fluorine defect and may in fact be due to V-F clusters. Referring to Table 7.3, the F dose in the plateau decreases only slightly from 11% to 8% as the anneal time at 820 °C increases from 45s to 30 min and remains constant to 1.5 hrs. This indicates that the vacancy-fluorine defects in the plateau are very stable at this temperature. Since F atoms diffuse very fast in silicon [100], the stability of the F plateau indicates that the plateau cannot be due to atomic fluorine, and hence supports the argument that the plateau is due to a vacancy-fluorine defect. There is considerable evidence in the literature for the presence of vacancy-fluorine clusters shown by positron annihilation spectroscopy [101, 109]. For example, Pi et al [101] studied F implanted silicon annealed at 700 °C and proposed that the vacancy-dominated V-F clusters are formed in the region of 0-0.5Rp. This depth broadly corresponds to the fluorine plateau in our work, which lies between 0- 0.7Rp (Fig.6.2). On the basis of our results and this evidence from the literature, we conclude that the plateau in Fig. 7.2 is due to V-F clusters.

The evolution of the V-F clusters in the F plateau at 820 °C can be observed in Fig. 7.3. A small fluorine plateau is formed in the region of 0.15 to 0.32 μm after a 45 s anneal. As the anneal time increases, the fluorine plateau moves towards the surface while its concentration decreases. Once a flat plateau is formed after a 30 min anneal, it remains the same for anneal times up to 1.5 hrs. The movement of the F plateau might be explained by diffusion which occurs in the presence of a concentration gradient. The F concentration gradient becomes small (except very close to the surface) after a 30 min anneal as shown, which is consistent with the stable plateau for anneal times larger than 30 min. Fig. 7.4 shows that a flat plateau is already observed after a 45 s anneal at 900 °C and it remains stable till a 2 min anneal. Therefore, the 900°C profiles show a similar behaviour as the 820 °C profiles, though the evolution of the F plateau is more advanced at 900 °C due to the higher anneal temperature.

The diffusivity of the V-F clusters in the F plateau can be estimated from Fig. 7.3. For example, at a concentration of 1 x10^{18} cm^{-3}, F diffuses a distance of ~ 34 nm in 75s (from 45s to 2 min) and another ~ 34 nm in 28 min (from 2 min to 30 min). Using the formula $x^2 = Dt$, where 'x' is the diffusion distance, 't' the anneal time and 'D' the diffusivity, gives values of diffusivity of 8 x 10^{-14} cm^2/s and 13 x 10^{-14} cm^2/s at 820 °C. It should be noted that this

formula comes from $x = 2\sqrt{Dt}$, which is an approximate measure of how far the dopant has diffused for a Gaussian profile and is often termed the diffusion length [39]. There is no reported value in the literature for the diffusivity of V-F clusters. However, we can make an indirect comparison with the diffusion of F in the vacancy rich region in ref. [101], where it is reported that F in the vacancy-rich region takes ~90 hrs to diffuse a distance of 0.9 μm from the region around Rp to the silicon surface at 700 °C. Using the same formula of $x^2 = Dt$ gives a diffusivity of ~ 2.5 x 10^{-14} cm^2/s. This value is lower than the value of 8-13 x 10^{-14} cm^2/s at 820 °C which would be expected as the anneal temperature is lower. On the other hand, the diffusivity of free vacancies reported in the literature is ~ 1 x 10^{-10} cm^2/s at 800 °C [90]. Therefore, it can be seen that the diffusivity of V-F clusters at 820 °C is three orders of magnitude lower than that of free vacancies at 800 °C which is consistent with the slowly changing F plateau observed in Fig. 7.3.

Next, we investigate the evolution of the shallow F peak which is formed at higher anneal temperatures of 1000 and 1050 °C (Fig. 7.2). On going from a 900 °C anneal to a 1000 °C, the F dose loss is significant in two places: at the surface and at the interface between the shallow peak and the transition region, which is indicated by a dip at ~0.27 μm. Similarly, further F dose loss is observed at a similar location on going from a 1000 °C anneal to a 1050 °C anneal. The annealing of V-F clusters at the surface could be explained by surface recombination [38] and that at the transition interface by the close proximity to the interstitial-rich region at Rp. Experiments on the rapid thermal annealing of Ge-preamorphised layers [48] have shown evidence of interstitials being released from end of range dislocation loops for thermal annealing times as short as 1s at 900°C. The recombination of interstitials with vacancies in the V-F clusters might be expected to release fluorine, which could then quickly diffuse to the surface.

The time evolution of the deep peak (0.32 -0.8 μm or Rp -2Rp) at 820 °C is discussed next. Fig. 7.3 unambiguously shows transport of fluorine from the tails of the fluorine profile to the peak as the anneal time is increased from 45s to 1.5hrs. This behaviour is surprising and merits some speculation on possible causes. The behaviour in Fig. 7.3 suggests an uphill diffusion mechanism and implies a flux of point defects from the fluorine profile tail to the peak. One possible cause of such a point defect flux would be the evolution of interstitials clusters into {113} defects and small dislocation loops [110] and the subsequent Ostwald ripening of the loops. Dislocation loops would be expected to form around the range of the fluorine implant, which could then provide the interstitial flux that might explain the uphill

fluorine diffusion. Detailed TEM experiments are needed to further investigate this possibility.

7.4. Effect of implantation damage on F profiles

7.4.1. Results

Figure 7.6 shows F SIMS profiles of Batch 5 samples implanted with or without 5 keV, 7×10^{12} cm^{-2} B^+, followed by 185 keV, 2.3×10^{15} cm^{-2} F^+ and then annealed for 30 s at 1000°C. The boron profile after anneal is also shown for reference. Both F SIMS profiles are very similar, exhibiting typical fluorine peaks: a shallow peak at a depth of 0.13 μm, a deep F peak at 0.42 μm and a shoulder between 0.2 to 0.28 μm. The B SIMS profile lies between the surface and a depth of ~0.1 μm and the boron peak concentration is ~8×10^{17} cm^{-3} at a depth of 0.02 μm. The similar fluorine profiles with and without a B implant indicates that the damage from this low dose B implant has little effect on the shallow F peak.

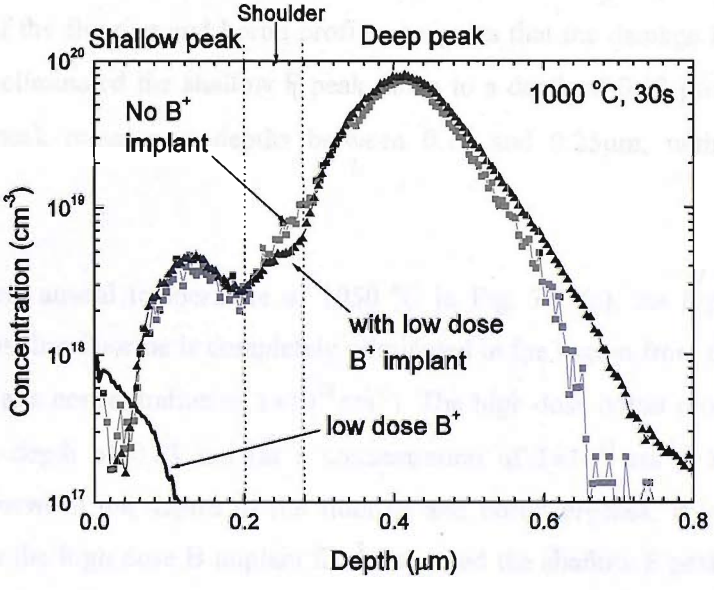

Fig. 7.6. Fluorine SIMS profiles of 185 keV, 2.3×10^{15}cm^{-2} F^+ implanted samples after a 30s anneal at 1000 °C with and without a prior 5 keV B^+ implant at a dose of 7×10^{12}cm^{-2}. The boron annealed profile is also shown for reference.

Figure 7.7 shows F SIMS profiles of Batch 4 samples implanted with 5 keV, 2×10^{15} cm^{-2} B^+ followed by 185 keV, 2.3×10^{15} cm^{-2} F^+, and then annealed for 45 s at 820, 1000 or 1050 °C. Results for the 5 keV, 7×10^{12} cm^{-2} B^+ implant are also shown for reference. After a 820 °C anneal in Fig. 7.7 (a), the low dose B implanted sample shows a fluorine profile with a small plateau at depths between 0.15 and 0.3 μm with a fluorine concentration of ~1 $\times10^{19}$ cm^{-3}.

The high dose B implanted sample shows that there is little fluorine present at depths between ~0.04 and 0.11 μm (at a concentration of 1×10^{18} cm^{-3}). The high dose boron implant extends from the surface to a depth of 0.13 μm (at a concentration of 1×10^{18} cm^{-3}). The correlation between the depths of the boron and fluorine implant suggests that the damage from the high dose B implant eliminates the F plateau in this region. Interestingly, the SIMS profile for the high dose B implanted sample shows the presence of F down to a depth of 0.03μm with a concentration of ~2×10^{18} cm^{-3}, indicating that the damage from the B implant has not eliminated the fluorine at these depths. As for the deep F peak, the SIMS profiles are almost identical in both F samples. Therefore, damage from the high dose B implant near the surface does not have much effect on the deep F peak.

In the high dose B implanted sample annealed at 1000 °C in Fig. 7.7 (b), little fluorine is present in the region from the surface to a depth of 0.18μm (at a concentration of 1×10^{18} cm^{-3}), a region where the high dose B profile is present. The high dose boron profile extends from the surface to a depth of 0.16 μm (at a concentration of 1×10^{18} cm^{-3}). The correlation between the depths of the fluorine and boron profiles suggests that the damage from the high dose B implant has eliminated the shallow F peak down to a depth of 0.18 μm. A small part of the shallow F peak remains at depths between 0.15 and 0.25μm, with a concentration of ~$3\times10^{18}$$cm^{-3}$.

At the highest anneal temperature of 1050 °C in Fig. 7.7 (c), the high dose B implanted sample shows that fluorine is completely eliminated in the region from the surface to a depth of 0.27 μm (at a concentration of 1×10^{18} cm^{-3}). The high dose boron profile extends from the surface to a depth of 0.23 μm (at a concentration of 1×10^{18} cm^{-3}). From the reasonable correlation between the depths of the fluorine and boron profiles, it is again seen that the damage from the high dose B implant has eliminated the shallow F peak down to a depth of about 0.27 μm.

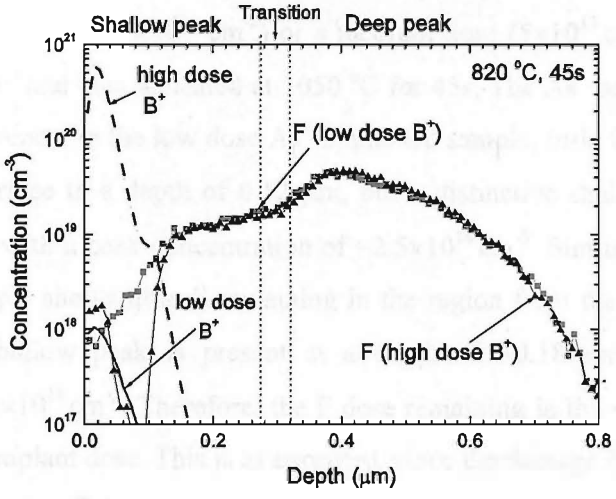

(a)

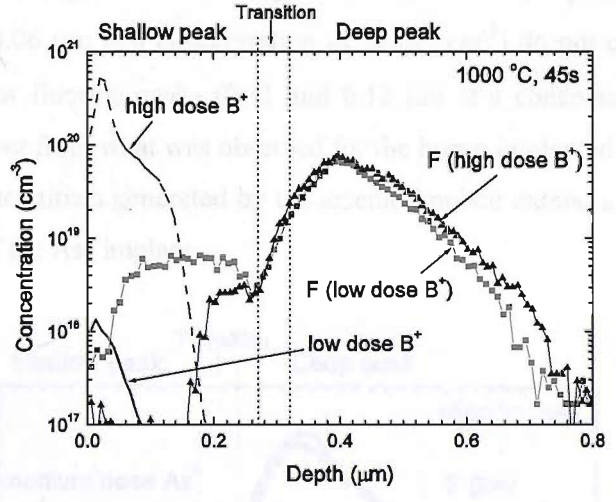

(b)

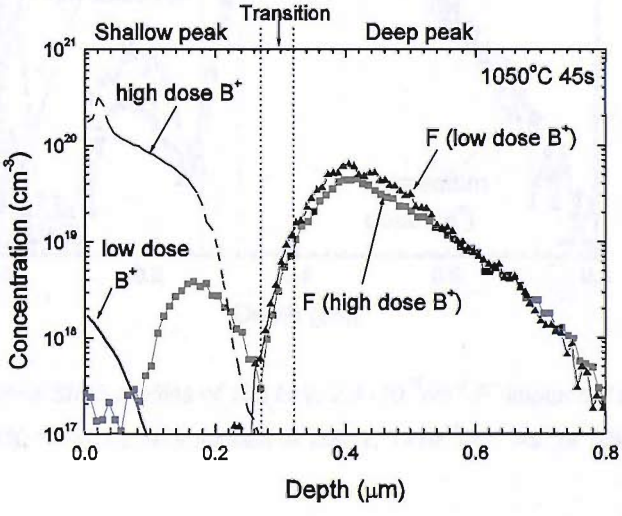

(c)

Fig. 7.7. F SIMS profiles of 185keV, 2.3×10^{15}cm^{-2} F^{+} implanted samples after a 45s anneal at 820, 1000 and 1050 °C (a-c) with a prior 5keV B^{+} implant at low dose of 7×10^{12}cm^{-2} or high dose of 2×10^{15}cm^{-2}

Finally, we compare in Fig. 7.8 F SIMS profiles of Batch 4 samples implanted with 10 keV As^+ either with a low dose (1×10^{13} cm^{-2}) or a medium dose (5×10^{13} cm^{-2}), followed by 185 keV, 2.3×10^{15} cm^{-2} F^+ and then annealed at 1050 °C for 45s. The As^+ profiles after anneal are also shown for reference. In the low dose As^+ implanted sample, little fluorine remains in the region from the surface to a depth of 0.12 μm, but a distinctive shallow peak is seen at a depth of ~0.18 μm with a peak concentration of ~2.5×10^{18} cm^{-3}. Similarly, the medium dose As^+ implanted sample shows little F remaining in the region from the surface to a depth of 0.12 μm, but a shallow peak is present at a depth of ~0.18 μm with a lower peak concentration of ~1×10^{18} cm^{-3}. Therefore, the F dose remaining in the sample decreases with an increase in As^+ implant dose. This is as expected, since the damage from a higher dose As^+ implant eliminates more F in the shallow peak and is similar to the effect seen for boron implanted samples in Fig. 7.7. Interestingly, we see that the depths of the As^+ annealed profiles (0.04 and 0.06 μm at a concentration of 1×10^{18} cm^{-3}) do not correlate well with the edges of the shallow fluorine peaks (0.11 and 0.12 μm at a concentration of 1×10^{18} cm^{-3}). This result is different from what was observed for the boron implanted samples in Fig. 7.7. It suggests that the interstitials generated by the arsenic implant extend a considerable distance beyond the range of the As^+ implant.

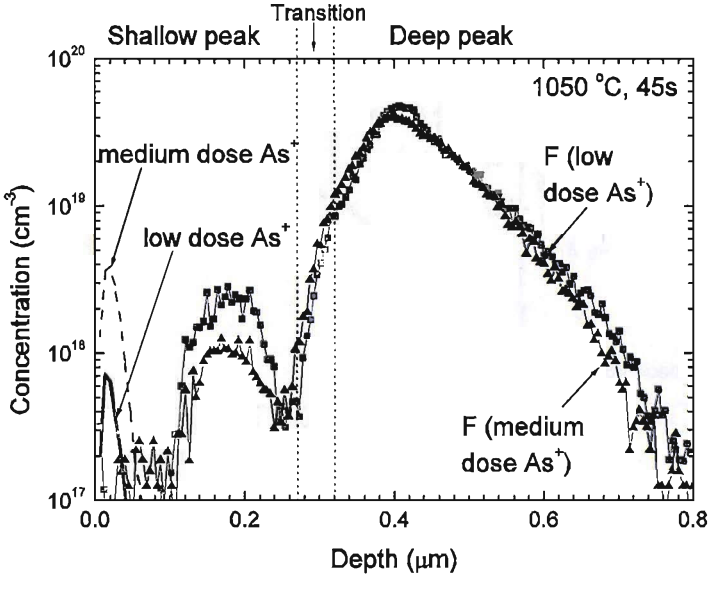

Fig. 7.8. Fluorine SIMS profiles of 185 keV, $2.3 \times 10^{15} cm^{-2}$ F^+ implanted samples after a 45s anneal at 1050 °C with a prior implant of 10keV, $1 \times 10^{13} cm^{-2}$ As^+ or 10keV, $5 \times 10^{13} cm^{-2}$ As^+.

7.4.2. Discussion

From Fig. 7.6, we see that a low dose boron implant has very little effect on the shallow fluorine peak. This suggests that there are not enough interstitials to significantly affect the V-F clusters in the shallow fluorine peak. On the other hand, Fig. 7.7 clearly shows that a high dose boron implant has a strong effect on the shallow fluorine peak. To investigate this possibility, Fig. 7.9 shows a TRIM [108] simulation of the interstitial and vacancy distributions for the results in Figs. 7.6 and 7.7. For the low dose B implant, Fig. 7.9 (a) shows that the vacancy concentration arising from the F implant is about 1000 times higher than the interstitial concentration generated by the low dose B implant at a depth of 0.02 μm (at the B implant range). This explains why the low dose B implant has little effect on the shallow F peak in Fig. 7.6. For the high dose B implant in Fig. 7.9 (b), the interstitial concentration generated by the B implant is comparable with the vacancy concentration generated by the fluorine implant down to a depth of 0.08 μm. This explains why the high dose B implant eliminates V-F clusters in the shallow F peak. It should be noted that TRIM simulation does not take into account the thermal annealing, therefore it cannot be used to precisely interpret depths of the point defects after anneal for comparison with the experimental results in Fig. 7.7 (a-c).

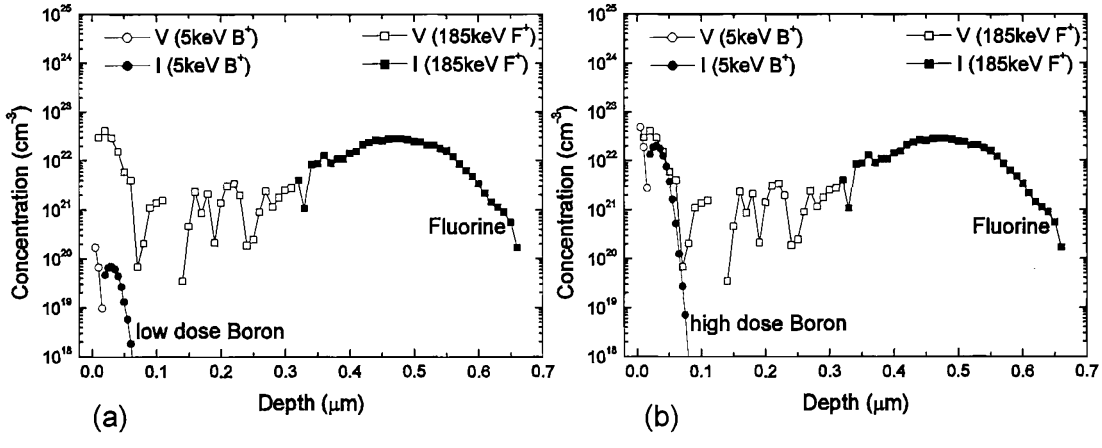

Fig. 7.9. TRIM simulation of the interstitial and vacancy distributions generated by 185 keV, $2.3\times10^{15}cm^{-2}$ F^+ and a prior implant of 5keV B^+ with a dose of either $7\times10^{12}cm^{-2}$ (a) or $2\times10^{15}cm^{-2}$(b).

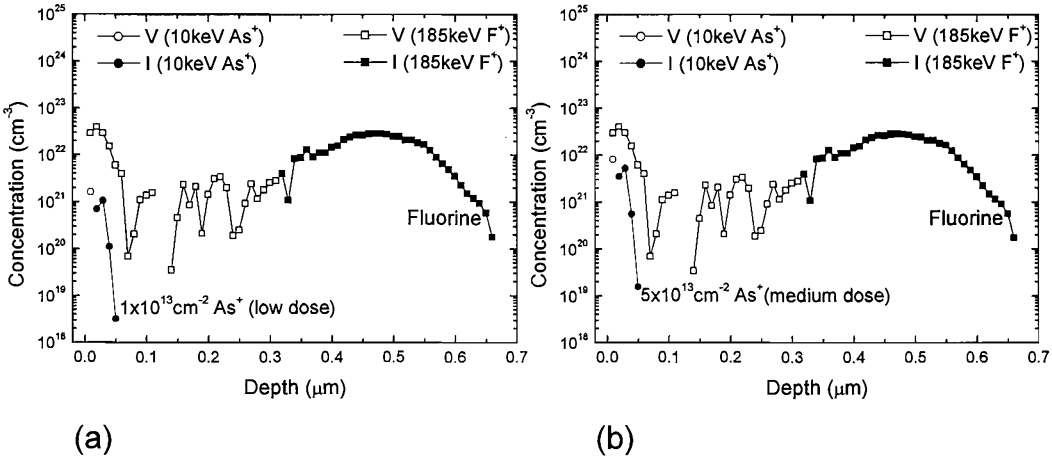

Fig. 7.10. TRIM simulation of the interstitial and vacancy distributions generated by 185 keV, $2.3\times10^{15}cm^{-2}$ F^+ and a prior implant of 10keV As^+ with a dose of either $1\times10^{13}cm^{-2}$ (a) or $5\times10^{13}cm^{-2}$(b).

Fig. 7.10 shows a TRIM simulation of the interstitial and vacancy distributions for the As^+ implants in Fig. 7.8. At a depth of 0.02 μm (at the As^+ implant range), interstitial concentrations generated by the As^+ implants are $\sim1\times10^{21}$ and $\sim5\times10^{21}$ cm^{-3} for the low dose and medium dose As^+ implants respectively. These interstitial concentrations are lower (~10-15 times) than the vacancy concentration arising from the F implant. Therefore, V-F clusters still remain after both As^+ implants as shown in Fig. 7.8, with less fluorine remaining at the higher As^+ dose. In summary, the TRIM simulation results in Figs. 7.9 and 7.10 provide strong evidence that the dopant implant damage is responsible for eliminating V-F clusters in the shallow F peak.

Next, we investigate if the dopant species has an effect on the shallow F peak. Fig. 7.11 shows an overlay of the F profiles obtained for boron and arsenic implants at different implanted doses and annealed at 1050 °C for 45s (Figs. 7.7c and 7.8). It can be seen that regardless of the implant species, the shallow F peak is eliminated up to the same depth of ~0.12 μm. This suggests that there is no direct correlation between the dopant species and the fluorine profiles. This further supports earlier results that interstitials generated by the dopant implants are responsible for the elimination of the V-F clusters in the shallow F peak. The extent of V-F cluster elimination depends primarily on the implant dose as seen again in Fig. 7.11.

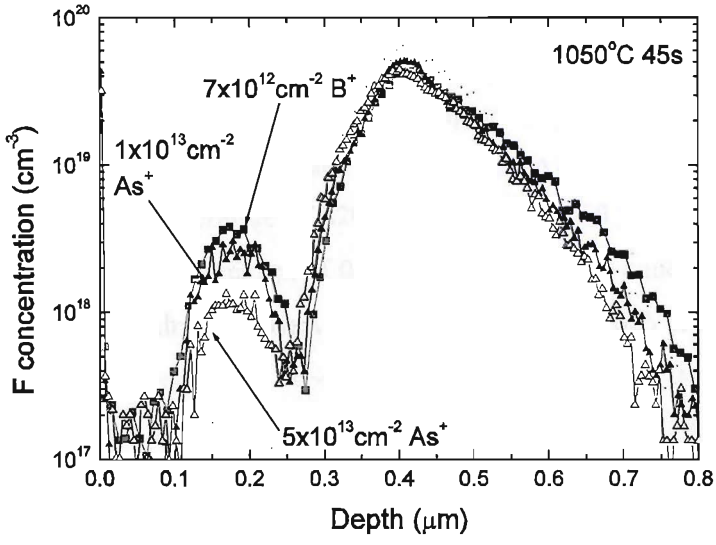

Fig. 7.11. Fluorine SIMS profiles of 185 keV, 2.3×10^{15}cm^{-2} F^{+} implanted samples after a 45s anneal at 1050°C with a prior implant of 5keV, 7×10^{12}cm^{-2} B^{+}, 10keV, 1×10^{13}cm^{-2} As^{+} or 10keV, 5×10^{13}cm^{-2} As^{+}.

In Fig. 7.12, the F dose remaining in the shallow F peak is plotted as a function of the implanted B^+ and As^+ dose for samples annealed at 1000 and 1050 °C. The dashed lines are drawn as a guide for the eyes. We can see the decreasing trend of F dose remaining in the shallow peak as the implanted B^+ and As^+ dose increases for both anneal temperatures. For a 1000 °C anneal, a substantial amount of F remains even with a high dose B co-implant. However, at the higher anneal temperature of 1050 °C, the shallow F peak is predicted to be eliminated by a co-implant at a dose of ~1x10^{14} cm^{-2}.

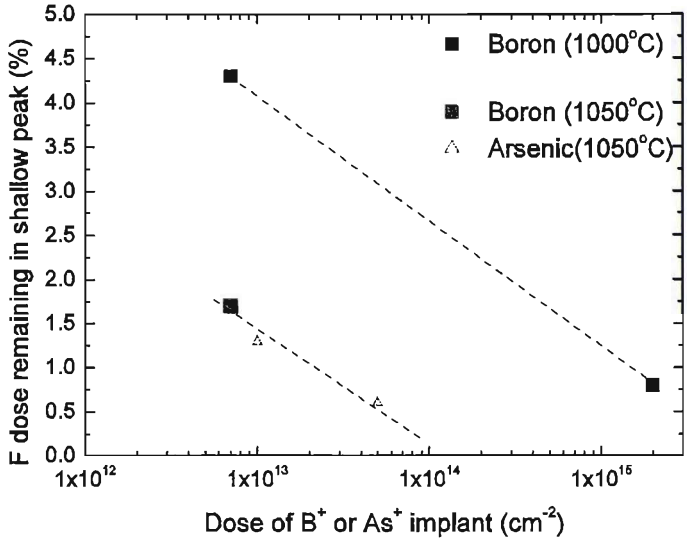

Fig. 7.12. Percentage of F dose remaining in the shallow peak of 185 keV, 2.3×10^{15}cm^{-2} F^{+} annealed at either 1000 or 1050 °C as a function of the implanted dose of B^+ and As^+

7.5. Effect of F implant energy

7.5.1. Results

In this section, we describe the effect of the F implant energy on the F SIMS profiles. Figure 7.13 shows the F SIMS profiles of Batch 4 samples given a 100 keV, 1 x 10^{15} cm^{-2} F^+ implant and a 45s anneal at a temperature of 820, 900, 1000 or 1050 °C. The as-implanted F SIMS profile shows a projected range, Rp, of 0.23 μm. At the lowest anneal temperature of 820 °C, a significant plateau is already observed at depths between 0.025 and 0.175 μm (0.1 – 0.75 Rp) with a fluorine concentration of ~ 1 x10^{19} cm^{-3}. It is also seen that the F concentration is higher than the as-implanted profile from the surface to a depth of ~0.08 μm. After a 900 °C anneal, a distinct shallow fluorine peak is formed at a depth of ~0.08 μm (0.3 Rp) and a dip in the F concentration is seen at a depth of ~0.15 μm. Again, it is seen that the F concentration is higher than the as-implanted sample from the surface to a depth of ~0.08μm. After a 1000 °C anneal, a significantly smaller shallow fluorine peak is seen at the same depth of ~0.08 μm (0.3Rp) with a peak concentration of ~1 x10^{18} cm^{-3}. After a 1000 °C anneal, the shallow F peak is dramatically smaller and has almost been eliminated. After the highest anneal temperature at 1050 °C, the shallow fluorine peak is completely eliminated. Beyond a depth of 0.18μm, the profile after 820°C anneal shows a double deep fluorine peak, with peaks at depths of ~ 0.21 μm (0.9Rp) and ~ 0.3 μm (1.3Rp) and with concentrations of ~ 2x 10^{19} cm^{-3} and ~ 3x 10^{19} cm^{-3} respectively. This double peak is seen for all anneal temperatures and it decreases in size as the anneal temperature increases.

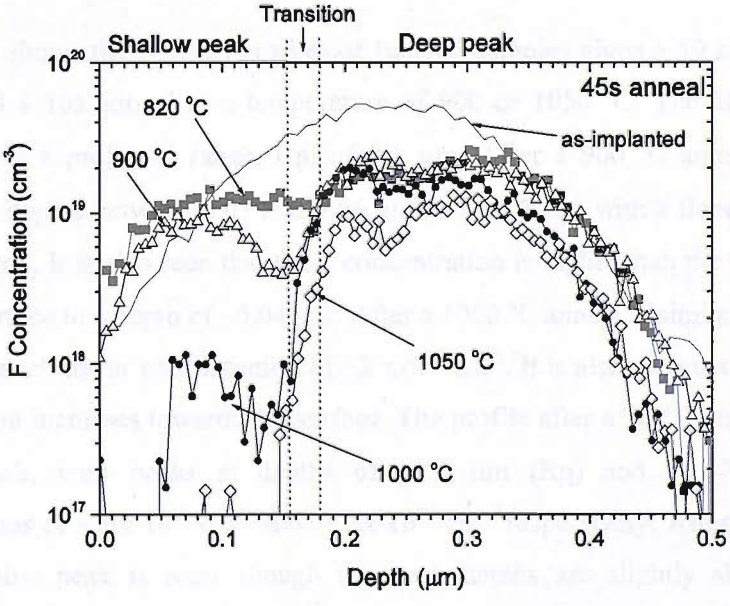

Fig. 7.13. Fluorine SIMS profiles for samples implanted with 100 keV, 1x$10^{15}$$cm^{-2}$ F^+ and annealed for 45s at 820, 900, 1000 or 1050 °C in nitrogen

Table 7.6 summarises the fluorine dose remaining in the F peaks and the transition region after annealing at different anneal temperatures. The shallow F peak was defined as extending from 0 to 0.16 μm (0- 0.7Rp), the transition region from 0.16 to 0.18 μm (0.7- 0.8Rp) and the deep peak from 0.18 to 0.5 μm (0.8- 2Rp). These definitions are at the same fractions of Rp as were used for the 185 keV F profile in Fig. 7.2. We observe that the total dose remaining is 54% for the lowest anneal temperature and it further reduces to only 18% for the highest anneal temperature. The fluorine dose in the shallow F peak, the plateau region and the deep peak generally decreases as the anneal temperature increases. However, a small increase in the F dose from 37% to 38% is seen in the deep peak on going from a 820 °C anneal to a 900°C anneal. This is an interesting result which was also observed for the 185 keV samples in Table 7.2.

		F dose remaining in different peaks (cm^{-2})			
Anneal conditions	Total dose	Plateau (0-0.16 μm)	Shallow peak (0-0.16 μm)	Transition (0.16 -0.18 μm)	Deep peak (0.18 - 0.5 μm)
As-implanted	$1.1x10^{15}$ (100%)	$2 x10^{14}$ (18%)		$1.3 x10^{14}$ (11%)	$7.8 x10^{14}$ (71%)
820 °C 45s	$5.9 x 10^{14}$ (54%)	$1.6x10^{14}$ (14%)	-	$3 x10^{13}$ (3%)	$4.0 x10^{14}$ (37%)
900 °C 45s	$5.3 x10^{14}$ (48%)	-	$1.0 x10^{14}$ (8%)	$2 x10^{13}$(2%)	$4.1 x10^{14}$ (38%)
1000 °C 45s	$3.2 x10^{14}$ (29%)	-	$8 x10^{12}$ (0.7%)	$2 x10^{13}$ (2%)	$2.9 x10^{14}$ (26%)
1050 °C 45s	$2.0 x10^{14}$ (18%)	-	$1 x10^{12}$ (<0.5%)	$7 x10^{12}$ (0.6%)	$1.9 x10^{14}$(17%)

Table 7.6. Summary of F dose remaining in the different F peaks for a 100keV F^+ implant annealed for 45s at a temperature between 820 and 1050 °C

Figure 7.14 shows the F SIMS profiles of Batch 5 samples given a 50 keV, 1 x 10^{15} cm^{-2} F^+ implant and a 10s anneal at a temperature of 900 or 1050 °C. The as-implanted F SIMS profile shows a projected range, Rp, of 0.1 μm. After a 900 °C anneal, a flat plateau is observed at depths between 0.01 and 0.06 μm (0.1– 0.6 Rp) with a fluorine concentration of ~ 4 $x10^{19}$ cm^{-3}. It is also seen that the F concentration is higher than the as-implanted sample from the surface to a depth of ~0.04 μm. After a 1000 °C anneal, a similar flat plateau is seen, but with a much lower concentration of ~2 $x10^{18}$ cm^{-3}. It is also seen that the F concentration in the plateau increases towards the surface. The profile after a 900°C anneal shows a double fluorine peak, with peaks at depths of ~0.1 μm (Rp) and ~0.17 μm (1.7Rp) with concentrations of ~ 6x 10^{19} cm^{-3} and ~ 2x 10^{19} cm^{-3} respectively. After a 1000 °C anneal, a similar double peak is seen, though the peak depths are slightly shifted and the peak concentrations are lower.

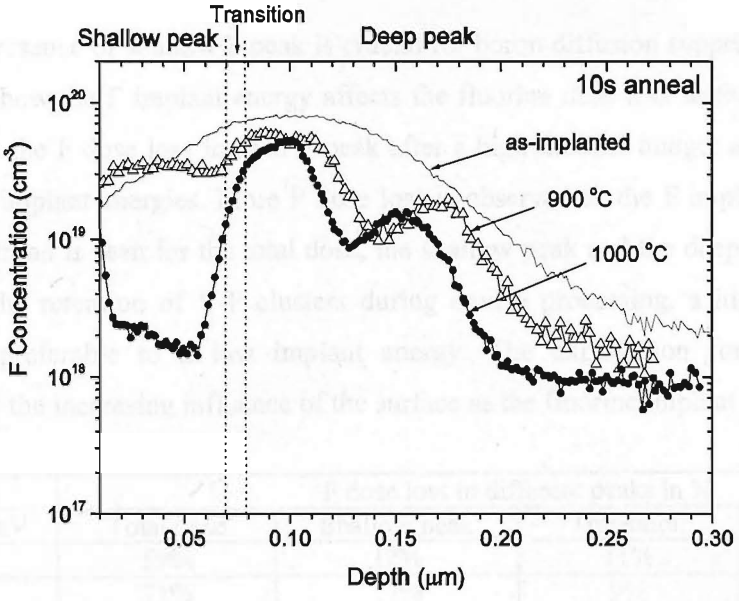

Fig. 7.14. Fluorine SIMS profiles for samples implanted with 50 keV, $1\times10^{15}cm^{-2}$ F^+ and annealed for 45s at 820, 900, 1000 or 1050 °C in nitrogen

	F dose remaining in different peaks (cm^{-2})			
Anneal conditions	Total dose	Shallow peak (0-0.07 μm)	Transition (0.07 -0.08 μm)	Deep peak (0.08 - 0.3 μm)
As-implanted	1.0×10^{15} (100%)	2.5×10^{14} (25%)	8×10^{13} (8%)	6.7×10^{14} (67%)
900 °C 10s	5.8×10^{14} (58%)	2×10^{14} (19%)	6×10^{13} (6%)	3.3×10^{14} (33%)
1000 °C 10s	2.8×10^{14} (28%)	2×10^{13} (2%)	3×10^{13} (3%)	2.3×10^{14} (23%)

Table 7.7. Summary of F dose remaining in the different F peaks for a 50keV F^+ implant annealed for 10s at a temperature between 900 and 1000 °C

Table 7.7 summarises the fluorine dose remaining after annealing at different anneal temperatures. The shallow F peak was defined as extending from 0 to 0.07 μm (0- 0.7Rp), the transition region from 0.07 to 0.08 μm (0.7- 0.8Rp) and the deep peak from 0.08 to 0.3 μm (0.8- 3Rp). These definitions are at the same fractions of Rp as were used for the 185 keV F profile in Fig. 7.2. We observe that the total dose remaining is 58% after a 900 °C anneal and it further reduces to only 28% after a 1000 °C anneal. The fluorine dose in reduction is seen in all the regions as the temperature increases. But the main reduction comes from the shallow F peak (17%) and the deep peak (10%). The dose decrease in the plateau region is only 3%.

7.5.2. Discussion

Since the presence of shallow F peak is crucial for boron diffusion suppression in silicon, we investigate how the F implant energy affects the fluorine dose loss in the sample. Table 7.8 summarises the F dose loss in each F peak after a high thermal budget anneal (1000 °C) for different F implant energies. More F dose loss is observed as the F implant energy reduces. This same trend is seen for the total dose, the shallow peak and the deep peak. Therefore, to maximise the retention of V-F clusters during device processing, a high fluorine implant energy is preferable to a low implant energy. The explanation for this behaviour is presumably the increasing influence of the surface as the fluorine implant energy is reduced.

	F dose loss in different peaks in %			
F energy, keV	Total dose	Shallow peak	Transition	Deep peak
185	59%	12%	11%	35%
100	71%	17%	9%	45%
50	72%	23%	5%	44%

Table 7.8. Summary of F dose loss in the different F peaks for different F^+ implant energies at 1000 °C anneal for times of either 10s (for 50keV) or 45s (for 100 and 185keV)

To investigate the evolution of the F profiles for different implant energies, Figure 7.15 compares normalised SIMS profiles samples implanted with 100 or 185 keV F^+ and annealed for 45 s at either 820 °C (a) or 1000 °C (b). The SIMS depth was normalised to the projected range, Rp of the F implants and the F concentration was normalised to the as-implanted F peak concentration. For the 820 °C anneal in Fig. 7.15 (a), the F plateau is not yet delineated in the 185 keV F sample but is already formed in the 100 keV F sample. This indicates that the thermal evolution of the F plateau is more advanced in samples implanted with lower implant energies. For the 1000 °C anneal in Fig. 7.15 (b), the shallow F peak is smaller in the 100 keV F sample than the 185 keV F sample. This again indicates that the thermal evolution of the shallow F peak is more advanced in samples implanted with lower implant energies. This effect could be due to the closer proximity of VF clusters to the surface, since the surface is a good recombination centre for interstitials [38]. The recombination of vacancies in the V-F clusters with interstitials diffusing to the surface would be expected to release the fluorine which would then rapidly out-diffuse.

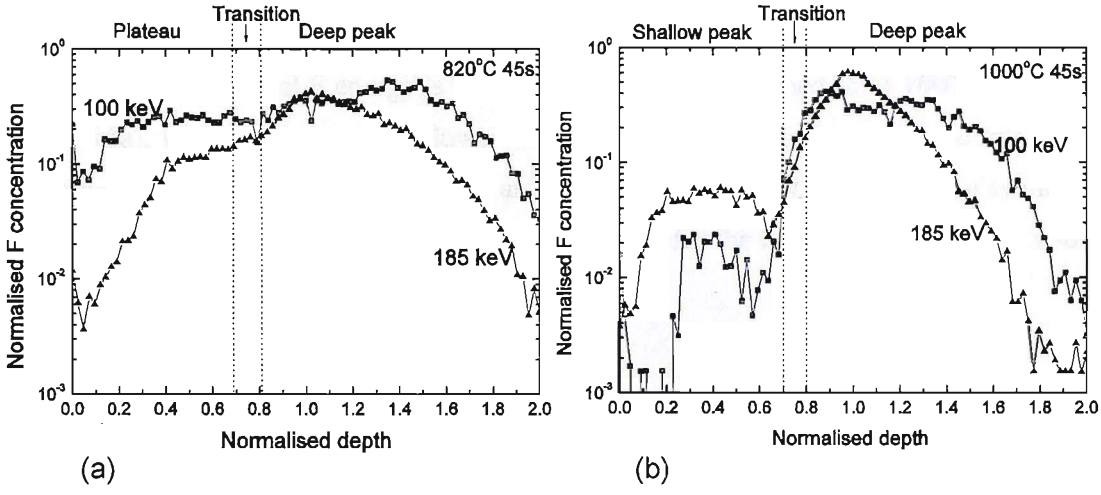

Fig. 7.15. Normalised F SIMS profiles of samples given 100 keV, $1\times10^{15}cm^{-2}$ F^+ or 185 keV, $2.3\times10^{15}cm^{-2}$ F^+ implant and annealed for 45s at either 820 °C (a) or 1000 °C (b).

For ultrashallow junctions, it is useful to estimate how much the F implant energy can be reduced and still have an effect on boron diffusion, since increasingly shallower junctions are required in MOSFET devices. Fig. 7.16 plots the normalised depth ($X_{V\text{-}F}/ R_p$) of the V-F clusters as a function of F implant energy. The normalised depth of the V-F clusters was taken from the F SIMS profiles in this work and also from the literature. For samples annealed at 1000 °C, Fig. 7.16 (a) shows that for samples implanted with energies below ~40 keV, the shallow peak is no longer clearly delineated at ~0.4 Rp. Since shallower fluorine peaks are unlikely to be due to V-F clusters, this result suggests that a fluorine implant energy above 40 keV is recommended to produce V-F clusters for annealing at 1000 °C.

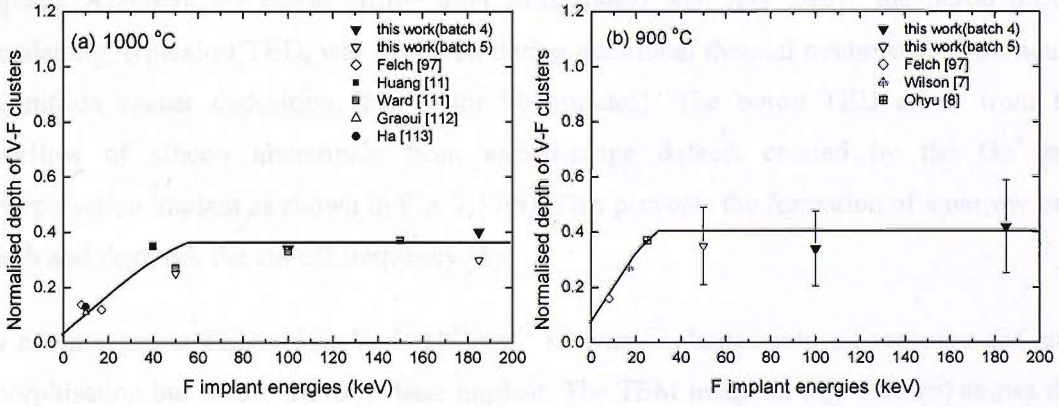

Fig. 7.16. Normalised depth of V-F clusters ($X_{V\text{-}F}/ R_p$)as a function of implant energy for F implanted samples annealed at 1000 °C(a) and 900 °C(b)

For samples annealed at the lower temperature of 900 °C, Fig. 7.16 (b) shows that the fluorine plateau, located at depths between 0.2-0.6Rp, is no longer observed for implant energies below 25 keV. This critical F energy is lower than the 40keV obtained for a 1000 °C anneal (in Fig. 7.16a), which indicates that a lower thermal budget anneal is better for the retention of V-F clusters when ultrashallow junctions are required. From Fig. 7.16 (b), we can estimate that the F implant energy can be reduced down to ~25keV for the formation of junctions with depths down to about 20nm.

7.6. Implementation of F implantation in silicon bipolar transistors

While fluorine implantation is increasingly being applied to MOS transistors [26,27], to date no work has been reported on the application of fluorine to silicon bipolar transistors. This section reports on the implementation of a fluorine implant into a production silicon bipolar technology at STMicroelectronics, Sicily, Italy. A high energy fluorine implant (150 keV) was used to position the range of fluorine implantation deeper than that of the germanium pre-amorphisation depth. It will be shown here that using a high energy fluorine implant is advantageous since it allows the V-F clusters to eliminate germanium end of range defects and suppress boron diffusion in the base of a silicon bipolar transistor, thereby resulting in an increased transistor cut-off frequency, f_T.

In a standard STMicroelectronics technology, Boron TED is encountered in the base of the transistor due to the pre-amorphisation implant which is done to prevent boron channelling. Pre-amorphisation was performed by a 80 keV, 1×10^{15} cm^{-2} Ge^+ implant before the BF_2^+ base implant. Although the boron profile after SPE anneal was very sharp, the boron profile broadening, typical of TED, was observed during additional thermal treatments, in particular the nitride spacer deposition (850°C for 90 minutes). The boron TED arises from the backflow of silicon interstitials from end-of-range defects created by the Ge^+ pre-amorphisation implant as shown in Fig. 7.17(a). This prevents the formation of a narrow base width and degrades the cut off frequency [6].

To counter boron TED, 150keV, $5x10^{14}$ cm^{-2} F^+ was implanted into silicon after Ge^+ pre-amorphisation but before the BF_2^+ base implant. The TEM image in Fig. 7.17 (b) shows that the fluorine implant eliminates the end-of-range defects from the germanium implant (seen at a depth of ~0.12μm as shown in Fig. 7.17 (a)) and instead produces a band of dislocation loops deeper in the silicon at the range of the fluorine implant at ~0.37 μm. For device

applications, this is advantageous, since the dislocation loops lie much deeper than the end of range defects and hence are further away from the device depletion regions.

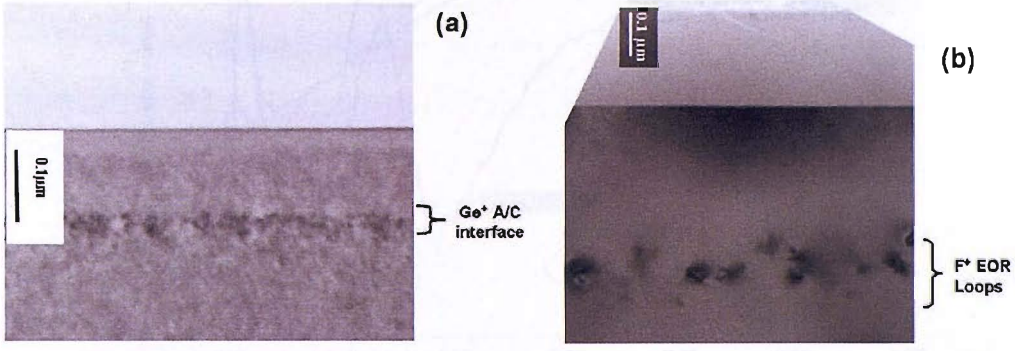

Fig. 7.17. Cross-section TEM micrographs for samples without (a) and with (b) a $5\times10^{14}cm^{-2}$ 150keV fluorine implant after the SPE anneal. The magnification bar is 0.1μm in both cases.

Fig. 7.18 shows F SIMS profiles of samples given the Ge^+ pre-amorphisation implant and a 150keV F^+ implant at $5x10^{14}$ cm^{-2}. One sample (F after final RTA) was given all the thermal treatments needed to produce a double polysilicon emitter bipolar transistor including a final anneal of 10s in N_2 at 1000°C. The second sample (F after SPE) only received the SPE anneal of 300 s at 700 °C. The fluorine profile after final RTA shows a deep peak at a depth of about 0.37μm and a shallow peak at a depth of $0.39R_p$ (0.14μm), extending to a depth of about $R_p/2$ (0.18μm). There is also an elevated fluorine concentration of $4\text{-}5\times10^{17}cm^{-3}$ extending from the shallow fluorine peak to the silicon surface. The fluorine peak at the surface is a measurement artefact due to the spacer surface layers trapping fluorine and ion beam mixing effects during analysis. The fluorine profile after the 700°C SPE anneal also shows similar key features, with a higher concentration of fluorine remaining in the sample at depths between about 0.13 and 0.36μm, perhaps due to some remaining microscopic crystal damage. On the basis of our results on fluorine implants into crystalline material (Chapters 5 and 7), we would expect the shallow fluorine peak to be due to vacancy-fluorine clusters. The vacancy-fluorine clusters could explain the absence of end of range defects from the Ge pre-amorphisation (Fig. 7.17(b)), since they would create a vacancy supersaturation in the vicinity of the end-of-range of the germanium implant. This vacancy supersaturation would be expected to suppress the formation of the end-of-range defects through a mechanism of interstitial annihilation by the V-F clusters. This benefit arises by placing the range of fluorine implantation deeper than that of the Ge pre-amorphisation interface.

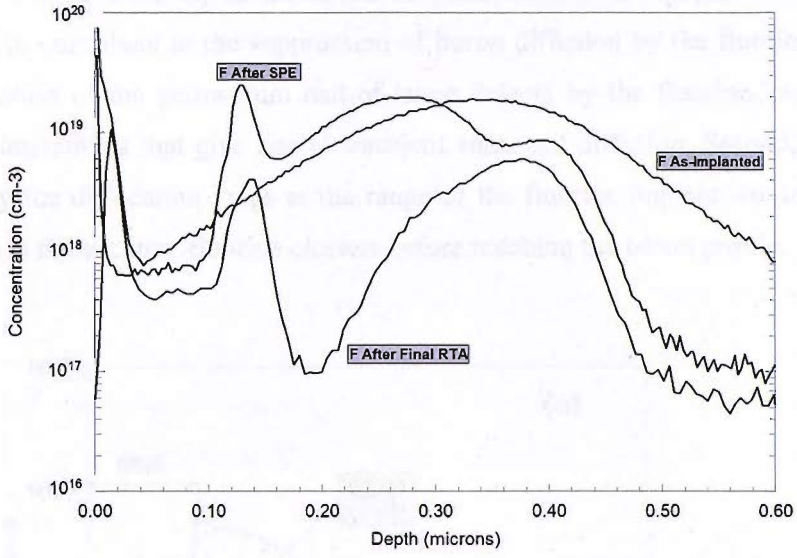

Fig.7.18. SIMS profiles for samples given a germanium pre-amorphisation implant and a 150keV F^+ implant at $5x10^{14}$ cm^{-2}. One sample was given all the thermal treatments needed to produce a double polysilicon emitter bipolar transistor, including solid phase epitaxy anneal, a vapox deposition and densification, a nitride spacer deposition of 90mins at 850°C and a final anneal of 10s in N_2 at 1000°C. The second sample only received the SPE anneal of 300s at 700°C.

Fig. 7.19 shows boron and fluorine SIMS profiles for transistor structures implanted with 80 keV, 1×10^{15} cm^{-2} Ge^+ for pre-amorphisation, with different doses of fluorine at 150keV and with a 14keV BF_2^+ base implant. For fluorine doses of 1 and $2\times10^{14}cm^{-2}$ in Fig.7.19(a), a fluorine peak can be seen at the polysilicon/silicon interface, but no $R_p/2$ fluorine peak is present. The deep fluorine peak at the range of the fluorine implant was also present, but is not shown in Fig.7.19 (a) for the sake of clarity. The boron profiles in Fig.7.19(a) are reasonably broad, giving junction depths of 0.103 and 0.108μm respectively at collector doping concentrations of $1\times10^{17}cm^{-3}$. These boron profiles show the presence of significant boron diffusion during the 90mins at 850°C nitride spacer deposition. In contrast, for a fluorine dose of $5\times10^{14}cm^{-2}$, Fig.7.19(b) shows that the $R_p/2$ fluorine peak is now present both after the nitride spacer deposition and after the final rapid thermal anneal. Furthermore, the boron profile is much sharper and does not change much with the final rapid thermal anneal. At a doping concentration of $1\times10^{17}cm^{-3}$, the junction depth is 0.070μm. These results show that a critical fluorine dose of $2\text{-}5\times10^{14}cm^{-2}$ exists, above which a significant suppression of boron diffusion is obtained and below which the fluorine has no effect. Furthermore, this critical fluorine dose for boron diffusion suppression correlates with the appearance of the $R_p/2$ fluorine peak on the SIMS profile. This fluorine peak is attributed to fluorine trapped in vacancy-fluorine clusters. This result is consistent with the effect of V-F clusters in

crystalline silicon samples, as discussed in Section 6.2.1 of Chapter 6. Two factors are postulated to contribute to the suppression of boron diffusion by the fluorine implant. First, the elimination of the germanium end-of-range defects by the fluorine implant removes a source of interstitials that give rise to transient enhanced diffusion. Second, any interstitials released by the dislocation loops at the range of the fluorine implant would be expected to recombine at the vacancy-fluorine clusters before reaching the boron profile.

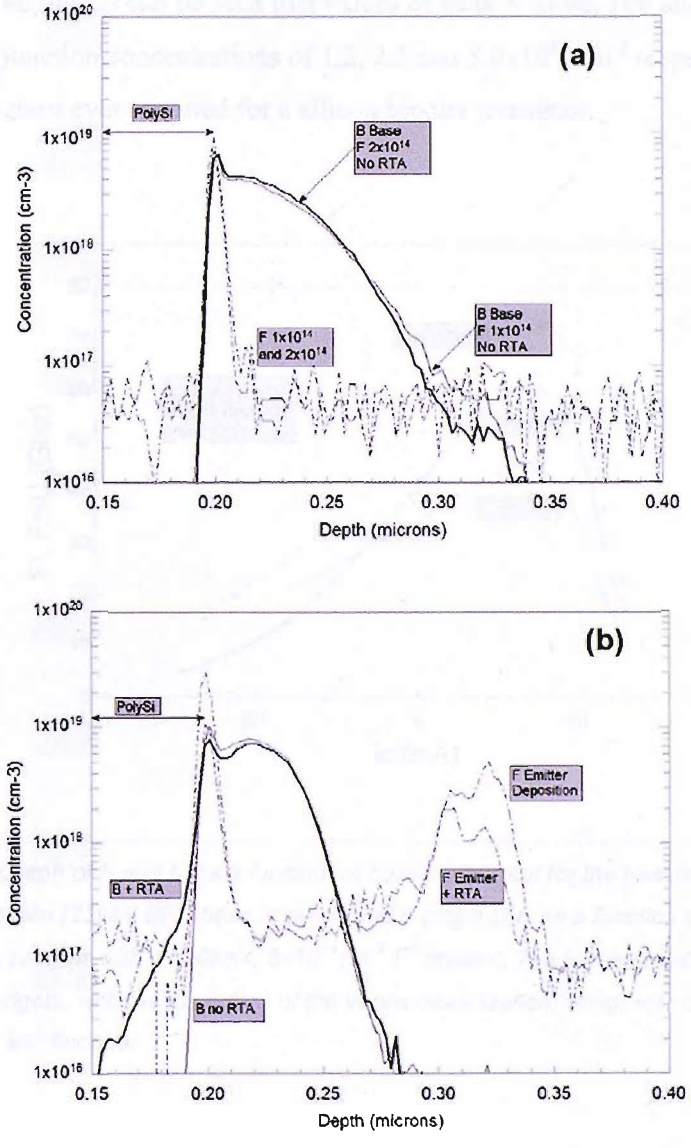

Fig. 7.19. Boron and fluorine SIMS profiles for transistor structures implanted with germanium for pre-amorphisation, with different doses of fluorine at 150keV and with a 14keV BF_2^+ base implant. The wafers received all the thermal treatments needed to produce a double polysilicon emitter bipolar transistor except the vapox anneal. For the low fluorine dose results (a) the final rapid thermal anneal was also omitted, whereas for the high fluorine dose results (b), a comparison is made of profiles with and without the final rapid thermal anneal.

Fig. 7.20 shows a graph of f_T as a function of collector current in transistors given a 22keV BF_2^+ base implant and with or without a 150keV, $5\times10^{14}cm^{-2}$ F^+ implant. It can be seen that the fluorine implant increases the maximum f_T from 46 GHz to 60 GHz. For completeness Fig. 7.20 also shows values of maximum oscillation frequency, f_m, as a function of collector current for the fluorine implanted transistor and a peak f_m of 72 GHz is obtained. Further optimization on the collector doping was performed by varying the collector implant doses. Fig. 7.21 shows a graph of f_T as a function of collector current for three different values of collector doping. It can be seen that values of peak f_T of 90, 100 and 110GHz are obtained for collector junction concentrations of 1.2, 2.5 and 5.0×10^{17} cm^{-3} respectively. These values of f_T are the highest ever reported for a silicon bipolar transistor.

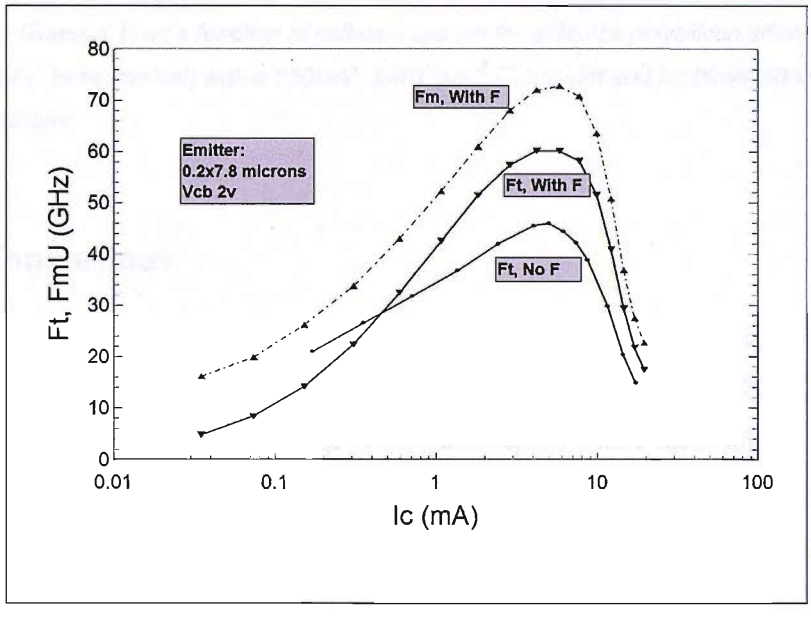

Fig. 7.20. Graph of f_T and f_m as a function of collector current for the baseline double polysilicon silicon bipolar process (22keV BF_2^+ base implant) and a graph of f_T as a function of collector current for an analogous process with a 150keV, $5\times10^{14}cm^{-2}$ F^+ implant. The two types of transistor received the same thermal budgets, with the exception of the vapox densification, which was omitted for the transistor implanted with fluorine.

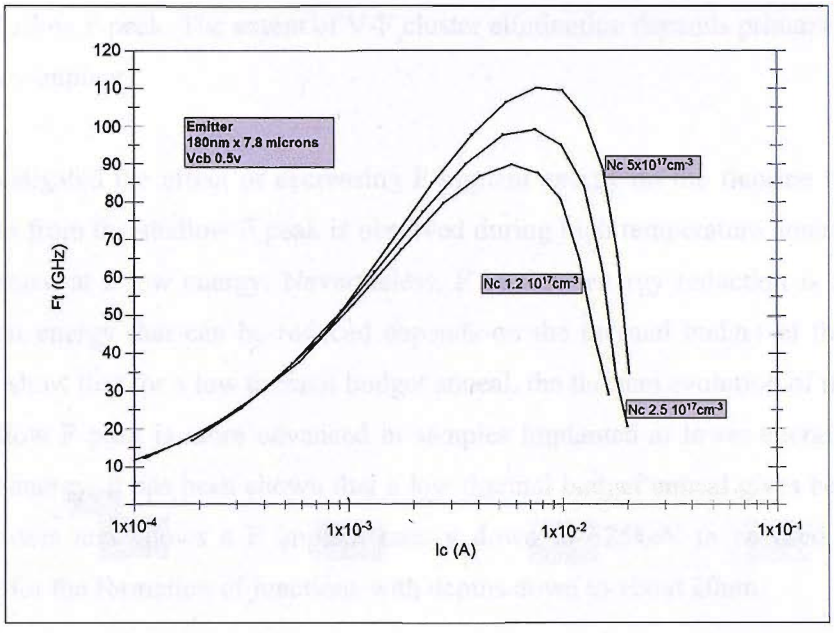

Fig. 7.21. Graph of f_T as a function of collector current for a double polysilicon silicon bipolar process (14keV BF_2^+ base implant) with a 150keV, $5x10^{14}cm^{-2}$ F^+ implant and for three different collector doping concentrations.

7.7. Conclusions

In summary, a study has been made of the effect of device processing on V-F clusters for anneal temperatures in the range 820 to 1050 °C. After annealing at 820 °C, a fluorine plateau is formed in the region of 0 -0.7 Rp, in the same region where the shallow F peak is formed at a higher anneal temperature. The F plateau is very stable at 820 °C and is transformed into a shallow F peak on annealing at a higher temperature. Analysis of F SIMS profiles has shown the F plateau is due to V-F clusters. Comparing the F SIMS profiles after 900 °C and 1050 °C anneals, it is shown that the transformation from a F plateau to a distinctive shallow F peak takes place by losing F at the surface and at the interface between the shallow peak and the deep peak (transition region). The annealing of V-F clusters at the surface can be explained by surface recombination and at the transition interface by the close proximity of V-F clusters to the interstitial-rich region at Rp.

The fluorine behaviour in the presence of damage from co-implanted B^+ or As^+ has also been investigated. It is seen that a low dose boron implant has very little effect on the shallow fluorine peak while a high dose boron implant eliminates the shallow fluorine peak. A similar effect on the shallow fluorine peak is seen for As^+ implants. Vacancy and interstitial distributions of F and dopant co-implants obtained by TRIM simulation show that the damage arising from the dopant co-implants is responsible for the elimination of V-F clusters

in the shallow F peak. The extent of V-F cluster elimination depends primarily on the dose of dopant co-implant.

We investigated the effect of decreasing F implant energy on the fluorine behaviour. More dose loss from the shallow F peak is observed during high temperature anneal when fluorine is implanted at a low energy. Nevertheless, F implant energy reduction is feasible and the minimum energy that can be reduced depends on the thermal budget of the anneal. SIMS profiles show that for a low thermal budget anneal, the thermal evolution of the F plateau and the shallow F peak is more advanced in samples implanted at lower energies. For a low F implant energy, it has been shown that a low thermal budget anneal gives better retention of V-F clusters and allows a F implant energy down to ~25keV to be used. This energy is suitable for the formation of junctions with depths down to about 20nm.

Finally, a study has been made of the use of a high energy fluorine implantation for boron diffusion suppression in a double polysilicon silicon bipolar technology. The suppression of boron TED is seen, which correlates with the appearance of a shallow fluorine peak on the SIMS profiles at a depth of approximately $R_p/2$, and this peak is attributed to vacancy-fluorine clusters. It has been proposed that the fluorine implantation also eliminates the germanium end of range defects. Therefore, the introduction of a fluorine implant into the process flow of a double polysilicon silicon bipolar transistor increases the cut-off frequency from 46 to 60GHz. Additional optimisation of the base and collector profiles leads to a further increase in cut-off frequency to 110GHz. This value of f_T is the highest ever reported for a silicon bipolar transistor.

Chapter 8

Conclusions and Future Work

In this work, a study has been made of the effect of point defect injection on ion implanted fluorine profiles and boron marker layers located at different depths during anneal at 1000 °C. SIMS analysis has shown fluorine peaks at depths of $0.3R_p$ and R_p and a shoulder between $0.5\sim0.7R_p$ after annealing of a 185keV, 2.3 $x10^{15}$ cm^{-2} F^+ implant. The shallow fluorine peak at a depth of $0.3R_p$ is smaller under interstitial injection than inert anneal condition and it decreases in size with anneal time. The presence of this shallow peak correlates with the suppression of boron diffusion in a boron marker located at the same depth. Therefore, these results provide strong evidence that the shallow fluorine peak is due to vacancy-fluorine clusters and that these clusters are responsible for the suppression of boron diffusion. The elimination of the shallow fluorine peak has been explained by the annihilation of vacancies in the clusters by recombination with injected interstitials.

The behaviour of the dislocation loops and their effect on boron diffusion has been investigated. For boron peaks located in the interstitial-rich region of the fluorine damage profile, the boron diffusion coefficient shows surprisingly a lower value under interstitial injection than under inert anneal. Plan-view TEM micrographs show that the dislocation loops are larger and fewer under interstitial injection than inert anneal. It is therefore proposed that the injected interstitials are accelerating evolution of interstitial defects into dislocation loops, that is accelerating the Ostwald ripening process.

A detailed, systematic study has been made of the V-F clusters under a wide range of processing conditions which are of interest for device fabrication. SIMS analysis shows that samples annealed at 820 °C exhibit a fluorine plateau in the region of 0 -0.7 Rp, in the same region where the shallow F peak is formed at a higher anneal temperature. The F plateau is very stable at 820 °C and is transformed into a shallow F peak on annealing at a higher temperature. Analysis of F SIMS profiles has shown the F plateau is due to V-F clusters.

The effect of damage from a dopant co-implant on the V-F clusters has also been investigated. It is seen that a high dose boron implant eliminates the shallow fluorine peak. A similar effect on the shallow fluorine peak is seen for As^+ implants. TRIM simulations of the vacancy and interstitial distributions of F and dopant co-implants show that the damage arising from the dopant co-implants is responsible for the elimination of V-F clusters in the shallow F peak. The extent of V-F cluster elimination depends primarily on the dose of the dopant co-implant.

A study has been made of the feasibility of reducing the fluorine implant energy and its effect on the fluorine behaviour. More dose loss from the shallow F peak is observed during high temperature anneal when fluorine is implanted at a low energy. Nevertheless, F implant energy reduction is feasible and the minimum energy that can be used depends on the thermal budget of the anneal. For a low F implant energy, it has been shown that a low thermal budget anneal gives better retention of V-F clusters and allows a F implant energy down to ~25keV to be used. This energy is suitable for the formation of junctions with depths down to about 20nm.

Finally, a study has been made of the use of fluorine implantation for boron diffusion suppression in a double polysilicon silicon bipolar technology. It is shown that the fluorine implant increases the cut-off frequency from 46 to 60GHz. Additional optimisation of the base and collector profiles leads to a further increase in cut-off frequency to 110GHz.

This work has unambiguously shown that V-F clusters are responsible for the suppression of boron diffusion in silicon. The analysis was mainly based on the SIMS profiles and it would be useful to study other characterisation methods like positron annihilation spectroscopy to get further information on the physical nature of the V-F clusters.

We saw that the V-F clusters in silicon are stable under a wide range of temperatures. It would be interesting and important to investigate the behaviour of the V-F clusters in other materials such as silicon-germanium, SOI, strained silicon and strained germanium, which are of current interest for MOS and bipolar device applications. Moreover, this work mainly focussed on the boron diffusion, it would be interesting to study the effect of fluorine implantation on the diffusion of phosphorus and arsenic, which are currently in use in device fabrication.

This work showed the evolution of V-F clusters from a fluorine plateau at a lower anneal temperature (~820 °C) to a distinctive shallow fluorine peak at a higher anneal temperature. The annealing was performed using rapid thermal annealers. This behaviour should be

investigated by using advanced annealing techniques such as spike anneal, flash anneal and laser annealing.

This work has looked into various device processing conditions and how they affect the fluorine behaviour. More work still needs to be done for each condition to characterise the fluorine behaviour in greater detail in order to develop mathematical models for the effect of fluorine on boron diffusion.

Appendix I

ATHENA Simulation Procedure

(a) ATHENA Input File to extract Boron Diffusion Coefficient

(To be used together with the optimizer program shown in the (b))

```
go athena
# define grid structure for substrate
line     x location=0.00 spacing=0.10
line     x location=0.10 spacing=0.10
line     y location=0.00 spacing=0.002
line     y location=0.80 spacing=0.002

# initialize substrate
initialize  silicon orientation=100

#load the as-grown boron profile and convert it to the program mesh co-ordinates
profile infile= asgrown.txt boron
extract name="asgrown" curve(depth,impurity="boron" material="Silicon"\
  mat.occno=1 x.val=0.05) outfile = "asgrown.dat"

#Choosing diffusion model
method fermi
set xdelta=0.0001

# Define diffusion parameters
impurity i.boron acceptor silicon Dix.0=5e-14 Dix.E=0.0 Dip.0=0.0 Dip.E=0.0
impurity i.boron acceptor silicon Dim.0=0.0 Dim.E=0.0 Dimm.0=0.0 Dimm.E=0.0
impurity i.boron acceptor silicon Dvx.0=0.0 Dvx.E=0.0
impurity i.boron acceptor silicon Dvm.0=0.0 Dvm.E=0.0 Dvmm.0=0.0 Dvmm.E=0.0
impurity i.boron acceptor silicon Fi.0=0.94 Fi.E=0.0

#Diffusion process
diffus time=     15/60    temp=   1000
extract name="Si" curve(depth-$"xdelta",impurity="Boron" material="Silicon" \
        mat.occno=1 x.val=0.05) outfile="fit.dat"
quit
```

(b) Optimizer window settings and an example of the result

(i) Parameter setting- the diffusion coefficient, 'Dix.0'

Deckbuild: Optimizer – (NONE) (edited)

Mode: Parameters | File | View | Edit | Print | Optimize | Properties...

Line number	Parameter name	Response type	Optimized value	Initial value	Minimum value	Maximum value
18	impurity Dix.0	linear	---	5e-14	2.5e-15	7.5e-11

(ii) Target setting: the target is the concentration of measured B profile.

Deckbuild: Optimizer – (NONE) (edited)

Mode: Targets | File | View | Edit | Print | Optimize | Properties...

Line number	Target name	Target type	X value	Target value	Optimized value	Error (%)	Weight
22	Si	log	3.64E-01	9.73E+16	---	---	0.26
22		log	3.70E-01	9.82E+16	---	---	0.27
22		log	3.75E-01	1.07E+17	---	---	0.29
22		log	3.81E-01	1.08E+17	---	---	0.30
22		log	3.86E-01	1.31E+17	---	---	0.36
22		log	3.92E-01	1.50E+17	---	---	0.40
22		log	3.97E-01	1.71E+17	---	---	0.44
22		log	4.03E-01	2.38E+17	---	---	0.54
22		log	4.08E-01	3.62E+17	---	---	0.67

(iii) Result window- showing the average error, diffusion coefficient value (Dix.0) and the fitted profiles

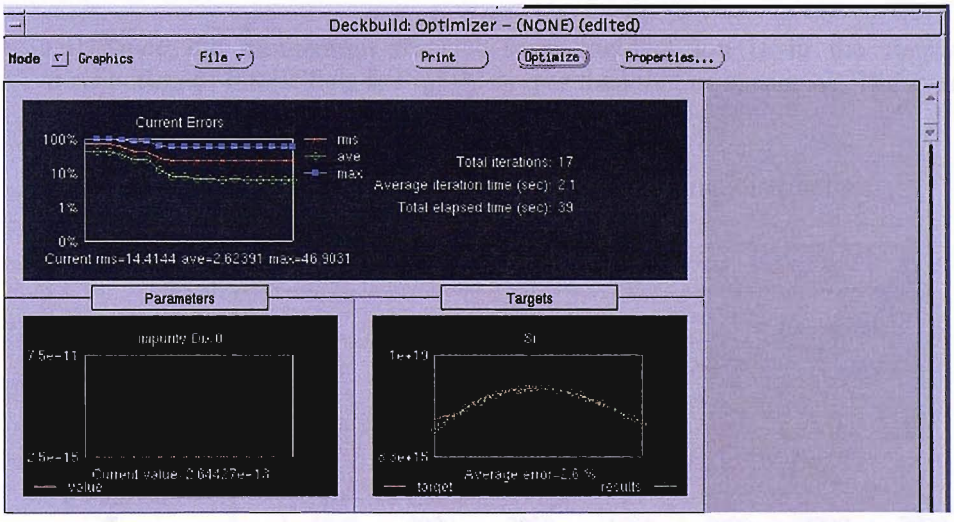

Appendix II

TRIM Simulation procedure

Below are the steps taken to convert TRIM raw data (defect count vs. depth) to final graph (defect concentration vs. depth) for a 185keV, 2.3×10^{15} cm^{-2} F^{+} implant.

(i) TRIM output : Defect counts (Vacancies and Interstitials) per implanted F ion as a function of depth

F projected range, Rp = 4000 Å, straggle, ΔRp = 1000 Å
Total Target vacancies = 1694 /ion
Total Target displacements (Si recoils) = 1838 /ion

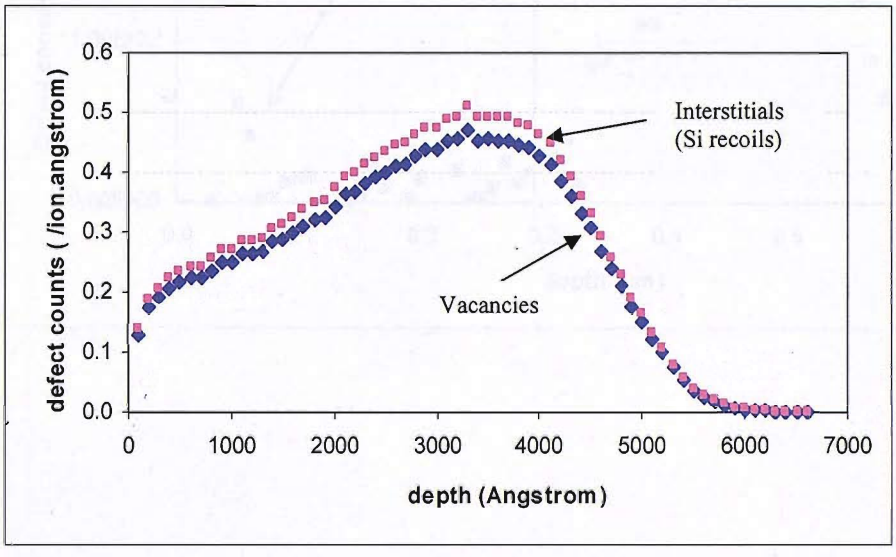

(ii) Since the momentum transfer from incident ion is in the forward direction, the distribution of interstitials is slightly deeper than that of vacancies. The average separation of I and V distributions is approximated by Rp-ΔRp.

(iii) Subtract the vacancy distribution from the interstitial distribution.

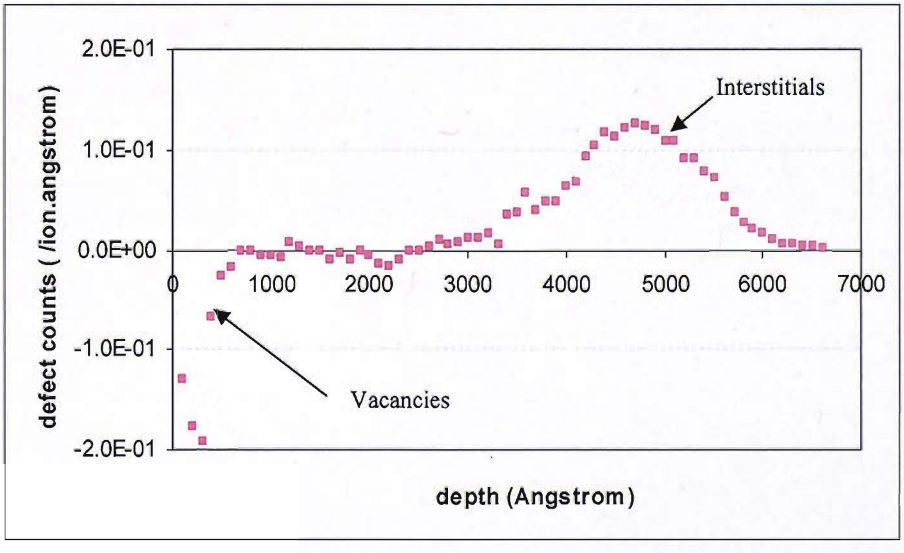

(iv) Convert into concentration profile (counts/cm^3) by multiplying with 2.3×10^{15} cm^{-2} (F dose) and 10^8 (to change unit from per Å to per cm). Finally, display vacancies distribution in the positive scale for easier viewing.

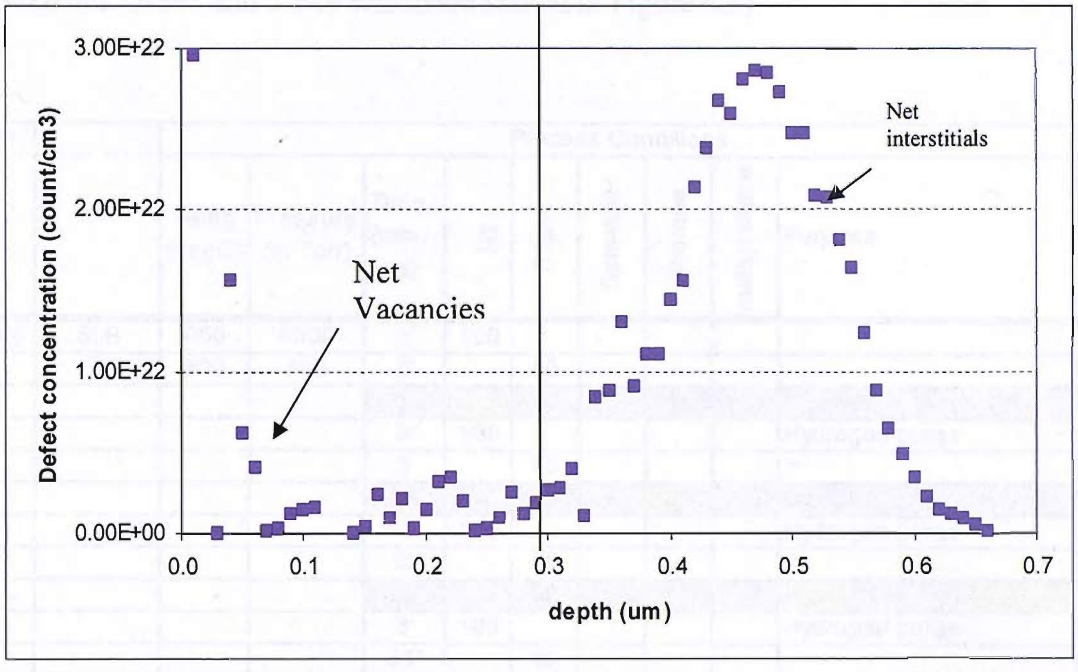

Appendix III

Recipe for the growth of boron marker layers in Si and SiGe

(Growth nos. 5-548 and 5-549 which are shown in Figure 4.3)

Run		Process Conditions								
		Temp (degC)	Pressure (m Torr)	Time (min, sec)	H2	Silane	Germane	diborane	methyl silane	Purpose
5-548	Si:B	950	1000	3'	100					
		800	500	9'		50				
				16"		50		15		B peak 4
				3'	100					Hydrogen purge
				3'		50				
				16"		50		15		B peak 3
				3'	100					Hydrogen purge
				3'		50				
				16"		50		15		B peak 2
				3'	100					Hydrogen purge
				83"		50				
				16"		50		15		B peak 1
				3'	100					Hydrogen purge
				83"		50				
5-549	SiGe:B	950	1000	3'	100					
		800	500	5'12"		50				
				38"		50	15			SiGe
				12"		50	15	15		B peak 4
				3'	100					Hydrogen purge
				2'		50				
				38"		50	15			SiGe
				12"		50	15	15		B peak 3
				3'	100					Hydrogen purge
				2'		50				
				38"		50	15			SiGe
				12"		50	15	15		B peak 2
				3'	100					Hydrogen purge
				1'36"		50				
				19"		50	15			SiGe
				12"		50	15	15		B peak 1
				19"		50	15			SiGe
				3'	100					Hydrogen purge
				1'12"		50				

Appendix IV

Process Batch Listing (Defect injection experiment)
Batch name: K2838s

step	ID	Description
1	P-EM	E-BEAM Mask/ Reticle Writing
2	G-S12	Title page: 2 wafers, Material: p-type CZ(100) 17-33 ohm-cm
3	G-1P	Lithography notes
4	G-1	Notebook page
	Epi	**Epitaxial layer, growth of boron markers**
5	W-C6	*Pre-epitaxy clean: RCA + brief dip in HF:H2O 1:100 to thin RCA oxide
6	LE-0	Low-pressure epitaxy Si:B
7	LE-0	Low-pressure epitaxy SiGe:B
	Implant	**Implant fluorine into top half of the wafers**
8	PX-H17	Photolitho Half-Mask: nom. 1.7um resist
9	P-RHBI	Hard bake for implant
10	IF-0	Implant fluorine: 2.3E15 /cm2 185keV to TOP Half of the wafer
11	P-RS	Resist strip
	Deposit	**Deposit LTO, Si3N4 and sawing**
12	W-C2	Fuming nitric acid clean, 2nd pot only
13	LO-100	LTO deposition: 100nm+/-15nm at 400 degC SiH4 and O2
14	G-3	Special instructions: Saw each wafer into half. Further saw into 3 pieces (L,C,R) as shown in diagram. Saw R into 1cmx1cm pieces. **Check the saw blade is not contaminated.**
15	W-C2	Fuming nitric acid clean, 2nd pot only
16	WH-7D1	Dip etch, 7:1 BHF 25degC. To hydrophobic Si +20sec for wafer sections L and all pieces from wafer section R
17	LD-N0	PECVD NITRIDE deposition; Deposit 130nm+/-20nm at 300 degC on wafer sections L and C
18	G-3	Special instructions: Saw wafer sectionsL and C into 1cmx1cm pieces. **Check the saw blade is not contaminated.**
	anneal	**RTA**
19	W-C2	Fuming nitric acid clean, 2nd pot only
20	RA-0	AG-RTA stage: process conditions to be confirmed
		Stripping of capped layers before SIMS analysis
21	WH-2D2	Dip etch, 20:1 BHF 25degC 15 to 20s.
22	WN-1	Strip/wet etch Si3N4, Orthophosphoric acid at 160degC
23	WH-7D1	Dip etch, 7:1 BHF 25degC. To hydrophobic Si+20sec.

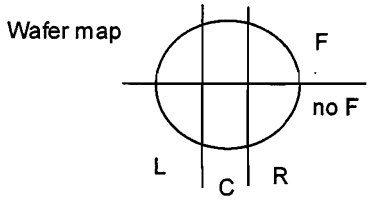

Bibliography

1. D. Kahng and M. M. Atalla, IRE Device Research Conference, Pittsburgh, 1960.
2. International Technology Roadmap for Semiconductors (ITRS), http://public.itrs.net
3. R. B. Fair, J. J. Wortman and J. Liu, J. Electrochem. Soc. 131, 2387 (1984).
4. K. Cho, M. Numan, T. G. Finstad, W. K. Chu, J. Liu and J. J. Wortman, Appl. Phys. Lett. 47, 1321 (1985).
5. Y. Taur and T. Ning, *Fundamental of modern VLSI devices*, Cambridge University Press, New York, USA (1998).
6. S.M.Sze, *Semiconductor Devices Physics and Technology*, 2nd Edition, John Wiley & Sons, 2002.
7. R. G. Wilson, J. Appl. Phys. 54, 6879 (1983).
8. K. Ohyu, T. Itoga and N. Natsuaki, Jap. J. Appl. Phys. 29, 457 (1990).
9. D. Fan, J.M. Parks and R.J. Jaccodine; Appl. Phys. Lett., vol. 59, pp. 1212-1214 (1991).
10. L.Y. Krasnobaev, N.M.Omelyanovskaya, V.V. Makarov, Jnl. Appl. Phys., vol. 74, pp. 6020-6022 (1993).
11. T.H.Huang, H.Kinoshita and D.L.Kwong, Appl. Phys. Lett. vol 65, pp1829-1831 (1994).
12. T. Shano, R. Kim, T. Hirose, Y. Furuta, H. Tsuji, M. Furuhashi and K. Taniguchi, Proc. International Electron Devices Meeting, 821 (2001) 37.4.1.
13. A. Mokhberi, R. Kasnavi, P. B. Griffin and J. D. Plummer, Appl. Phys. Lett., 80 (2002) 3530.
14. E. Ishida, D. F. Downey, K. S. Jones, J. Liu, Proceedings of the International Conference on Ion Implantation Technology, v2, 909, (1999)
15. T. Noda, J. Appl. Phys. 96, (2004) 3721.
16. J. M. Jacques, L.S. Robertson, K. S. Jones, M.E.Law, M.Rendon and J.Bennett, App Phys Lett, vol 82, pp3469-3471 (2003)
17. J. M. Jacques, L.S. Robertson, A. Li-Fatou, C. M. Hazelton, E. Napolitani, L. M. Rubin and K. S. Jones, J. App. Phys. 98, 073521-1 (2005)
18. H. A. W. El Mubarek and P. Ashburn, Appl. Phys. Lett., 83 (2003) 4134.
19. G. Impellizzeri, J. H. R. dos Santos, S. Mirabella, F. Priolo, E. Napolitani and A. Carnera, Appl. Phys. Lett., 84 (2004) 1862.
20. D. F. Downey, J. W. Chow, E. Ishida and K. S. Jones, Appl. Phys. Lett. 73, 1263 (1998).
21. H. Graoui, M. Hilkene, B. McComb, M. Castle, S. Felch, et al., Proc. MRS., Vol. 810, p. 247, 2004.
22. N.E.B.Cowern, B.Colombeau, J.Benson, A.J.Smith, W.Lerch, S.Paul, T.Graf, F.Cristiano, X.Hebras, DBolze, App. Phys. Lett. vol 86, pp2055-2057 (2005)

23. S. Mirabella, G. Impellizzeri, E. Bruno, L. Romano, M. G. Grimaldi, E. Napolitani, A. Carnera and F. Priolo, Appl. Phys. Lett., 86 (2005) 121905-1.
24. H. A. W. El Mubarek, M. Karunaratne, J. M. Bonar, G. D. Dilliway, Y Wang, P. L. F. Hemment, A. F. Willoughby and P. Ashburn, IEEE Trans. Electron Devices, 52, 4, (2005) 518.
25. H. A. W. El Mubarek, J. M. Bonar, G. D. Dilliway, P. Ashburn, M. Karunaratne, A. F. Willoughby, Y Wang, P. L. F. Hemment, R. Price, J. Zhang and P. Ward, J. Appl. Phys., 96 (2004) 4114.
26. K.Liu, J.Wu, J.Chen, A.Jain, IEEE Electron Device Lett., vol 24, pp180-182 (2003).
27. H.Fukutome, Y.Momiyama, H.Nakao, T.Aoyama, H.Arimoto, Tech. Dig. – Int. Electron Devices Meet., pp485-488 (2003).
28. A. F. W. Willoughby, J. Phys. D 10, 455 (1977).
29. W. K. Hofker, H. W. Werner, D. P. Oosthoek, and H. A. M. de-Grefte, Appl. Phys. 2, 265 (1973).
30. R. T. Hodgson, V. Deline, S. M. Mader and J. C. Gelpey, Appl. Phys. Lett. 44, 589 (1984).
31. J. J. Hamilton, N. E. B.Cowern, J. A. Sharp, E. J. H. Collart, B. Colombeau, M. Bersani, D. Giubertoni, A. Parisini and K. J. Kirkby, Appl. Phys. Lett. 89, 042111 (2006).
32. A. E. Michel, W. Rausch, P. A. Ronsheim and R. H. Kastl, Appl. Phys. Lett. 50 (1987) 416.
33. N. E. B. Cowern, K. T. F. Janssen and H. F. F. Jos, J. Appl. Phys. 68, 6191 (1990).
34. E. Schroer, F. Priolo, E. Napolitani, A. Carnera and V. Privitera, Appl. Phys. Lett. 74 (1999) 3996.
35. M. D. Giles, J. Electrochem. Soc. 138, 1160 (1991).
36. N. E. B. Cowern and C. Rafferty, MRS Bull. 25, 39 (2000).
37. N. E. B. Cowern, M. Jaraiz, F. Cristiano, A. Claverie and G. Mannino, Tech. Dig. Int. Electron Devices Meet., 333 (1999).
38. P.M.Fahey, P.B.Griffin, J.D.Plummer; *Point defects and dopant diffusion in silicon*; Reviews of Modern Physics, vol 61, p289 (1989)
39. J. D Plummer, M. D. Deal and P. B. Griffin, *Silicon VLSI Technology, Fundamentals, Practice and Modeling*, Prentice Hall, 2000.
40. Integrated Graduate Development Scheme (IGDS) Course, University of Surrey, 2005.
41. P. A. Stolk, H. J. Gossmann, D. J. Eaglesham, D. C. Rafferty, G. H. Gilmer, M. Jaraiz, J. M. Poate, H. S. Luftman, T. E. Haynes, J. Appl. Phys. 81, 6031 (1997).
42. G. Z. Pan and K. N. Tu, J. Appl. Phys. 82 (1997) 601.
43. A. Claverie, L. F. Giles, M. Omri, B. de Mauduit, G. Ben Assayag and D. Mathiot, Nuclear Instrum. Methods Phys. Res. B147 (1999) 1.

44. A. Claverie, B. Colombeau, B. de Mauduit, C. Bonafos, X. Hebras, G. Ben Assayag and F. Cristiano, Appl. Phys. A 76, 1025 (2003).
45. D. J. Eaglesham, P. A. Stolk, H. J. Gossmann and J. M. Poate, Appl. Phys. Lett. 65 (1994) 2305.
46. L. H. Zhang, K. S. Jones, P. H. Chi, D. S. Simons, Appl. Phys. Lett. 67 (1995) 2025.
47. H.G. A. Huizing, C. C. G. Visser, N.E.B. Cowern, P. A. Stolk and R. C. M. de Kruif, Appl. Phys. Lett. 69 (1996) 1211.
48. N.E. B. Cowern, D. Alquier, M. Omri, A. Claverie and A. Nejim, Nuclear Instrum. Methods Phys. Res. B148 (1999) 257.
49. M. M. De Souza, C. K. Ngw, M. Shishkin, E. M. Narayanan : Phys. Rev. Lett. 83, 1799 (1999).
50. I. M. Lifshitz, V. V. Slyosov, J. Phys. Chem. Sol. 19 (1961) 35.
51. C. Bonafos, A. Martinez, M. Faye, C. Bergaud, D. Mathiot and A. Claverie, Nucl. Inst. Meth. Phys. Res. B 106, 222 (1995).
52. S. Saito, S. Shishiguchi, A. Mineji and T. Matsuda, Mat. Res. Soc. Symp. Proc. 532, 3 (1998).
53. G. Mannino, P. A. Stolk, N. E. B. Cowern, W. B. de Boer, A. G. Dirks, F. Roozeboom, J. G. M. van Berkum, P. H. Woerlee and N. N. Toan, Appl. Phys. Lett. 78 (2001) 889.
54. A. Agarwal, H.-J. Gossmann, A. T. Fiory, V. C. Venezia and D. C. Jacobson, Proc. Of Electrochemical Society, PV 2000, May 14-18 (2000), Toronto, Canada.
55. M. Mehrotra, J. C. Hu, A. Jain, W. Shiau, S. Hattangady, V. Reddy, S. Aur, and M. Rodder, Tech. Dig. Int. Electron Devices Meet. (1999), 419.
56. W. Lerch, S. Paul, J. Neiss, S. McCoy, T. Selinger, J. Gelpey, F. Cristiano, F. Severac, M. Gavelle, S. Boninelli, P. Pichler and D. Bolze, Mat. Science and Engineering B 124-125 24 (2005).
57. S. B. Felch, H. Graoui, G. Tsai and A. Mayur, Nucl. Inst. Meth. Phys. Res. B 237, 35 (2005).
58. S. D. Kim, C. M. Park and J. C.S. Woo, Solid State Electronics 49 131 (2005).
59. Y. F. Chong, K. L. Pey, A. T. S. Wee, A. See, L. Chan, Y. F. Liu, W. D. Song and L. H. Chua, Applied Physics Letter, 76, 3197 (2000).
60. R. Surdeanu, Y. V. Ponomarev, R. Cerutti, B. J. Pawlak, L. K. Nanver, I. Hoflijk, P. A. Stolk, C. J. J. Dachs, M. A. Verheijen, M. Kaiser, M. J. P. Hopstaken, J. G. M van Berkum, F. Roozeboom and R. Lindsay, Proceedings of ECS (2002).
61. L. K. Nanver, J. Slabbekoorn and A. Burtsev et al.,, ECS Proceedings, vol. 14, 119 (2003).
62. J. A. Sharp, N. E. B.Cowern, R. B. Webb, D. Giubertoni, S. Gennaro, M. Bersani, M. A. Foad, F. Cristiano, P. F. Fazzini and K. J. Kirkby, Appl. Phys. Lett. 89, 192105 (2006).

63. D. Eaglesham, T. Haynes, H.-J. Gossmann, D. Jacobson and P. Stolk, Appl. Phys. Lett. 70, 24, 3281 (1997).
64. V. Venezia, T. Haynes, A. Agarwal, L. Pelaz, H.-J. Gossmann, D. Jacobson and D. Eaglesham, Appl. Phys. Lett. 74, 9, 1299 (1999).
65. L. Shao, X. Wang, J. Liu, J. Bennett, L. Larsen and W. –K. Chu, J. Appl. Phys. 92, 4307 (2002).
66. W. –K. Chu, L. Shao, X. Wang, J. Liu, P. E. Thompson and H. Chen, Proceedings of the 14th International conference on Ion Implantation Technology, 22-27 Sept 2002, pp 48-51.
67. L. Shao, J. Zhang, J. Chen, D. Tang, P. E. Thomson, S. Patel, X. Wang, H. Chen, J. Liu, W. –K. Chu, Appl. Phys. Lett. 84, 3325 (2004).
68. A. J. Smith, *The formation of Ultra-shallow p-type Junctions using Vacancy Engineering,* Ph.D. dissertation, University of Surrey, UK, 2006.
69. P. A. Stolk, D. J. Eaglesham, H.-J. Gossmann, J. M. Poate, Appl. Phys. Lett. 66, 1370 (1995).
70. S. Mirabella, A. Coati, D. De Salvador, E. Napolitani, A. Mattoni, G. Bisognin, M. Berti, A. Carnera, A. V. Drigo, S. Scalese, S. Pulvirenti, A. Terrasi and F. Priolo, Phys. Rev. B 65, 45209 (2002).
71. R. Scholz, U. Gosele, J. –Y. Huh, T. Y. Tan, Appl. Phys. Lett. 72, 200 (1998).
72. S. Nishikawa, A. Tanaka and T. Yamaji, Appl. Phys. Lett. 60, 2270 (1992).
73. A. Cacciato, J. G. E. Klappe, N. E. B. Cowern, W. Vandervost, L. P. Biro, J. S. Custer, F. W. Saris, J. Appl. Phys. 79, 2314 (1996)
74. S. Lombardo, A. Cacciato, K. K. Larsen, V. Raineri, F. la Via, V. Privitera and S. U. Campisano, J. Appl. Phys. 79, 3464 (1996).
75. H. J. Osten, R. Bath, G. Fisher, B. Heinemann, D. Knoll, G. Lippert, H. Rucker, P. Schley and W. Ropke, Thin Solid Films, volume 321, 11 (1998).
76. P. Chevalier, C. Fellous, B. Martinet, F. Leverd, F. Saguin, D. Dutare and A. Chantre, Proc. European Solid State Device Research Conf. p.299 (2003).
77. G. Fuse, T. Hirao, K. Inoue, S. Takayanagi and Y. Yaegashi, J. Appl. Phys. 53, 3650 (1982).
78. M. Delfino and M. E. Lunnon, J. Electrochem. Soc. Solid State Science and Technology, v.132, no. 2, 435 (1985).
79. H.-H. Vuong, H.-J. Gossmann, C. S. Rafferty, H. S. Luftman, F. C. Unterwald, D. C. Jacobson, R. E. Ahrens, T. Boone and P. M. Zeitzoff, J. Appl. Phys. 77 (1995) 3056.
80. J. Liu, D. F. Downey, K. S. Jones and E. Ishida, Proc. Int. Conf. Ion Implantation Technology, 951 [1999].
81. L. S. Robertson, J. Jacques, D. F. Downey, K. S. Jones, M. E. Law, M. J. Rendon and D. Sing, International workshop on junction technology 2001, IWJT-57, 4-1-1 (2001).

82. G. Impellizzeri, J. H. R, Dos Santos, S. Mirabella, F. Priolo, E. Napolitani, A. Carnera, Materials Research Society Symposium - Proceedings, v 810, Silicon Front-End Junction Formation - Physics and Technology, 2004, p 253-258
83. H. A. W. El Mubarek, Y Wang, R. Price, J. M. Bonar, J. Zhang, P. L. F. Hemment and P. Ashburn, Mat. Science in Semiconductor Processing 8, 103 (2005).
84. G.Impellizzeri, *Fluorine enriched silicon: properties and advantages*; PhD thesis, University of Catania, Sicily (2004)
85. S. M. Hu, J. Appl. Phys. 45 (1974) 1567.
86. J. M. Bonar, B. M. McGregor, N. E. B. Cowern, A. H. Dan, G. A. Cooke and A. F. W. Willoughby, Mat. Res. Soc. Symp. Vol. 610, B.4.9.1 (2000)
87. S. Uppal, A. F. W. Willoughby, J. M. Bonar and J. Zhang, Appl. Phys. Lett. 85, 552 (2004)
88. Y. Zaitsu, T. Shimizu, J. Takeuchi, S. Matsumoto, M. Yoshida, T. Abe and E. Arai, J. Electrochem. Soc., Vol. 145, 258 (1998)
89. M. S. A. Karunaratne, A. F. W. Willoughby, J. M. Bonar, J. Zhang and P. Ashburn, J. Appl. Phys. 97 (2005) 113531.
90. H. Bracht, N. A. Stolwijik and H. Mehrer, Physical Review Vol. **52**, 16542 (1995)
91. H. Bracht, MRS Bull. 25 (6), (2000)
92. Athena User's manual (2001), Silvaco international, 4701 Patrick Henry Drive, Bldg. 1, Santa Clara, CA 95054.
93. J. M. Bonar, *Process Development and Characterization of Silicon and Silicon-Germanium Grown in a Novel Single-Wafer LPCVD System*, Ph. D. dissertation, University of Southampton, UK, 1996.
94. H. A. W. El Mubarek, *Suppression of Boron Transient Enhanced and Thermal Diffusion in Silicon and Silicon-Germanium by Fluorine Implantation,* Ph. D. dissertation, University of Southampton, UK, 2004.
95. J. W. Mayer, L. Eriksson and J. A. Davies, *Ion Implantation in Semiconductors, Silicon and Germanium,* Academic Press, 1970.
96. V. Haublein, L. Frey and H. Ryssel, Proceedings of the 14th International Conference on Ion Implantation Technology, 22-27 Sept. (2002) 217.
97. S. B. Felch, B. S. Lee, D. F. Downey, Z. Zhao and R. J. Eddy, Proceedings of the International Conference on Ion Implantation Technology, p611-614 (1996)
98. R.G. Wilson, F. A. Stevie and C. W. Magee, *Secondary Ion Mass Spectroscopy: A practical hand book for depth profiling and bulk impurity analysis*, John Wiley & Sons, 1989.
99. R. B. Fair, *Impurity Doping*, edited by F. F. Y. Wang (North Holland, Amsterdam, 1981), Chapter 7, pp. 315-442.

100. G. R. Nash, J. F. W. Schiz, C. D. Marsh, P. Ashburn, G. R. Booker, Appl. Phys. Lett. Vol 75, 3671 (1999)

101. X. D. Pi and C. P. Burrows and P. G. Coleman, Phys. Rev. Lett., vol. 90, 155901, (2003).

102. D. Skarlatos, D. Tsoukalas, L. F. Giles and A. Claverie, J. Appl. Phys., 87 (2000) 1103.

103. H. Park, H. Robinson, K. S. Jones, and M. E. Law, Appl. Phys. Lett. 65, 436 (1994).

104. N. E. B. Cowern, B. Colombeau, E. Lampin, F. Cristiano, A. Claverie, Y. Lamrani, R. Duffy, V. Venezia, A. Heringa, C. C. Wang, C. Zechner, Mat. Res. Soc. Symp. Proc. Vol. 765, D6.8.1, (2003)

105. Cristiano et al, Nucl. Instru and Methods in Phys B 216 (2004), 46-56

106. H. L. Meng, S. Prussin, M. E. Law and K. S. Jones, J. Appl. Phys., 73 (1993) 955.

107. J. K. Listebarger, K. S. Jones, J. A. Slinkman, J. Appl. Phys., 73 (1993) 4815.

108. J. F. Ziegler and J. P. Biersack, The Stopping Range of Ions in Matter (2003) Available online: http://www.srim.org

109. D. A. Abdulmalik, P. G. Coleman, N. E. B. Cowern, A. J. Smith, B. J. Sealy, W. Lerch, S. Paul and F. Cristiano, App. Phys. Lett. Vol. 89, 052114 (2006).

110. S. Boninelli, N. Cherkashin, A. Claverie, F. Cristiano, Nucl. Instruments and Methods in Physics Research B 253 (2006) 80-84.

111. P. Ward, private communication.

112. H. Graoui, M. Hilkene, B. McComb, M. Castle, S. Felch, A. Al-Bayati, A. Tjandra, M. A. Foad, Nucl. Instruments and Methods in Physics Research B 237 (2005) 46-52.

113. J.-M. Ha, J.-W. Park, S. Felch, K. Fujihara, H.-K. Kang, S.-I. Lee, Surface and Coatings Technology 136, 157 (2001)

LIST OF PUBLICATIONS

Study of Fluorine Behavior in Silicon by Selective Point Defect Injection
M. N. Kham, H. A. W. El Mubarek, J. M. Bonar and P. Ashburn
Applied Physics Letter, 87 011902 (2005)

Effect of Fluorine on Boron Thermal Diffusion in the presence of Point Defects
M. N. Kham, H. A. W. El Mubarek, J. M. Bonar and P. Ashburn
Materials Science and Engineering B, 124-125 192 (2005)

Effect of Fluorine on Boron Diffusion under Interstitial Injection from the Surface
M. N. Kham, H. A. W. El Mubarek, J. M. Bonar, D. Chivers and P. Ashburn
Nuclear Instruments & Methods in Physics Research B, 253 100 (2006)

110GHz f_T Silicon Bipolar Transistors Implemented using Fluorine Implantation for Boron Diffusion Suppression
M. N. Kham, H. A. W. El Mubarek, J. M. Bonar, P. Ward, L. Fiore, R. Petralia, C. Alemanni, A. Messina and P. Ashburn
IEEE Transactions on Electron Devices, Vol. 53 Number 3 546 (2006).

Reduced Boron diffusion under Interstitial Injection in Fluorine Implanted Silicon
M. N. Kham, I. Matko, B. Chenevier and P. Ashburn
Accepted for publication in Journal of Applied Physics (2007)